Beyond the track: The processing of double strand breaks after iron-ion irradiation and the role of base excision repair

Zur Erlangung des Grades eines Doktors der Naturwissenschaften (Dr. rer. nat.)
Genehmigte Dissertation von Laura Schwan
Tag der Einreichung: 10.06.2025, Tag der Prüfung: 10.09.2025

1. Gutachten: Prof. Dr. Burkhard Jakob
2. Gutachten: Prof. Dr. Alexander Löwer
Darmstadt, Technische Universität Darmstadt

TECHNISCHE
UNIVERSITÄT
DARMSTADT

Biologie
GSI Helmholtzzentrum für Schwerionenforschung GmbH
Biophysik

Schwan, Laura: Beyond the track: The processing of double
strand breaks after iron-ion irradiation and
the role of base excision repair
Darmstadt, Technische Universität Darmstadt,
Jahr der Veröffentlichung der Dissertation auf TUprints: 2026
URN: https://nbn-resolving.org/urn:nbn:de:tuda-tuda-153354
Tag der mündlichen Prüfung: 10.09.2025

Ehrenwörtliche Erklärung:

Ich erkläre hiermit, dass ich die vorliegende Arbeit ohne unzulässige Hilfe Dritter angefertigt habe. Sämtliche aus fremden Quellen direkt oder indirekt übernommenen Gedanken sowie sämtliche von Anderen direkt oder indirekt übernommenen Daten, Techniken und Materialien sind als solche kenntlich gemacht.

Ferner erkläre ich, dass ich bei der Verfassung der Dissertation die ”Grundsätze zur Sicherung guter wissenschaftlicher Praxis an der Technischen Universität Darmstadt” und die ”Leitlinien zum Umgang mit digitalen Forschungsdaten an der TU Darmstadt” in den jeweils aktuellen Versionen beachtet habe. Die Arbeit wurde bisher bei keiner anderen Hochschule zu Prüfungszwecken eingereicht.

Darmstadt, 10.06.2025

L. Schwan

Abstract

Gebündelte DNS-Schäden sind eines der Hauptmerkmale ionisierender Strahlung und stellen ein hohes Risiko für die Gesundheit dar. Vor allem können sie zu der Entstehung von Krebs beitragen. Dabei wird zwischen hoch- und niedrig-LET (Linearer Energietransfer) Strahlung unterschieden, wobei hoch-LET Strahlung, z.B. beschleunigte Schwerionen, zunehmend komplexere Schäden verursacht als niedrig-LET Strahlung mit Photonen. Aufgrund des Erdmagnetfelds und der Atmosphäre ist die Gefahr der Schwerionen-Exposition für auf der Erde lebende Menschen zu vernachlässigen. Sobald diese schützenden Faktoren auf Weltraumreisen jedoch überwunden werden, sollten die Risiken, die mit solch einer Strahlenbelastung verbunden sind, bestens eingeschätzt werden können. Die radiobiologische Wirkung von kosmischer Strahlung wird dabei oft mit Eisenionen an Beschleuniger-Anlagen simuliert. Während ein Schwerion den Zellkern passiert, entstehen durch die Wechselwirkung des Ions mit den biologischen Molekülen der Zelle dicht gebündelte DNS-Schäden verschiedenster Komplexität entlang der Ionen-Trajektorie. Durch die Ionisation werden auch sekundäre Elektronen, aufgrund ihrer hohen Energie als δ-Elektronen bezeichnet, freigesetzt. Diese verursachen wiederum Schäden außerhalb der Ionenspur, und je nach Energie erreichen sie selbst auch Nachbarzellen. Zu den Hauptschäden gehören neben DNS-Doppelstrangbrüchen (DSB) und Einzelstrangbrüchen auch Basenschäden. Letztere werden über die sogenannte Basenexzisionsreparatur (BER) repariert, wobei nach Entfernen der geschädigten Base ein Einzelstrangbruch als kontrollierter Zwischenschritt verursacht wird. In dieser Arbeit wird demnach mithilfe des Einsatzes von Inhibitoren gegen zwei der in BER involvierten Faktoren gezeigt, dass DSB durch die gleichzeitige Tätigkeit von mehreren BER-Prozessen an benachbarten Basenschäden nach der Gabe von Kaliumbromat ($KBrO_3$) entstehen. Es kann angenommen werden, dass diese zusätzlichen DSB die Schadenskomplexität nach Schwerionenbestrahlung in der Ionenspur noch weiter erhöhen. Komplexe Schäden werden sehr häufig mithilfe von Resektionsprozessen an den Bruchenden repariert, wohingegen weniger komplexe Schäden, wie solche die durch Photonen oder Elektronen verursacht werden, meistens über nicht-homologe Endverknüpfung repariert werden. Obwohl die Schadenskomplexität von δ-Elektronen verursachten DSB denen der Photonen-induzierten DSB ähnelt, wurde vermehrt Resektion sowie auch homologe Rekombination an DSB außerhalb der Ionenspur

in G1/G2-Zellen beobachtet. Im Gegensatz dazu zeigen Fibroblasten, fast ausschließlich in G1, überraschenderweise eine leicht schnellere Reparatur der gleichen Schäden im Vergleich zu DSB nach Röntgenbestrahlung.
Diese Ergebnisse unterstreichen die Wichtigkeit, die biologische Strahlenantwort nach Schwerionen-Exposition zu untersuchen. Nicht nur werden relativ simple Basenschäden in potentiell kanzerogene DSB umgewandelt, sondern auch die Komplexität der Spurschäden durch zusätzlich entstehende DSB erhöht. Das gleichzeitige Vorhandensein von großer Schadenskomplexität und weniger komplexen Schäden außerhalb der Spur scheint die Reparatur von letzteren in Richtung Resektionsabhängigkeit zu beeinflussen. Obwohl noch weitere Experimente notwendig sind, um die hier gemachten Punkte zu unterstützen, können die Ergebnisse für die radiobiologische Modellierung der Schadensinduktion und -reparatur nützlich sein. Die Wirkung von ionisierender Strahlung auf Zellen auf molekularer Ebene ist vor allem wichtig für die Risikoabschätzung bemannter Weltraummissionen. Radiobiologische Experimente an Beschleuniger-Anlagen auf der Erde unterstützen somit die Erkenntnisgewinnung und diese Arbeit bildet einen kleinen Teil im Bereich der DNS-Reparatur nach hoch-LET Eisenionen-Bestrahlung ab.

Abstract

Clustered DNA damage as one of the hallmarks of ionizing radiation, poses a great risk on the genomic integrity. High frequencies of clustered DNA damage induced by ionizing radiation increase the overall cancer risk. The exposure to high linear energy transfer (LET) charged particles, like heavy ions, leads to the induction of increasingly clustered DNA lesions compared to low-LET photon irradiation. Although environmental heavy-ion exposure poses no great risk to humans on Earth due to the Earth's atmosphere and magnetic shielding, it represents a significant threat on the human health during deep space missions. To study the (health) effects of the biologically highly effective heavy-ion exposure as part of the galactic cosmic ray (GCR) spectrum, irradiation experiments are commonly performed with accelerated iron (Fe) ions. While heavy ions pass through the cellular nucleus, they induce highly clustered DNA-lesions along their pathway. Due to the ion's interaction with matter, δ-electrons emerge and depending on the ion's initial energy, they can deposit energy distant to the ion track (off-track), even in adjacent cells. Besides single- and double strand breaks (SSBs, DSBs), ionizing radiation leads to a high abundance of base lesions. Base lesions will be immediately processed by the well conserved base excision repair (BER) pathway. During the base removal, endonuclease activity at the damage site leads to the induction of a SSB as an intermediate step. In this work it was shown that by using inhibitors against two BER-related factors, 8-OxoG DNA glycosylase 1 (OGG1) and AP endonuclease 1 (APE1), BER processes induced by administering the oxidizing agent $KBrO_3$ lead to the emergence of additional DSBs in non-inhibited human cells. The higher DSB load observed in non-inhibited cells after heavy-ion irradiation suggests that BER processes increase damage clustering within the ion's narrow track area. To repair most of the highly clustered track damage, DNA-end resection needs to be performed first, while less complex photon-irradiation induced breaks usually do not depend on resection and are ligated via non-homologous end-joining (NHEJ) predominately. Although the complexity of δ-electron induced DSBs outside of the track region can be considered almost identical to DSBs induced by low-LET photon irradiation, increased resection with subsequent processing via homologous recombination (HR) was observed at off-track DSBs in a mixed population of G1/G2 cells with concurrent ion tracks. Contrary to the finding of an extended use of resection at off-track DSBs,

repair kinetics assessed in mainly G1-phase cells are surprisingly faster for off-track DSBs compared to DSBs induced by low-LET X-rays.

These findings underline the importance of the biological processing of less-serious base lesions into DSBs, which threaten the genomic integrity especially due to increased damage clustering in heavy-ion tracks. The simultaneous occurrence of strongly clustered in-track DNA-damage and less-clustered off-track DSBs seems to further affect the processing of the latter. Although further work is necessary, the results obtained from this project could be of interest for the radiobiological modeling of IR induced DNA damage. Understanding the effects of high-LET irradiation on the molecular level and its consequences on the cell fate regarding for instance cancer induction, is indispensable for the risk assessment of manned future deep space missions. Ground-based radiobiological experiments with heavy ions are of great importance to study the effects of GCR exposure on the human health and this work contributes to the understanding of the DNA-damage response to high-LET heavy-ion irradiation.

Contents

3 Results 29

List of Figures

List of Tables

Abbreviations

Abbreviation / Acronym	Definition
γH2AX	Serin 139 phosphorylated histone H2AX
53BP1	TP53-binding protein 1
8-OxoG	8-Oxo-2'-deoxyguanosine
a-EJ	Alternative end-joining
AP	Apurinic / apurimidinic
APE1	AP endonuclease 1
ATM	Ataxia telangiectasia mutated kinase
BER	Base excision repair
BERi	Base excision repair inhibitor
BSA	Bovine serum albumin
C	Carbon
CA	Chromosomal aberrations
CENPF	Centromere protein F
CPD	Cumulative doubling time
DAPI	4,6-Diamidin-2-phenylindol
DDR	DNA damage response
DMEM	Dulbecco's Modified Eagle Medium
DNA	Deoxyribonucleic acid
DSB	Double strand break
dsDNA	Double stranded DNA
ECDF	Empirical cumulative distribution function
EdU	5-Ethynyl 2'-deoxyuridine
EU	5-Ethynyl uridine
FBS	Fetal bovine serum
FC	Flow cytometry
Fe	Iron
GCR	Galactic cosmic rays

GSH	Reduced glutathione
$^{\bullet}$HO	Hydroxyl radical
H_2O_2	Hydrogen peroxide
HDR	Homology directed repair
HR	Homologous recombination
HZE	High charge and high energy
ICR	Inter quartile range
IF	Immunofluorescence
IR	Ionizing radiation
KAP-1	KRAB-associated protein 1
Ku	Ku70/Ku80 heterodimer
LET	Linear energy transfer
Li	Lithium
MMEJ	Microhomology-mediated end-joining
MX	Methoxyamine hydrochloride
NHEJ	Non-homologous end-joining
OGG1	8-Oxoguanine glycosylase
PARP1	Poly ADP-ribose polymerase 1
PBS	Phosphate buffered saline
PI	Propidium iodide
PT	Particle therapy
RAD51	DNA repair protein RAD51 homolog 1
RBE	Relative biological effectiveness
RIF	Radiation induced foci
RNA	Ribonucleic acid
ROS	Reactive oxygen species
RPA	Replication protein A
SD	Standard deviation
SDSA	Synthesis-dependent strand annealing
SEM	Standard error of the mean
SSA	Single-strand annealing
SSB	Single strand break
ssDNA	Single stranded DNA
TEM	Transmission electron microscopy
U	Uranium
U2OS	Human osteosarcoma cells

1 Theory

1.1 Ionizing radiation and its biological impact

The increasing popularity of space missions leads to growing concerns about the risk assessment for a human being exposed to different space hazards. NASA's Human Research Program (HRP) lists them as follows: Isolation and confinement, distance from Earth, gravity fields, hostile and closed environments and foremost space radiation [1]. There exists a variety of more or less effective counter measurements for the psychological effects as well as for the impact of microgravity to the general fitness [2]. The exposure to ionizing radiation (IR) becomes increasingly more prevalent when the space traveller leaves the atmosphere and Earth's magnetic field and is completely exposed to the galactic cosmic radiation (GCR) field of the outer space. On the Moon's surface, radiation dose levels are assumed to be 2.6 times higher than on the international space station (ISS) located in the low Earth orbit (LEO) [3]. Future manned space missions will be of longer duration than previous missions and in the case of an exploratory long-term mission to Mars the space explorer will be exposed to GCR for well above six months. Additional solar particle events (SPE) derived from the Sun complicate the dose estimation further due to their unpredictable nature. The constant exposure to GCR on the human body is assumed to result in increased risks of cardiovascular alterations [4], damage to the central nervous system (CNS) [5] as well as cataracts [6] and cancer due to the increased carcinogenic effect of heavy ions [7].

Especially the high energy and high charge number Z (HZE) ion part, although with an abundance of only 1% for $Z \geq 3$ of the whole GCR spectrum [8], has a considerable contribution to the dose-equivalent [9]. Iron (^{56}Fe) ions have a particularly important role when considering the HZE-ion distribution of the GCR spectrum due to their high abundance and increased biological effectiveness [8]. For instance, during a three-year mission through space around 33% of all cellular nuclei in a human body will receive one HZE-ion hit [10]. Although passive radiation shielding can mitigate the exposure to the GCR field to some extend [7], very high energetic ions pose especially difficult to shield with the currently used spacecraft materials, primarily aluminum. With more shielding

material added, the production of secondary particles due to the interaction of HZE ions with the shielding material will increase, resulting in a complex radiation field [11, 12]. Additionally, using more material to achieve thicker shielding would add significantly on the total cost to launch the spacecraft. Also the materials atomic number needs to be taken into account for designing effective shielding strategies [11]. The interaction of HZE ions with low Z number shielding materials for instance produces only secondary particles that are biologically less damaging than the particles emerging from the interaction with high Z number materials, which favors the implementation of lighter (composite) materials composed of mainly hydrogen [11]. Epidemiological data to estimate the health risk for exposure exists only for γ-rays in the high-dose range derived from the historical atomic bomb incidents [13], not for low-dose rate charged particle exposure as in the space environment. This leads to high uncertainties in the risk assessment for missions into space. For instance, the uncertainty of cancer risk due to GCR exposure during an exploratory Mars mission is estimated to be between 400% and 600% [14].
Other than space, heavy-ion irradiation has an emerging role in the field of radiotherapy foremost to treat cancer, with the main focus on carbon (^{12}C) ions [15]. Besides C ions, other potential candidates for radiotherapeutic applications are helium (^{4}He) and oxygen (^{16}O) ions [16]. More recently, radioactive ion beams (^{11}C) [17] have been explored for particle therapy (PT) as well. Another important source for the exposure to charged particles on earth is found in the ground. Besides other naturally occurring radionuclides, resources of uranium (^{238}U) within the soil decay into gaseous radon (^{222}Rn) which further decays within a relatively short half-life of 3.82 days while emitting α-particles (Helium nuclei, He^{2+}), just like the subsequent daughter nuclei with an even shorter half-life of less than 1 h [18]. Inhaling radon gases thus leads to the exposure to α-particles and poses the increased risk of developing lung cancer, especially if the (solid) descendants accumulate around the bronchial tissue [19].

When charged particles, like protons, α-particles or ions, enter (biological) material, like human tissue, the frequency of interactions with the surrounding molecules and atoms continues to increase non-linearly until the particle comes nearly to a halt. The amount of transferred energy per penetration depth has the distinct shape of a so called Bragg curve, with the Bragg peak marking the maximum of the released energy. The linear energy transfer (LET) is one important property of accelerated charged particles to understand their increased biological effectiveness, compared to photons [20]. Especially PT benefits of this narrow dose deposition around the Bragg peak, while healthy tissue can effectively be spared in the particle entrance region [21]. Via shifting of the ion's kinetic energy to spread out the Bragg peak region (SOBP), the tumor volume can be exposed to a homogenous dose distribution, making it superior to photon irradiation with the exponentially decreasing distribution of dose along a photon's pathway [22]. Due to the sharp fall-off at the distal region of the Bragg peak (figure 1.1), tissue of high risk can be effectively spared [22]. LET is inversely related to the square of velocity and it increases with the square of the charge number of the projectile (ion), which can be derived from the Bethe equation [23]. Photons interact with matter differently from charged particles. The interaction of low energetic photons can be described by the photoelectric effect. Energy is transferred from the incident photon to an atomic-bound electron, leading effectively to its removal if the photon's energy is at least the electron-nucleus binding energy. With higher photon energies around the X-ray regime, scattering events become more prevalent. Within the Compton scattering, the scattered photon transfers some energy to a target electron, while it continues with longer wavelengths. The transferred energy removes the recoiled electron from its bound state. At even higher energies, at least above the resting energy of one electron and one positron (1.022 MeV), pair production within the potential field of an atomic nucleus may occur more frequently. Since this work focusses solely on the biological impact of ionizing radiation, X-rays within the keV regime have been utilized which implies that Compton scattering is the main type of photon-matter interaction in this case. In contrast to the peak behavior of charged particles, the shape of the photon's dose-depth profile is exponentially declining (figure 1.1).

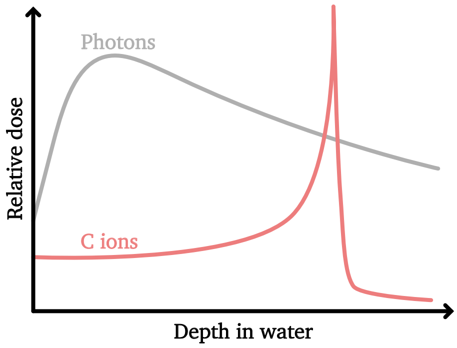

Figure 1.1: Depth-dose profile of therapeutic photons and C ions with pronounced Bragg peak in water.

Exposure to heavy ions increases the percentage of tumor prevalence in mice to a larger degree than same dose photon irradiation [24]. Correspondingly, heavy ions are more effective than photons in neoplastic transformation of mammalian cells [25]. Due to the mutational consequences, deoxyribonucleic acid (DNA) resembles a highly sensitive target of cells regarding radiation damage. During the interaction with cells, the passage of charged particles will produce a track of direct ionization events along the ions pathway and induce clustered and complex DNA damage inside the cellular nucleus. Within these ionizations, high energetic secondary electrons (δ-electrons / δ-rays) are being released, while the density of δ-electrons induced ionizations follows an inverse square law [26]. The direction of δ-electron emission is not isotropically but angular from the ion track, while the angle depends on the kinetic energy of the δ-electron [27]. Those electrons further induce DNA lesions around the track region and increase the overall damage load inside the cellular nucleus [26]. Thus, the irradiation with charged particles is of mixed radiation quality, with high-LET damage along the track and low-LET damage around the track. If the projectile ion is of high energy, the liberated δ-electrons can even reach the mm range and deposit energy in adjacent cells not directly hit by the ion [28]. Since more than half of the ion's initial kinetic energy is distributed to the δ-electron energy spectrum [27], the damage induced by those electrons has to be considered while studying the effects of HZE ions on the DNA integrity.

Irradiating a monolayer of cells with charged particles at low fluences using an accelerator results in a Poisson distribution of direct hits, with a significant fraction of cells not being traversed by the particle. Consequently, the use of the macroscopic dose in this regard may not be the ideal parameter to describe and compare the biological effects of low- and high-LET irradiation. For instance, high-LET ions would cause way more damage in traversed cells as cells irradiated with lower LET protons at the same averaged dose [20, 29, 30]. Instead, LET together with the fluence of particles per unit area may be more appropriate, which are correlated to dose as follows:

$$D = 1.6 \cdot 10^{-9} \frac{LET \cdot f}{\rho} \tag{1.1}$$

With dose D in Gy, LET in keV/µm, fluence f in particles/cm^2 and the material density ρ in g/cm^3. The factor $1.6 \cdot 10^{-9}$ is needed for the unit conversion.

Upon the traversal of a cell's nucleus by photons or charged particles, ionization events can either damage the DNA directly by interacting with the DNA molecules or indirectly by leading to the production of reactive oxygen species (ROS) in the surrounding water through water hydrolysis [31]. Additionally, the location of ROS production and diffusion can be further divided into the two components of the water layer: the first hydration layer enclosing the DNA structure and bulk water, while only the latter one would include the possibility of free radical scavengers which might mitigate the damaging abilities of ROS [31]. The indirect effect accounts for approximately 71% [32] of the total DNA damage after X-ray irradiation and is attributed towards the highly reactive hydroxyl radical ($^{\bullet}$HO) as the main contributor [32]. $^{\bullet}$HO damages prevalently nearby DNA bases [33, 34] and to a lesser degree sugar moieties [34, 35]. Due to its short mean diffusion distance of 6 nm it needs to be in direct proximity to the DNA [32]. Other non-radicals like hydrogen peroxide (H_2O_2) are able to form highly reactive $^{\bullet}$HO through a Fenton reaction with DNA-bound transition metal ions [36]. Cytoplasmic radical scavengers, for instance glutathione [37], can react with ROS like $^{\bullet}$HO and non-radicals like H_2O_2 to convert those damaging agents into less toxic products, although radicals formed in the first hydration layer in direct vicinity to the chromatin may not be scavengeable and lead consequently to several DNA lesions [31, 38].

1.2 DNA damage response (DDR)

Ionizing radiation (IR) can induce a plethora of different lesions in the DNA. Types of damage include base damage, apurinic or apurimidinic (AP) sites, single strand breaks (SSB) and double strand breaks (DSB) with differing complexity. The amount of those lesions depends strongly on the particles or photon's initial kinetic energy and thus the number and location of ionization events inside the nucleus. Most of the lesions induced by IR are SSBs with a yield of 1000 per cell per Gy [39] and 2 to 2.7 times more base lesions [39, 40]. The yield of DSBs with 35 to 40 per cell per Gy [39, 41] is much smaller, since two events on opposite strands with a maximum distance of approximately 10 bp [42, 43] would be required. Moreover, the number of IR induced DSBs increases linearly with dose [44]. And more than 17.5 eV of energy deposition at the sugar-phosphate is needed to induce one single SSB [42, 45].

Singly damaged sites, which compose of only one isolated lesion, should be repaired efficiently and almost error-free, since the undamaged opposite strand would serve as a template. Those lesions can be the result of an isolated event, for example a single photon, particle or radical hitting the DNA molecules directly without the production of additional radicals. For instance, the interaction of ROS with DNA may lead to the generation of many isolated SSBs [46, 47]. In contrast, locally multiply damaged sites (LMDS) usually involve more than one radical species within a small volume and are thus quite common in energy deposition events of IR [39] and without radiation only achievable for example with high concentrations of H_2O_2 treatment [48]. Clustered lesions consist of SSBs, AP sites, base lesions as well as DSBs at different ratios (figure 1.2) while they have to be located in close proximity within a 1 nm to 4 nm DNA segment [49], the equivalent of one or two helical turns. DSBs accompanied directly by base damage, AP sites or strand breaks to form a cluster are considered to be complex [50]. For low-LET electrons, at least 20% of all induced DSBs are already assigned to be of complex type (DSB + strand break) [50]. With increasing LET, the complexity of DNA damage clusters increases [40]. After high-LET irradiation, around 70% of DSB clusters are accompanied by single SSBs whereas in 90% of all DSB clusters, SSBs with additional base lesions can be observed [40]. Consequently, clustered lesions are regarded as one hallmark of high-LET irradiation [51, 52]. As stated earlier, high-LET radiation is part of the GCR spectrum which poses increased cancer risks to exposed space travelers [9]. To handle this high diversity of DNA lesions, mammalian cells have developed different repair pathways.

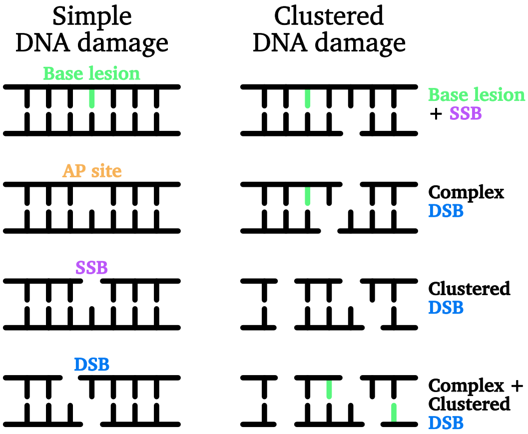

Figure 1.2: Simple and clustered DNA damage. Based on Danforth, Provencher, and Goodarzi [53].

1.2.1 Base excision repair (BER)

Base excision repair (figure 1.3) is a highly conserved pathway, relevant in bacteria up to mammalian cells, for repairing DNA base lesions of different kind. Since cells produce endogenous oxidative damage in high abundance, with numbers of steady-state oxidative base modifications in the range of 1000 to 1260 per genome in mouse [54] and human cells [55], respectively, this repair mechanism is of great importance for the general genome maintenance. Guanosine for instance is known for having the lowest redox potential of all four nucleotides [56]. It is expected to be more frequently affected by interactions with radicals, and foremost by $^{\bullet}$HO, to form 8-OH-adduct radicals which will subsequently transform into 7,8-dihydro-8-oxoguanine (8-OxoG) [57]. During DNA strand synthesis or by inserting an oxidized deoxyguanosine triphosphate (dGTP) into the DNA during replication, 8-OxoG increases the probability of being mis-paired with adenine [58, 59] and thus forming 8-OxoG:C → 8-OxoG:A → T:A transversion mutations [60].

To efficiently remove the damaged base to prevent further accumulations of mutations, the (short-patch) BER pathway will begin with the removal of the base to produce an AP site by a specific DNA glycosylase, depending on the type of base lesion [61]. After the base removal, the AP endonuclease 1 (APE1) is being recruited to the AP site with high affinity to open the DNA backbone to facilitate the DNA polymerase (Pol β) activity for filling in the correct base. The gap is then sealed by a DNA ligase (LIG1 in the nucleus and LIG3 in mitochondria [62]) accompanied by a scaffolding protein (XRCC1) [63].

Bases are chemically modified foremost by oxidation, deamination and alkylation and besides of the already mentioned 8-OxoG, some other types of lesion include 2,6-diamino-4-hydroxy-5-N-methylformamido-pyrimidine (FaPy), thymine glycol (Tg) and uracil (U) [38, 61]. Around 11 different DNA glycosylases are able to detect the large variety of base lesions [61] while most of them are monofunctional, like uracil-N glycosylase (UNG), meaning they can only cleave glycosidic bonds. In contrast, most of the glycosylases responsible for the removal of oxidative lesions, like endonuclease VIII-like glycosylase 1-3 (NEIL1-3) and 8-OxoG DNA glycosylase 1 (OGG1), are bifunctional and besides similar glycosylase activity they can additionally induce a strand break through β-lyase activity [61, 64]. Nevertheless, OGG1 is more efficient in its glycosylase activity than in strand nicking [65]. 8-OxoG is the main substrate of OGG1 and MutY homolog DNA glycosylase (MYH) [61, 66] as well as for NEIL1 and NEIL2 [67, 68]. MYH additionally removes mis-paired A in 8-OxoG:A incorporations to decrease the frequency of T:A transversions [66].

The presence of clustered damage inhibits further strand nicking by glycosylases [69] as well as APE1 [70]. While neighboring 8-OxoG do not lead to a strong inhibition, additional AP sites and SSBs located asymmetrically opposite to the initial lesion (at base positions $\pm$ 1 and $\pm$ 3) inhibit the strand incision by APE1 strongly [70]. Nonetheless, base lesions induced by ionizing radiation can be converted into DSBs, presumably through simultaneous processing by BER in damage clusters, as observed in bacteria and mammalian cells [71–74]. Increasing numbers of DSBs originating from base excision processes performed at endogenous and peroxide induced base lesions were also observed *in vivo* and *in vitro* in mouse cells, respectively [75]. Since DSBs along heavy-ion tracks are highly clustered, additional BER processes may add to the DSB clustering. Failure in the DDR cascade may lead to an accumulation of mutations which increase the probability of neoplastic transformations and tumorigenesis [76]. In fact, several tumor tissues show increased levels of endogenous oxidative damage clusters [77] as well as higher numbers of endogenous DSBs [78] compared to non-malignant cells.

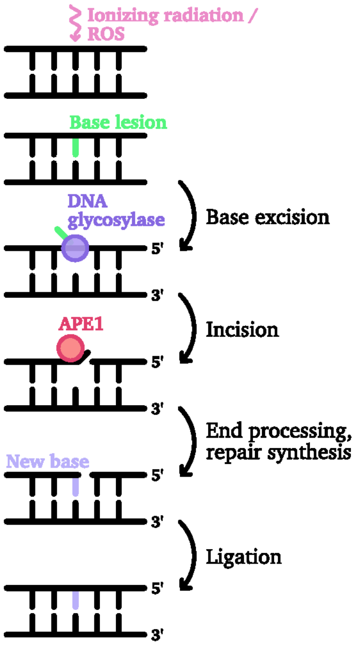

Figure 1.3: Base excision repair pathway. Based on Krokan and Bjoras [63].

1.2.2 Non-homologous end-joining (NHEJ)

DNA DSBs can pose a great risk regarding the cellular genome stability and may lead to chromosomal aberrations if they are not resolved rapidly before the next cell cycle [79]. In addition to induction by IR, DSBs can also be induced by chemical agents, like the therapeutic agent bleomycin [80], or even endogenously. For instance ROS, which are generated during normal metabolic processes, induce plenty of SSBs, while a small fraction of SSBs are being converted into DSBs during DNA replication [81]. It is assumed that around 10 DSBs per cell per day may emerge [82]. Most of the endogenous (due to physiological processes) and exogenous (for instance chemicals and radiation) induced DSBs are being repaired promptly by either one of the following two pathways, non-homologous end-joining (NHEJ) or homologous recombination (HR). The classical NHEJ (c-NHEJ) (figure 1.4) is the main DSB repair pathway [83–85] and active during the whole cell cycle of mammalian cells [86]. In contrast to HR, it does not rely on regions containing large homology sequences. Although the NHEJ pathway is more efficient if some microhomology of up to 4 bp at the break site is involved, it is able to directly ligate non-homologous blunt ends as well [87]. Since this pathway ligates broken ends without a template, NHEJ could in principle lead to the introduction of small errors like deletions or insertions at the break site and is thus regarded as more error-prone than HR. Nonetheless, the end joining of directly ligatable ends is highly accurate, while imperfectly complementary DNA ends will be joined with slightly more modifications at the break sites [88]. The pathway of NHEJ is initialized by the binding of the Ku70-Ku80 heterodimer to both, 3' and 5', double stranded DNA (dsDNA) ends with high affinity [89]. Importantly, Ku70-Ku80 binding is inhibited by long single stranded DNA (ssDNA) overhangs [89]. Following the DNA binding of Ku, DNA-dependent protein kinase catalytic subunit (DNA-PKcs) is being recruited to build a synapsis together with Ku [90]. If limited resection of the small microhomology region is required, the endonuclease Artemis is being recruited to the synapsis and its endonuclease function is activated via DNA-PKcs autophosphorylation [91]. Nevertheless, just around 10% of DSBs induced by ionizing radiation need Artemis-dependent resection during the NHEJ execution [92] and survival data attest only a small increase in radiosensitivity at low doses (< 6 Gy) due to loss of Artemis [93]. The break is then further processed by the NHEJ-exclusive DNA ligase IV (LIG4) in conjunction with the stimulating X-ray repair cross-complementing protein 4 (XRCC4) and the XRCC4-like factor (XLF), which forms a complex with XRCC4 [94]. Paralogue of XRCC4 and XLF (PAXX) is another NHEJ factor with Ku binding ability, and is similar to the structure of the XRCC4-XLF complex [95], although XLF and PAXX are assumed to be less relevant for the functionality of the LIG4 in contrast to the crucial presence of the scaffolding protein XRCC4 [96].

Alternative end-joining (a-EJ) and microhomology-mediated end-joining (MMEJ) are being performed particularly if other factors indispensable for the viability of the c-NHEJ pathway are absent [97]. These pathways are significantly more error-prone and substantially slower than c-NHEJ [97]. Cells lacking XRCC4, Ku70 and LIG4 show increased chromosomal translocations and a higher frequency of deletions (< 100 bp) and insertions (< 10 bp) at the break sites, due to the use of a-EJ [98]. In contrast to c-NHEJ, the use of microhomology at the break ends is more extended [99, 100]. Factors involved in a-EJ are predominantly poly ADP-ribose polymerase 1 (PARP1) [101], C-terminal binding protein 1 (CtBP1) interacting protein (CtIP), MRE11 double strand break repair nuclease (MRE11) [102] and polymerase Θ (Pol Θ) [103]. The immediate switch to alternative end-joining pathways highlights the importance of a fast and reliable ligation of DSBs.

High-LET irradiation induces an increased frequency of short DNA fragments (< 40 bp) due to the high density of DSBs [104]. It is proposed that the binding efficiency of Ku70-Ku80 to DSB ends of short fragments is impeded which in turn leads to a decreased repair using NHEJ [105]. This suppression of the NHEJ pathway can be observed at complex DSBs induced by high-LET irradiation [106]. Additionally, Ku70-Ku80 deficient cells show an increased use of HR, which suggests that the missing binding of Ku70-Ku80 at the DSB site shifts the DDR in favor of homology directed repair (HDR) [107]. Although if repair via HR is not feasible, cells may use more error-prone repair pathways. For instance, NHEJ mutant fibroblasts show increased levels of chromosomal aberrations [108], which emphasizes the protecting role of the NHEJ pathway for chromosomal maintenance.

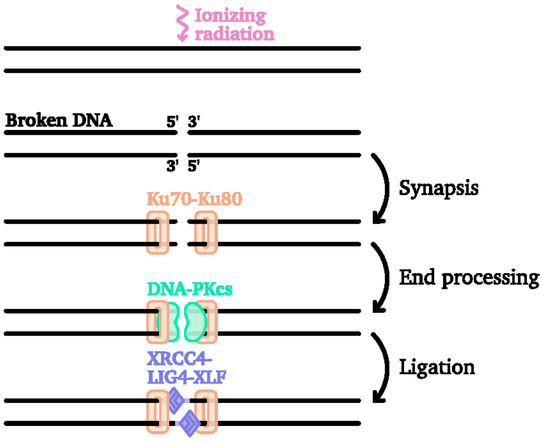

Figure 1.4: DSB repair by non-homologous end-joining. Based on Lieber et al. [109] and Goodarzi and Jeggo [110].

1.2.3 Homologous recombination (HR)

Homologous recombination (figure 1.5) is the other major DSB repair pathway besides NHEJ in mammalian cells [111]. In contrast to NHEJ, HR depends on the intact sister chromatid, identical to the broken strand, to be used as a template and thus can only operate in S and G2 phase of the cell cycle [44, 86, 112]. Moreover, it was shown that HR is predominately active during S phase, with lower activity in G2 and basically no use of HR in early G1 phase [85]. Since this pathway uses the available sister chromatid as a template, the repair of DSBs by HR is supposed to be highly accurate. Although, experiments with yeast show that recombinational repair can also be slightly mutagenic due to the rate of DNA polymerase misincorporation [113]. Besides ionizing-radiation induced DSBs, HR also plays an important role in the repair of DSBs arising from replication fork collapses [114]. DNA end resection at the broken strands is a crucial step before repair via HR can be accomplished, and is initiated by binding of the MRE11-RAD50-NBS1 (MRN) complex to the break site [115]. By endonuclease activity of the dimerized MRE11 at the break ends [116], extended ssDNA overhangs are being produced via 5’ to 3’ end resection.

MRN activity together with other resection related factors as CtIP, exonuclease 1 (EXO1) and DNA replication nuclease 2 (DNA2)/Bloom's syndrome protein (BLM), is further being facilitated by breast cancer type 1 susceptibility protein (BRCA1) [115]. These factors are also in concert with the ssDNA-binding replication protein A (RPA), which is being recruited to resected strand ends for stabilization and to prevent the formation of secondary structures within the ssDNA [117]. RPA is further being replaced by directly interacting with DNA repair protein RAD51 homolog 1 (RAD51) [118], which forms a filament on the ssDNA strand [119] to invade and search the homologous sister strand for the identical base pair sequence [120]. BRCA1, BRCA2 and RAD51 are supposed to co-localize, foremost during S phase, and a depletion of each of those factors seems to have strong adverse effects on genome integrity [121–123]. BRCA1 is furthermore supposed to be responsible for preventing TP53-binding protein 1 (53BP1) binding upon emerging DSBs in favor of HR, while 53BP1-binding itself would promote NHEJ due to the inhibition of resection [124]. Last but not least, with the prerequisite of RAD54-binding, the break will be newly synthesized by DNA polymerases, supposedly α, δ, ε and ζ [125], while ligase I (LIG1) is assumed to be involved in the ligation step [126]. Non-conservative HR, also called single-strand annealing (SSA), is an alternative mechanism of HDR. As HR, SSA depends on resected break ends and instead of a sister chromatid, homologous repeats in proximity to the DSB will be annealed, leading to the removal of DNA patches in between those repeats [127]. Consequently and in contrast to HR, DSB repair by SSA is regarded as more error-prone. Slightly elevated SSA-use at DSBs can be observed for instance in Ku80-deficient cells, while the extend of SSA increases even further if HR is additionally impaired via RAD51-loss [128]. Similar to a-EJ, SSA seems to be the backup option for resected DNA break ends if the main DSB repair pathways are unavailable [128].

The more complex the DSB cluster, the more HR is being used in G2-phase cells [83], although alternative pathways like a-EJ or SSA emerge more frequently with increasing DSB complexity as well [129]. After α-particle irradiation for instance, an increased amount of RPA at DSB sites was observed, indicating that repair at those lesions requires resection [130]. Thus, the extended use of resection seems to be correlated to DSB complexity and DSBs become more resected after high-LET irradiation, even in G1-phase cells [131]. Since the repair accuracy of these alternative mechanisms is significantly inferior, increased use at complex lesions may disrupt the genomic stability by increasing the formation of chromosomal aberrations (CA) [106, 129].

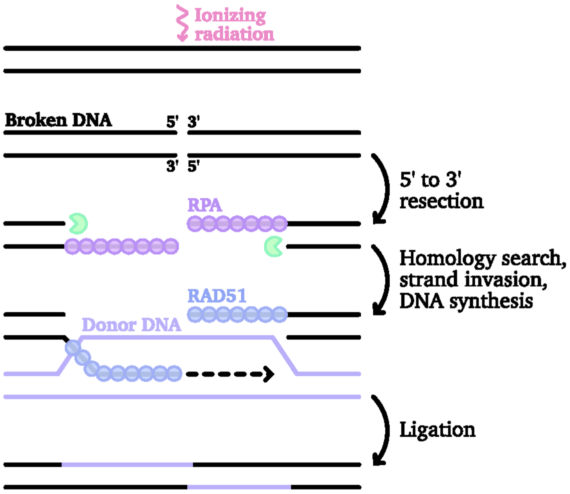

Figure 1.5: DSB repair by homologous recombination with the double Holliday junction (DHJ) sub-pathway. The other sub-pathway, synthesis-dependent strand annealing (SDSA), instead involves just a single HJ and leaves the donor DNA unmodified. Based on Wright, Shah, and Heyer [120] and Nickoloff et al. [132].

1.2.4 Pathway choice and cellular consequences

To prevent cells with damaged chromatin from entering into S phase and to avoid the accumulation of CAs, cell cycle checkpoints, for instance the G1/S checkpoint, can be activated [133]. Although the activation itself does not occur immediately and can take several hours after damage induction by ionizing radiation [134]. Cells irradiated in late G1 phase will enter subsequently S phase even upon unresolved damage [135], while this accumulated damage may be further processed by HR after proceeding into the S phase [85]. Another checkpoint in the G2 phase, G2/M checkpoint, prevents the cell from entering into mitosis with broken DNA strands [136]. However, it was observed that exponentially growing fibroblasts irradiated with 1 Gy X-rays are released from the G2/M checkpoint after a few hours while they still exhibit around 20 DSBs per nucleus [137]. Also cells irradiated with Fe ions leave this G2 checkpoint after some time and enter into mitosis, even though they possess unresolved complex lesions, which subsequently are assumed to lead to the formation of CAs [138].

The chromatin structure is influencing the repair pathway as well. For example, DSBs located in transcriptionally active genomic regions enriched with the histone mark H3K36me3 are supposed to be processed more frequently with HR [139]. With its length of around

2 m with more than 6×10^9 bp [140], the DNA fiber is wrapped around histones to form nucleosomes, while one nucleosome consists of eight histones. Two of each of the four histone family members, H4, H3, H2B and H2A, assemble one nucleosome and in between nucleosomes, H1 serves as a linker histone [141]. The H2A variant H2AX, with a prevalence of 2% to 10% of all mammalian H2A, plays a major role in the DSB response [142]. Upon the induction of a DSB, the ataxia telangiectasia mutated kinase (ATM) phosphorylates H2AX rapidly (1 to 10 min) on the residue serine 139, denoted as γH2AX [142, 143]. Due to the widespread phosphorylation of H2AX involving megabase regions around the DSB [142], the γH2AX signal forms microscopically observable foci and it can be assumed that each focus resembles one DSB [144], although this is only true for sparsely ionizing radiation at low doses where no foci overlap would be expected. Using immune fluorescence (IF) imaging of radiation induced foci (RIF) of γH2AX, the induction and repair of DSBs can be assessed quite precisely [145], while this technique even enables the visualization of heavy-ion tracks via γH2AX and other repair factors accumulating along the track [146]. Frequently after high-LET irradiation, a pan-nuclear γH2AX distribution can be observed, which does not seem to influence the induction of γH2AX at DSB sites [147].

One purpose of the modification of histones is the recruitment and accumulation of further factors involved in DSB repair [148] and chromatin remodeling [149]. Euchromatin (relaxed chromatin) is assumed to be more accessible for repair factors in contrast to the much more dense heterochromatin (condensed chromatin), which can be found predominately at repetitive, pericentromeric and telomeric chromosomal regions with general reduced transcription rates [150]. Subsequently, repair in euchromatin is accelerated and DSBs are resolved faster than in heterochromatin due to the need for decondensation of the dense chromatin structure first [151]. Within the tracks after particle irradiation, the chromatin structure, assessed by transmission electron microscopy (TEM), seems to become less dense in the time frame of 0.5 to 24 h [152].

The consequences for cells exposed to high-LET irradiation reach from genomic mutations and CAs to cancer, senescence and cell killing [24, 153]. Compared to photon irradiation, the relative biological effectiveness (RBE) of particle irradiation increases with LET [154], while the curve's shape depends on the studied biological end point. In the case of cell survival, the RBE reaches a maximum at LET values of around 100 keV/µm to 200 keV/µm after which the RBE declines ("overkill effect") [155]. The RBE is estimated by the ratio of the reference photon dose (D_R), usually X- or γ-rays, to the dose of the specific particle radiation (D_P) at the same biological effect (isoeffect), for instance the same percentage of cell survival:

$$RBE = \frac{D_R}{D_P} \tag{1.2}$$

Importantly, the RBE varies for different cell types as well as particle species and energy [156, 157]. RBE values are especially important in particle-therapy planning to increase the effectiveness in tumor cell killing [157].

Early on it was found that ionizing radiation is an effective initiator of carcinogenesis and neoplastic transformation of mammalian cells [158]. High-LET Fe-ion irradiation in mice for instance induces tumors at higher frequencies and faster onset as compared to the irradiation with γ-rays [159]. Foremost the high number of complex lesions induced by Fe-ion irradiation seems to be repaired with slower kinetics and a substantial fraction of those damage sites remain unrepaired [160] and may even last beyond days [161]. Unresolved complex DSBs increase the frequency of CA-formation which marks Fe-ion irradiation as carcinogenic [162]. It is assumed that two distinct events leading to DSBs are responsible for the formation of each CA [163]. This also requires for both of the DSBs to be left unrepaired for a certain amount of time to have a higher probability for a translocation event [164]. Additionally it is suggested that the breaks of different chromosomes involved in this translocation event have to be very close to each other [165], and experiments show an increased number of DSBs at chromosome borders after carbon-ion irradiation [166]. Nonetheless, DSBs induced by heavy-ion irradiation do not show movement over larger distances which excludes large scale chromatin mobility as the main reason for the occurrence of CAs after ion exposure [167]. Chromosomal exchanges can be classified into simple and complex. The formation of simple exchanges requires two chromatin breaks, while for complex exchanges, at least three breaks in two or more different chromosomes need to be involved [168]. After high-LET irradiation, an elevated frequency of complex chromosomal exchanges in human cells was observed, for instance after α-particle irradiation alone [169, 170] as well as after the exposure to mixed beams of α-particles and X-rays [171]. Interestingly, the number of complex aberrations after mixed beams irradiation increases more than expected for each single radiation quality alone [171]. Mixed beams, which are composed of different radiation qualities with simultaneous low- and high-LET properties, simulate the situation of the exposure to HZE ions and can be used to observe whether effects on the DDR for example are of synergistic or additive nature.

Since the DDR of cells with concurrent higher and lower complex damage is currently not well understood, this work focusses on the processing of DNA damage in human cells after Fe-ion irradiation, as part of the GCR spectrum. The exposure to high-LET ions is cancerogenic [172] and it is of high interest to study the molecular mechanisms leading to a possibly increased health risk of space travellers, considering future deep space missions. Although it is well known that the complex damage produced by ionization events along the trajectory of a charged particle is being processed differently than simple and sparsely distributed photon induced DSBs, it is unknown whether this high damage load has an effect on the processing of the surrounding less complex DSBs emerging from δ-electron interactions. For this purpose, the use of resection as well as HR at δ-electron induced DSBs in cells with at least one Fe-ion hit was studied. Clustered damage in general is being resected more often than single DSBs, suggesting that pathway choice in favor of resection is decided solely by the damage quality itself. Nonetheless, the degree of resection use at DSBs of δ-electron events outside the track region could differ to cells irradiated just with photons, due to the strongly clustered damage in the track region. Depending on the chosen repair pathway, the resolving of DSBs can be more or less time consuming [173]. Thus, besides resection, DSB repair kinetics can provide insight into the efficiency of break rejoining. Last but not least, since adjacent BER processes may lead to the formation of DSBs, the complexity and clustering of proximate DSBs could be increased. This would have significant consequences on the already high damage density within heavy-ion trajectories, as an increased amount of clustered DSBs would be more difficult to resolve efficiently.

Parts of the results of this dissertation have been published in Schwan et al. [174].

2 Material and Methods

2.1 Cell culture

Primary human foreskin fibroblasts (AG1522D, Coriell Institute) and human osteosarcoma cells (U2OS, ATCC (American Type Culture Collection)), as well as U2OS-NBS1-2GFP, kindly provided by Claudia Lukas (Danish Cancer Society, Institute of Cancer Biology in Copenhagen, Denmark) [175], were kept at 95% humidity, 5% CO_2 and 37 °C in Dulbecco's Modified Eagle Medium (DMEM) with 4.5 g/l glucose, 15% fetal bovine serum (FBS) (AG1522D) or 10% FBS (U2OS, U2OS-NBS1-2GFP), 1% non-essential amino acids (AG1522D) and 400 µg/ml Geneticin (G418) with 1 µg/ml Puromycin (U2OS-NBS1-2GFP cells only). AG1522D fibroblasts were accumulated in G1 phase via contact inhibition, while the cumulative doubling time (CPD) was calculated using equation 2.1 to determine the cellular viability numerically in addition to optical observations. With CPD_{old} as the previous CPD, $N_{counted}$ as the number of cells counted and N_{seeded} as the number of cells seeded. Cells in the CPD range of 20 to 30 were seeded for each experiment, since the general viability of passages reaching values well above 30 declined rapidly with increasing numbers of cells detaching from the vessel's bottom.

$$CPD_{new} = CPD_{old} + \frac{\log \frac{N_{counted}}{N_{seeded}}}{\log 2} \tag{2.1}$$

For experiments, cells were seeded either in single 35 mm Petri dishes or on 24x24 or 18x18 mm^2 glass cover slips (#1.5 (170 µm thickness)) for the fixed cell experiments or in chambered coverslips (#1.5) with four wells (ibidi) for live cell imaging. All experiments were performed with 70% to 80% confluency of the cell layer.

2.2 BER inhibitor treatment

To block the BER pathway, a combination of two inhibitors was added to the cell-culture medium, with TH5487, an OGG1 inhibitor and methoxyamine hydrochloride (MX), an

APE1 inhibitor. MX was dissolved in cell culture medium at room temperature with 2x (40 mM) the end concentration of 20 mM. The pH value of the mixture was adjusted between 6.5 to 7.5 using KOH and TH5487 dissolved in DMSO was added with 2x (20 µM) the end concentration of 10 µM. Half of the volume of each cell dish was discarded and replaced with the 2x BERi working solution. Control cells were treated with DMSO, while adding the same volume of DMSO as the volume of TH5487 used in the inhibitor group. Incubation time was at least 1 h at 37 °C prior each experiment and the inhibitor mixture was always prepared shortly before.

2.3 $KBrO_3$ treatment

To induce oxidative base damage, cells were treated with $KBrO_3$ in culture medium. $KBrO_3$ was dissolved in the cell's specific medium to a concentration of 80 mM. Half of each sample's medium was discarded and replaced by the $KBrO_3$ medium, thus, reaching a $KBrO_3$ end concentration of 40 mM. Incubation was carried out at 37 °C for about 1 h, after which the cells were either fixed immediately, see section 2.5 and 2.6, or washed twice with phosphate buffered saline (PBS) and continued incubating with their specific medium without $KBrO_3$.

2.4 Cell irradiation

2.4.1 X-ray irradiation

X-ray irradiation of AG1522D fibroblasts and U2OS cells was performed with a dose of 0.5 Gy and a dose-rate of approximately 2.5 Gy/min. The X-ray tube's peak voltage was set at 250 kV along with the tube current at 16 mA.

For each irradiation session, large Petri dishes (⌀ = 145 mm) containing 8 smaller dishes, were homogeneously irradiated consecutively. Non-irradiated control samples were removed prior irradiation to ensure equal environmental conditions for all groups, including the transportation between laboratories.

2.4.2 Heavy-ion irradiation

Fe-ion irradiation

Iron (Fe) ion irradiation was performed at the GSI synchrotron SIS18 at an energy of 350 MeV/n and a fluence of 3×10^6 particles/cm^2. The resulting LET was around

224 keV/µm and the dose 1 Gy.
Petri dishes were placed inside empty T25 cell culture flasks (figure 2.1) which were subsequently placed on a moving conveyor in front of the beam line to automatically irradiate several stacks of T25 flasks containing the cell dishes without human intervention. Cells were irradiated angular on glass coverslips with a slight tilt towards the beam line by raster scanning over the sample within the irradiation window of 2x2 cm. Control cells were carried to the cave as well and returned to the incubator together with the irradiated ones.
For live cell imaging of the chambered coverslips directly at the beam line, only the outer chambers were irradiated and imaged simultaneously, since the irradiation of directly neighboring chambers may contribute to the dose.

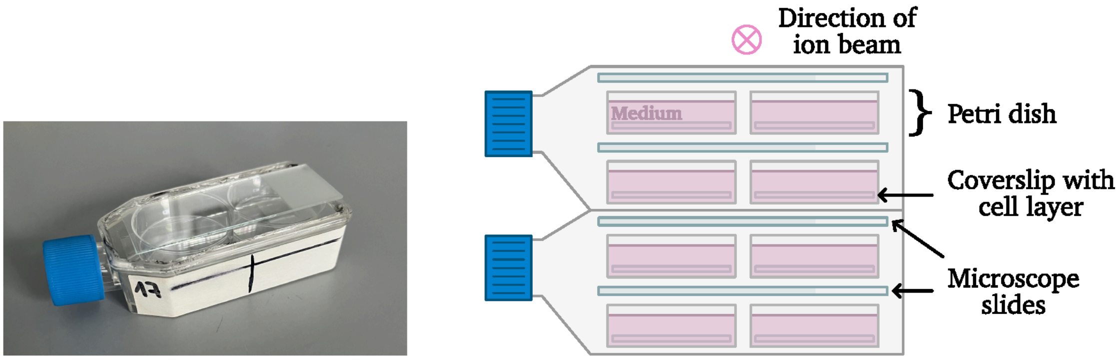

(a) Numbered T25 cell culture flask with removed top part and marked beam target.

(b) Front view of stacked T25 cell culture flasks containing Petri dishes separated by microscope slides.

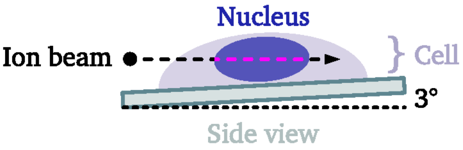

(c) Side view of a cell traversed by an ion.

Figure 2.1: Synchrotron SIS18 irradiation in horizontal direction of Petri dishes inside cut open T25 cell culture flasks. One flask could fit four Petri dishes in total, with two flasks simultaneously irradiated at a time. Additionally, flasks were tilted slightly (around 3°) towards the beam direction.

Li-ion irradiation

Lithium (Li) ion irradiation was performed at the GSI linear accelerator (UNILAC) at an energy of 11.4 MeV/n and a fluence of 3×10^6 particles/cm^2. Neglecting the energy loss in air, the LET within the first water layers would be around 38 keV/µm with a mean dose of 0.18 mGy, although the LET is expected to be slightly higher at the cell layer.
Coverslips containing the cells were placed inside custom designed holders (figure 2.2) and inserted into a tank containing the cell's medium with or without inhibitor. Cells were irradiated consecutively and without medium via lifting each holder in front of the beam window. Due to the low energy and high LET, Li ions were not able to penetrate the accumulated thin medium layer at the lower back. Thus only cells close to the edges are exposed to the ions. After irradiation, all coverslips were removed from the tank and put back into their dedicated sample dish into the incubator. Control cells were carried to the cave as well and returned to the incubator together with the irradiated ones.

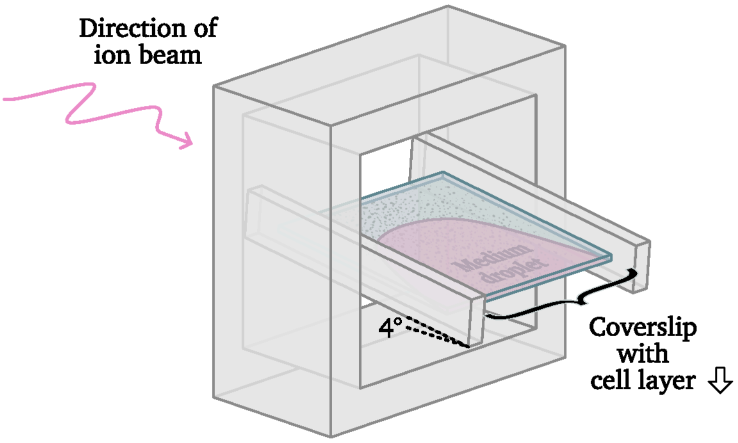

Figure 2.2: Custom cell holder for the horizontal ion irradiation at the UNILAC. Coverslips were inserted upside down with a slight tilt of 4° and the cell layer facing downwards. Only cells outside the thin medium layer were exposed to ions.

2.5 Cell fixation with formaldehyde

Cells were put back into the incubator and fixed at defined time points after $KBrO_3$ treatment or irradiation using 2% formaldehyde solution in phosphate buffered saline (PBS) for 15 min, 0.5% Triton™ X-100 in PBS for 10 min and after two washing steps

with PBS, incubation with 0.4% bovine serum albumin (BSA) with azide in PBS, or just PBS with azide, for at least 30 min or overnight at 4 °C before immunofluorescence (IF) staining was carried out.
If the samples were IF stained with the 8-OxoG antibody, cells were fixed with aceton-methanol instead, see next section 2.6.

2.6 Cell fixation with aceton-methanol

For staining of 8-OxoG base lesions after $KBrO_3$ treatment using the anti-8-hydroxy-2'-deoxyguanosine (8-OxoG) antibody, cells were fixed with −20 °C cold acetone and methanol (1:1) on ice for 20 min. The cell's membranes were subsequently permeabilized using 0.5% Triton™ X-100 in PBS at room temperature for 5 min. For RNA digestion, permeabilized cells were incubated at 37 °C for 1 h with the following buffer: 10 mM Tris-HCl at pH 7.5, 1 mM EDTA, 0.4 mM NaCl and 100 µg/ml RNAse A. The DNA was afterwards denatured using 2.5 N HCl at room temperature for 30 min and subsequently neutralized with 0.1 M $Na_2B_4O_7$ at room temperature for 10 min. Cells subsequently incubated with 0.4% BSA in PBS for 30 min at room temperature or overnight at 4 °C, before 8-OxoG IF staining was performed.

2.7 Immunofluorescence staining

Carl Roth's ROTI®kit for Imaging (EdU Click-647, 7777.1) was used to exclude S-phase nuclei by adding 4 µl of 10 mM 5-ethynyl 2'-deoxyuridine (EdU) to each 2 ml sample dish 15 min prior fixation, to a final concentration of 20 µM per sample. Since pre-incubation with buffer containing BSA before performing the click-reaction deteriorates the signal, PBS was used instead. For the click-reaction mixture with a total volume of 200 µl per dish, following reaction components were added within same order: 151.6 µl millipore water, 20 µl 10x reaction buffer, 8 µl catalyst solution, 0.4 µl 10 mM Eterneon Red 645 Azide or AZDye647-Azide (Jena Bioscience, CLK-1299-1) and 20 µl 10x buffer additive. After incubation with the click-reaction mixture at room temperature for about 30 min, cells were washed twice for 3 min with PBS and blocking for subsequent IF staining procedures was performed by adding 0.4% BSA in PBS for at least 30 min at room temperature or overnight at 4 °C to the cell dish.
After blocking with 0.4% BSA in PBS, blocking buffer was removed and cells were stained by using primary antibodies against Serin 139 phosphorylated histone H2AX (γH2AX), centromere protein F (CENPF), replication protein A 32 kDa subunit (RPA), TP53-binding

protein 1 (53BP1), DNA repair protein RAD51 homolog 1 (RAD51), 8-oxoguanine glycosylase (OGG1) and 8-oxo-2'-deoxyguanosine (8-OxoG) mixed with 0.4% BSA in PBS. Fixed cells incubated for about 1 h at room temperature or overnight (12 h – 16 h) at 4 °C with the primary antibody solution. After primary antibody incubation, cells were washed three times with PBS for 5 min each. Subsequently, cells incubated with the secondary antibodies for 1 h at room temperature. Cells were washed twice with PBS for 5 min each and DNA was stained with 1 µg/ml 4,6-Diamidin-2-phenylindol (DAPI) in PBS for 10 min at room temperature. After incubation with DAPI, cells were washed twice for 5 min with PBS and each coverslip was dipped into millipore water to remove salt residues before attaching the coverslip to the microscope slide with a thin layer of 5 µl to 10 µl SlowFade™ Diamond Antifade Mountant (Invitrogen™). All used antibodies are listed in the following tables, see 2.1 for the primary and 2.2 for the secondary antibodies.

Immunogen	Manufacturer	Clone	Catalogue number	Host	Conc.	IF dil.
γH2AX	Millipore	JBW301	5-636-I	Mouse	1 mg/ml	1:500
53BP1	Calbiochem		PC712	Rabbit	2 mg/ml	1:500
OGG1	Novus Biologicals		NB100-106	Rabbit	1 mg/ml	1:500
CENPF	Novus Biologicals		NB500-101	Rabbit	1 mg/ml	1:750
RAD51	Abcam	14B4	ab213	Mouse	1 mg/ml	1:200
RPA	Santa Cruz	9H8	sc-56770	Mouse	200 µg/ml	1:300
8-OxoG	JaICA	N45.1	JAI-MOG-020P	Mouse	100 µg/ml	1:100

Table 2.1: Primary antibodies used for IF staining.

Name	Manufacturer	Catalogue number	Species	Host	Conc.	IF dil.
Alexa Fluor™ 488	Invitrogen	A11017	anti-Mouse	Goat	2 mg/ml	1:400
Alexa Fluor™ 488	Invitrogen	A11008	anti-Rabbit	Goat	2 mg/ml	1:400
Alexa Fluor™ 568	Invitrogen	A11019	anti-Mouse	Goat	2 mg/ml	1:400
Alexa Fluor™ 568	Invitrogen	A21069	anti-Rabbit	Goat	2 mg/ml	1:400

Table 2.2: Secondary antibodies used for IF staining.

2.8 Image acquisition

Images were acquired using a Leica TCS SPE confocal microscope equipped with a 63x / 1.4 oil immersion lens together with the Leica Application Suite X (LAS X) imaging software (Leica Microsystems) or a Nikon Eclipse Ti spinning disk confocal microscope equipped with a 40x or 100x /1.4 oil immersion lens, an Andor-DU8285 VP-3884 EM-CCD camera and Andor iQ 3 v3.6.1 (Andor Technology) for imaging of fixed and live cell samples. Resolution of acquired images was 0.121 µm/px (40x) or 0.072 µm/px (100x) with an image dimension of 1004 x 1002 pixel. Increment between image slices was set between 0.2 µm to 0.3 µm, with a total amount of 20 to 30 slices per Z-stack.
Directly at the beam line, live cell images of U2OS-NBS1-2GFP cells on chambered coverslips were acquired using a modified remote-controlled OLYMPUS IX73 microscope equipped with an UPlanFL 60x / 1.2 water or 100× / 1.4 oil immersion lens and a 1.6x optovar, an Andor Ixon Ultra DU-888 EM-CCD camera and Andor iQ 3 v3.6.1 (Andor Technology). Image dimensions were 1024 x 1024 pixel, with 0.081 µm/px resolution. Imaging frequency was set to one Z-stack of 7 slices per minute at 12 to 16 locations per sample.

2.9 Image and statistical analysis

For further microscope image processing, image deconvolution with Huygens Essential v19.04 (Scientific Volume Imaging, SVI) was performed. ImageJ v1.53j to v1.54p [176] together with custom developed scripts was used for image analysis and Python v3.9 to v3.13 (Python Software Foundation) along with the main packages Matplotlib, Pandas, Numpy, Scipy and Seaborn was used for generating the plots and performing the statistical evaluation.

2.9.1 Foci analysis

The evaluation of nuclear foci was performed semi-manually on confocal microscope images using ImageJ. After generating a maximum's projection of the Z-stack, thresholding methods, for instance Otsu [177], were used to extract foci from the nuclear background. Due to some variation in background intensity, each thresholded image was manually assessed by eye to minimize over- or underestimation of foci signal.
In cells with ion tracks, damage marker foci with at least 1 µm distance from the track center were assigned as off-track foci, whereas all foci within the track area of less than 2 µm diameter were classified as in-track foci (figure 2.3). Furthermore, only images of

cells with clearly discernible tracks were evaluated to reduce the number of in-track foci misclassified as off-track foci.
To evaluate the fraction of co-localizing foci, an overlay in the maximum projection was generated and the number of overlapping foci of the two different IF markers was assessed. Regarding this, the area of overlap was required to be of sufficient size which was further determined manually by eye to conclude whether the two markers co-localize.

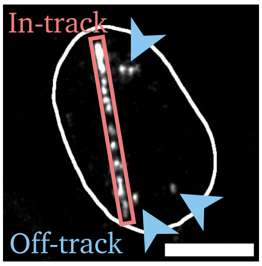

Figure 2.3: Definition of in-track and off-track RIF in cells with ion tracks. DSB markers were used to discriminate between in-track (box) and off-track (arrows) RIF. Only foci with at least 1 μm distant from the track's center were classified as off-track foci. Scale bar: 10 μm.

2.9.2 NBS1-GFP foci emergence time analysis

To determine the emergence time and location of NBS1-GFP foci induced by Fe-ion irradiation, confocal microscope images were processed via using a custom developed ImageJ script. First, each individual focus was highlighted to manually define whether the focus' location was in- or off-track. Next, while going through the time stack, the time point [min] at which the previously classified focus becomes visible was estimated. This so-called foci emergence time was further collected in a table together with the focus' location and the cell's inhibition-status (control or treated with BERi prior irradiation).

2.9.3 Nuclear IF intensity analysis

To quantify the 8-OxoG signal after $KBrO_3$ treatment, see section 2.3, the intensity of the 8-OxoG IF signal within the whole nuclear area was evaluated by generating a maximum projection along the Z-axis. The DAPI signal served as an outline for the nuclear area to measure the mean gray value of the 8-OxoG channel within the nucleus in cells with or without BER inhibitor and at different time points after $KBrO_3$ treatment.

2.9.4 Statistical analysis

If not indicated otherwise, errors show the standard error of the mean (SEM). If needed, for instance after subtracting mean background values from the whole data set, propagation of the SEM was performed with equation 2.2.

$$SEM_j = \sqrt{SEM_i^2 + SEM_{BG}^2} \tag{2.2}$$

With SEM_i as the SEM of the observed values and SEM_{BG} as the SEM of the background. In the case of the γH2AX assay of δ-electrons presented in section 3.4, the calculation of the error bars was slightly modified. First, both sets of the same beam time (Fe-ion beam time of 2022) were averaged, $\bar{x}_1$. This mean value was then averaged with the mean of the other independent beam time (Fe-ion beam time of 2021), $\bar{x}_2$, (equation 2.3). The average background value obtained from this equation, $\bar{x}_{BG}$, was then subtracted from each average, $\bar{x}$, (equation 2.4). Thus, not only error propagation was performed for averaging both mean values but also for subtracting the background values.

$$\bar{x} = \frac{\bar{x}_1 + \bar{x}_2}{2} \tag{2.3}$$

$$\bar{x}_j = \bar{x} - \bar{x}_{BG} \tag{2.4}$$

The standard deviation (SD) ,σ, was obtained from equation 2.5, with x_i as observed values within one data set, $\bar{x}_i$ as the mean value of the observations from this data set and N as the number of observations.

$$\sigma = \sqrt{\frac{\sum_{i=1}^{n}(x_i - \bar{x}_i)^2}{N}} \tag{2.5}$$

The SEM of each data set, SEM, was calculated with equation 2.6, with σ as the SD of the different time points and N as the number of observations.

$$SEM = \frac{\sigma}{\sqrt{N}} \tag{2.6}$$

Since both data sets were averaged with equation 2.3 and background values were subtracted via 2.4, the propagation of the SEM was calculated with 2.7, with SEM_1 as the SEM of the first beam time data set and SEM_2 as the SEM of the second beam time data set as well as the respective SEM of the background values of both sets, SEM_{BG_1} and SEM_{BG_2}, obtained from equation 2.6.

$$SEM_j = \frac{1}{2}\sqrt{SEM_1^2 + SEM_2^2 + SEM_{BG_1}^2 + SEM_{BG_2}^2} \tag{2.7}$$

Data was either represented as point plots, box plots or scatter plots. Point plots show the mean values with error-bars within the range of the SEM or propagation of the SEM, if not indicated otherwise. Box plots depict the range from the first to third quartile (box), while the whiskers extend to the 1.5x inter quartile range (ICR), with outliers outside of this range represented as circles and the line within the box as median. Scatter plots, which show all observations, were combined with point plots to represent the mean and the respective SD. To prevent extended overlapping of data points in scatter plots, random jitter was used to distribute the points position along the X-axis.

Due to the skewed distribution of the foci data, statistical analysis was performed by using the nonparametric Mann-Whitney *U* test and statistical significance was determined by p-values below 0.05. Statistical significance inside plots was indicated by asterisks with the following convention: $p \geq 0.05$ is not shown, $p < 0.05$ is indicated with one asterisk (*), $p \leq 0.01$ with two asterisks (**) and everything below $p \leq 0.001$ with three asterisks (***).

2.10 Flow cytometry

The flow cytometry measurement of normal human fibroblasts (AG1522D) was performed to visualize the cell-cycle distribution in contact-inhibited cell cultures. First, the cells of three separate Petri dishes (⌀ = 35 mm) were detached using 0.5 ml Accutase® (Sigma-Aldrich) for 5 min at 37 °C per Petri dish. The cell suspension was subsequently pipetted up and down several times in order to get single cells, transferred into a 50 ml tube containing 10 ml PBS and centrifuged at 520 g for 8 min at room temperature. After removing the supernatant, the cells were resuspended in 1 ml PBS. 5 ml PBS was then added to the cell suspension, while taking 10 µl of the cell suspension to count by using the TC20 Automated Cell Counter (Bio-Rad). The cell suspension was centrifuged again at 520 g for 8 min at room temperature. After removing the supernatant, the tube containing the cells was inverted onto a napkin to prevent back flow of the PBS. The cells were resuspended in the remaining PBS drop and isolated thoroughly while vortexing. 1 ml of 70% Ethanol per each 1×10^6 cells was added to the cell suspension and the ethanol-fixed cells were stored at least for 30 min at -20 °C.

To stain the DNA for the flow cytometry measurement, 1×10^6 cells of the previously frozen ethanol-fixed sample were transferred into a 15 ml tube and centrifuged at 500 g for 10 min at 4 °C in a swing out bucket. After removing the supernatant, the cells were resuspended in 1 ml PBS and centrifuged again at 500 g for 10 min at 4 °C in a swing out bucket. This time, after removing the supernatant, the cells were resuspended in 425 µl PBS. 50 µl RNAse A was added to the cell suspension and after 20 min of incubation time at 37 °C, DNA was stained via adding propidium iodide (PI) at a concentration of 50 µg/ml to the cell suspension. The cell suspension was then subsequently filtered through a cell strainer cap to remove cell agglutinations and to increase the amount of single cells. Immediately afterwards, the well separated cell suspension was analyzed via flow cytometry using the S3 Cell Sorter (Bio-Rad) with 50 000 events recorded per sample.

Analysis of the gathered flow cytometry data was performed by using FlowJo™ v10.6.2 Software (BD Life Sciences). The area of the side-scattered (SSC) versus area of the forward-scattered (FSC) pulses were plotted to gate for the living cells, whereas gating within the PI fluorescence peak's height versus area subsequently resulted in a population containing foremost single cells. This population served as the input for the cell cycle distribution analysis by generating a histogram of all the PI intensity peak area counts which enabled the annotation of the G1, S and G2/M cell cycle phase peaks.

3 Results

3.1 Induction of DSBs by BER

The repair of clustered base lesions via the well conserved BER pathway may lead to the formation of harmful DSBs, which was observed for instance after X-ray irradiation [74]. In contrast to sparsely ionizing radiation, heavy ions induce clustered lesions in a constrained volume along their track. Due to the narrow distribution of DSBs in the track area, the emergence of additional lesions in direct proximity to the track damage may increase the DSB complexity even further. It can therefore be expected that foremost BER processes within the track region contribute to the DSB clustering. The following section thus investigates the extend of BER-induced DSBs in tracks of heavy ions. To determine the fraction of DSBs which are formed due to BER activity, an inhibitor combination against two BER factors was used. The first part of this section presents some results obtained via inducing oxidative damage in cells treated with and without BER inhibitor to confirm the efficiency of the inhibition.

3.1.1 $KBrO_3$ induces 8-OxoG-base lesions

Potassium bromate ($KBrO_3$) is a strong oxidizing agent that induces damage to DNA bases and was used to investigate the efficacy of the applied BER inhibitor (BERi). To inhibit BER, a combination of the OGG1 inhibitor TH5487 and the APE1 inhibitor methoxyamine hydrochloride (MX) was used. At first, the ability of $KBrO_3$ to induce oxidative base lesions within the experimental conditions of this project was assessed. $KBrO_3$ is able to oxidize DNA within the presence of reduced glutathione (GSH) [178, 179] with 7,8-Dihydro-8-OxoGuanine (8-OxoG) as its main DNA modification [180]. Non-inhibited and BER-inhibited normal human fibroblasts (AG1522D) were treated with $KBrO_3$ for 1 h. After changing back to normal medium, the cells were fixed using ice-cold methanol-aceton immediately (0 h), 15 min, 30 min and 1 h after stopping the $KBrO_3$ treatment. By subsequent IF staining and imaging (figure 3.1) the 8-OxoG signal intensity per time point and condition was assessed (table 3.1 and figure 3.2).

The integrated intensity of the 8-OxoG signal should be proportional to the amount of

8-OxoG antibody bound to the sample and the intensity values between the control and $KBrO_3$ treated samples should thus reflect the induction and consecutive repair of base lesions induced by $KBrO_3$ incubation. As expected, after the $KBrO_3$ treatment the intensity of the 8-OxoG signal increases compared to the control without any prior $KBrO_3$ incubation, with the highest intensity peak 15 min after the 1 h $KBrO_3$ pulse, while 30 min after the $KBrO_3$ treatment the intensity levels decreased tremendously. After 1 h, the intensity values have dropped further, and the 8-OxoG base lesions seem to have decreased nearly completely back to the mean background values, indicating a successful removal of oxidative lesions by the BER pathway. Although there seems to be less 8-OxoG signal directly after removal of $KBrO_3$ in the BER-inhibited sample in contrast to the control group, this difference diminishes with time. Since both groups, with and without BERi, show decreasing 8-OxoG intensities during the 1 h recovery time, 8-OxoG is being effectively removed despite the concurrent OGG1 inhibition.

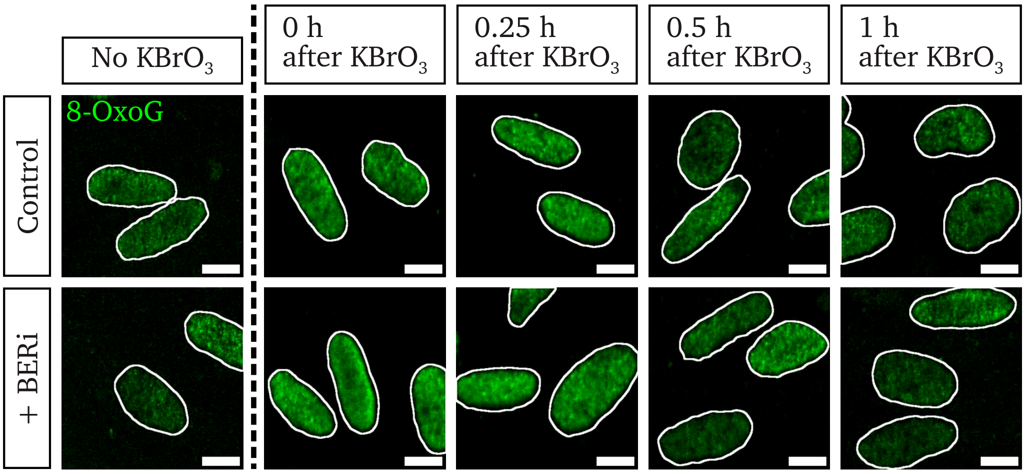

Figure 3.1: IF staining of 8-OxoG (green) in AG1522D fibroblasts with (+ BERi) or without (control) inhibitor pre-incubation, without $KBrO_3$ treatment (no $KBrO_3$) and directly (0 h), 0.25 h, 0.5 h and 1 h after $KBrO_3$ treatment. Scale bar: 10 µm.

Treatment	Time after $KBrO_3$ treatment [h]	Control [mean ± SEM]	BERi [mean ± SEM]
No $KBrO_3$	0	753.8 ± 4.9	729.3 ± 7.8
$KBrO_3$	0	1526 ± 28	1390 ± 31
	0.25	1661 ± 30	1633 ± 30
	0.5	1037 ± 16	1086 ± 11
	1	877.7 ± 9.1	837.8 ± 8.8

Table 3.1: 8-OxoG IF intensity values [A.U.] per nucleus in AG1522D fibroblasts with and without BERi pre-incubation after $KBrO_3$ treatment with corresponding control cells without $KBrO_3$ incubation. With N=2 independent experiments including $n_{Control}$=1118 and n_{BERi}=980 cells.

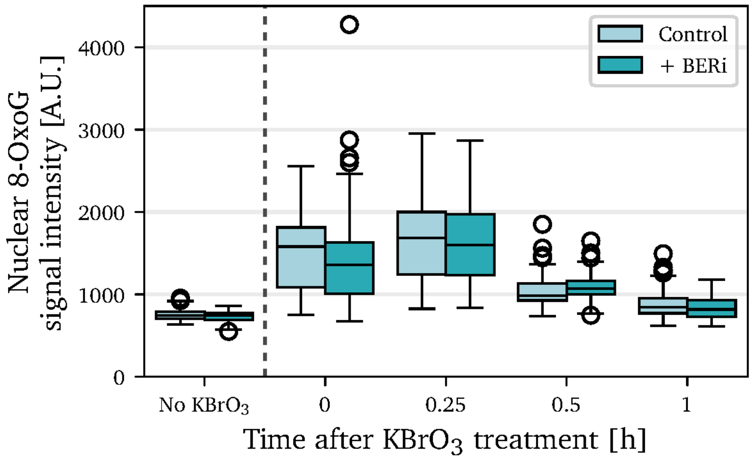

Figure 3.2: **Induction and repair of oxidative base damage after $KBrO_3$ treatment.** 8-OxoG IF intensity values per nucleus in AG1522D fibroblasts with and without BERi pre-incubation after $KBrO_3$ treatment with corresponding control cells without $KBrO_3$ incubation represented on the left side of the dashed line. With N=2 independent experiments including $n_{Control}$=1118 and n_{BERi}=980 cells.

3.1.2 $KBrO_3$ incubation leads to accumulation of DSBs

The previous section, 3.1.1, showed the increase of oxidative base lesions in AG1522D fibroblasts upon treatment with $KBrO_3$. In case a SSB is produced by APE1 activity, a DSB may be generated via concurrent BER processes on the opposite strand, although some inhibition on DSB formation by neighbouring AP-sites and SSBs is expected [70, 181].
To assess the degree of DSB formation during $KBrO_3$ incubation, human osteosarcoma (U2OS) cells tagged with the DSB-marker 53BP1 linked to GFP were imaged directly after adding $KBrO_3$ to the cell's medium (figure 3.3). 53BP1 accumulates at DSB sites and can be observed as foci [182, 183], which co-localize with other DSB markers like γH2AX [145]. With a frequency of one image per 10 min, the amount of 53BP1-GFP foci per nucleus was evaluated to quantify the number of DSBs emerging during 1 h of $KBrO_3$ incubation.
During 1 h of imaging, the mean number of 53BP1-GFP foci per nucleus increases almost perfectly linear with time (figure 3.4). Although the imaging stopped after 1 h, the curve does not seem to change it's shape, suggesting that the amount of observable 53BP1-GFP foci is not yet saturated and could increase further during prolonged $KBrO_3$ incubation.

The linear increase is around 1.8 foci per 10 min $KBrO_3$ incubation time, while the linear shape of the curve indicates ongoing processing and simultaneous induction of base lesions. This first observation of a steady increase in DSBs while cells incubate with $KBrO_3$ suggests that processing of damaged bases in close proximity, presumably due to the high $KBrO_3$ concentration used in this experiment, leads to the formation of significant amounts of detectable DSBs. This indicates the further processing of the $KBrO_3$ induced 8-OxoG lesions measured in the previous section.

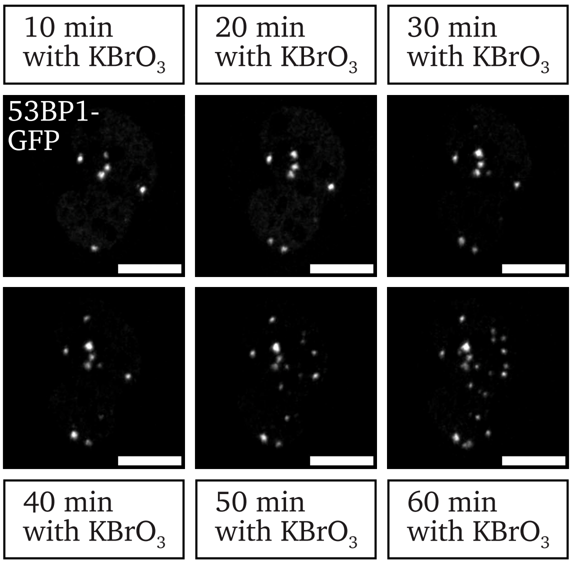

Figure 3.3: Live cell imaging of U2OS-53BP1-GFP cells during 1 h of $KBrO_3$ incubation. Images show the 53BP1-GFP signal (white) of the same nucleus during the time course of 1 h with one image each 10 min. Scale bar: 10 µm.

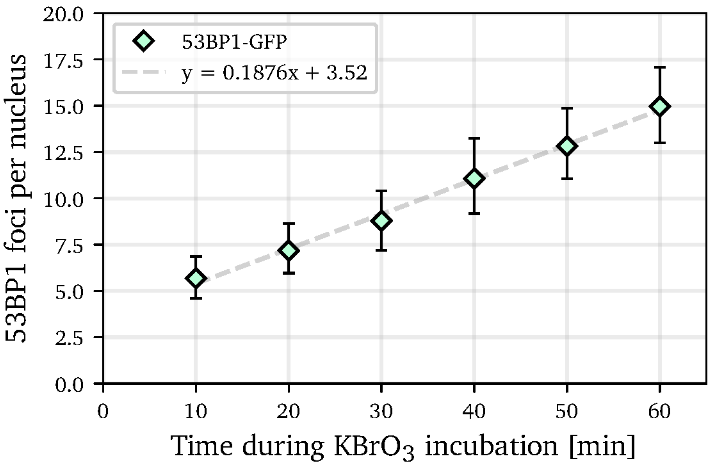

Figure 3.4: **Induction of 53BP1-GFP foci in living cells during $KBrO_3$ incubation.** Number of 53BP1-GFP foci during $KBrO_3$ incubation within live cell imaging of U2OS-53BP1-GFP cells for 1 h with images taken every 10 min. Diamond-shaped dots represent the data's mean per time point with error-bars within the 95% confidence interval. With N=1 experiment including n=28 cells.

3.1.3 A combination of OGG1 and APE1 inhibitor effectively decreases DSB induction by $KBrO_3$ treatment

To compare the impact of BER on the DSB load, inhibitors were used to prevent cells from using the BER pathway. While inhibiting the AP endonuclease activity to prevent the formation of SSBs would also result in decreased numbers of BER-induced DSBs, additional inhibition of an early BER factor could increase the inhibitory effect even further. To test the single BER inhibition against the combination of two BER inhibitors, AG1522D fibroblasts were exposed to $KBrO_3$ for 1 h while being pre-treated with either the OGG1 inhibitor TH5487, the APE1 inhibitor methoxyamine hydrochloride (MX) or a combination of both (BERi). The small molecule inhibitor TH5487 binds at the active site of OGG1 [184] and therefore prevents the direct binding of OGG1 to the base lesion, with 8-OxoG as the main target of OGG1 [185]. MX on the other hand undergoes chemical bonding with deoxyribose directly at AP sites [186, 187], and thus prevents the further processing by the AP-endonuclease APE1 [188]. Since both, APE1 and to a weaker extend OGG1, induce SSBs [65], impairing the activities of both BER factors may lead to an overall stronger BER inhibition.

As observed in the previous experiment (figure 3.4), the incubation with $KBrO_3$ leads to the accumulation of DSBs, which can as well be observed via IF imaging of the DSB marker γH2AX (figure 3.5). To evaluate the effect on the DSB reduction of each inhibitor as well as the inhibitor combination after $KBrO_3$ incubation, γH2AX and OGG1 foci per nucleus have been evaluated (table 3.2). The OGG1 signal hereby served as evidence for the ability of TH5487 to prevent OGG1 binding at lesion sites. Although the additional evaluation of APE1 focus formation in samples treated with the APE1 inhibitor MX would have been an useful indicator for the prevention of APE1 accumulation at AP sites due to MX, the non-specific binding of several APE1 antibodies tested impaired the evaluation substantially and thus are not included in this work.

OGG1, besides the relatively high nuclear background, can be observed as visible foci via IF imaging and co-localizes with γH2AX most of the time. Interestingly, OGG1 tends to accumulate inside nucleoli, as assessed by additional 5-ethynyl uridine (EU) staining (appendix 4.1). As expected, the combination of TH5487 and MX was most effective in reducing both, γH2AX and OGG1 foci almost to the background level of the control samples (figure 3.6). γH2AX foci were reduced by a factor of 7 and OGG1 foci by around 5.7 compared to non-inhibited $KBrO_3$ treated cells. The increase of OGG1 in MX-incubated samples in comparison to the decrease found in TH5487-treated cells could be explained by the inhibitors individual mechanisms. Since TH5487 prevents the active binding of OGG1 to the base lesion [184], it can be expected to observe a diminishing effect on the overall OGG1 signal. In contrast, MX is blocking AP sites for further processing after OGG1 removed the damaged base successfully, while the binding of OGG1 should not be impacted crucially by the mode of action of MX. Looking at the literature, it is well observed that alternative factors can take over main tasks of the BER pathway to ensure the unrestricted progression. The DNA glycosylases NEIL1 and NEIL2 for example may acquire the function of OGG1 in removing 8-OxoG lesions if OGG1's recruitment is hindered through inhibition [68]. This could explain the relatively high DSB amount during OGG1 inhibition, since the BER pathway still seems functional. Using only MX leads to a very significant decrease of DSBs to almost $^1/_4$ of the initial non-inhibited sample treated with $KBrO_3$. In conclusion, the combination of two BER inhibitors, TH5487 and MX, prevents the formation of BER-induced DSBs more pronounced as compared to both inhibitors individually and thus increases the inhibitory effect even further.

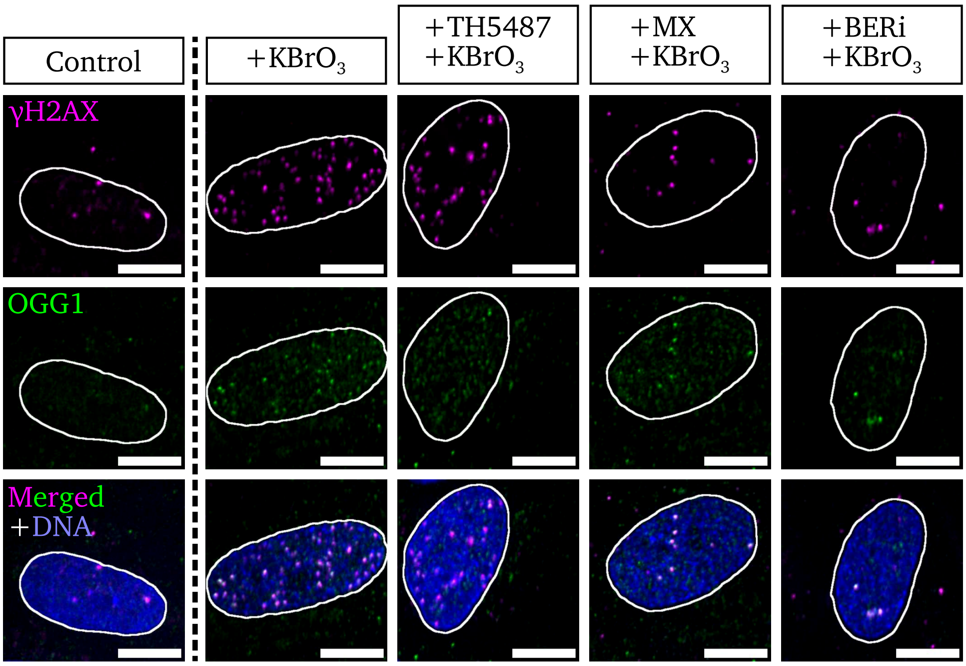

Figure 3.5: IF images of AG1522D fibroblasts stained against the DSB marker γH2AX (magenta), BER marker OGG1 (green) and DNA (blue) before (control) and immediately after $KBrO_3$ treatment, while cells pre-incubated either without inhibitor ($KBrO_3$), with OGG1 inhibitor TH5487 (TH5487 + $KBrO_3$), with APE1 inhibitor MX (MX + $KBrO_3$) or with the combination of both (BERi + $KBrO_3$). Scale bar: 10 µm.

Treatment	γH2AX [mean ± SEM]	OGG1 [mean ± SEM]
Control	3.20 ± 0.46	0.53 ± 0.12
$KBrO_3$	43.0 ± 1.2	52.4 ± 4.5
TH5487 + $KBrO_3$	29.9 ± 1.1	14.0 ± 1.1
MX + $KBrO_3$	11.80 ± 0.61	43.9 ± 2.7
BERi + $KBrO_3$	6.11 ± 0.51	9.15 ± 0.48

Table 3.2: Mean number of γH2AX and OGG1 foci in AG1522D fibroblasts without inhibitor ($KBrO_3$), with TH5487 (TH5487 + $KBrO_3$), with MX (MX + $KBrO_3$) and with the combination of both (BERi + $KBrO_3$) 1 h after $KBrO_3$ incubation. With N=1–2 independent experiments including n=200 cells.

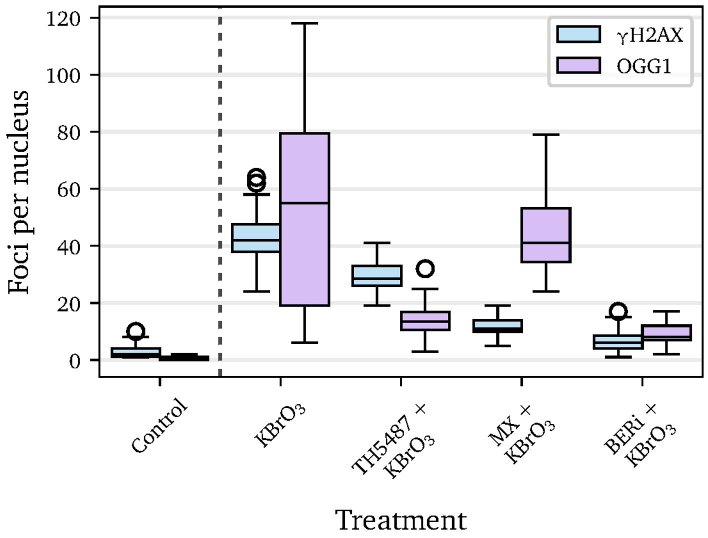

Figure 3.6: **Combination of BER inhibitors prevents BER-induced DSB formation strongly.** Number of γH2AX and OGG1 foci in AG1522D fibroblasts without inhibitor ($KBrO_3$), with TH5487 (TH5487 + $KBrO_3$), with MX (MX + $KBrO_3$) and with the combination of both (BERi + $KBrO_3$) 1 h after $KBrO_3$ incubation. Control samples without inhibitor or $KBrO_3$ treatment are represented to the left of the dashed line. With N=1–2 independent experiments including n=200 cells.

3.1.4 Slow repair of BER-induced DSBs after $KBrO_3$ treatment

To further characterize the quality of $KBrO_3$-induced DSBs, DSB-repair kinetics were performed. Experimentally derived DSB-repair kinetics via the γH2AX assay show the time course of the resolving of γH2AX foci, which is assumed to correlate with the repair of DSBs [44, 189], although with some limitations [145]. Depending on the complexity of the DSB, repair may take longer due to an extended use of resection, which can be observed as the second component of biphasic repair kinetics [190, 191]. Due to the observation of large amounts of DSBs upon the applied $KBrO_3$ concentration, it can be assumed that $KBrO_3$-induced base lesions are densely distributed. This may lead to more complex DSBs accompanied by additional base lesions, reflected by slower repair kinetics. AG1522D fibroblasts were IF stained against γH2AX in the time range of 30 min up to 24 h after treatment and subsequent removal of $KBrO_3$ with or without the pre-incubation of BER inhibitor (figure 3.7).

30 min after $KBrO_3$ treatment, the non-inhibited group's mean γH2AX-foci count reaches a maximum of more than 50 foci per nucleus, whereas the inhibited cells' foci number increases slightly above the background level below 8 foci per nucleus (table 3.3). While a pronounced DSB repair can be observed in non-inhibited cells during the whole time course, BER-inhibited cells show no decline of γH2AX foci. Besides a small increase of less than 4 foci 2 h after $KBrO_3$ treatment in inhibited cells, the foci number of BER-impaired cells remains almost unchanged. At the last measured time point 24 h after $KBrO_3$ treatment, almost 33% of the initial DSB amount seems to be not resolved yet, suggesting that BER-induced DSBs after $KBrO_3$ treatment are processed slowly.

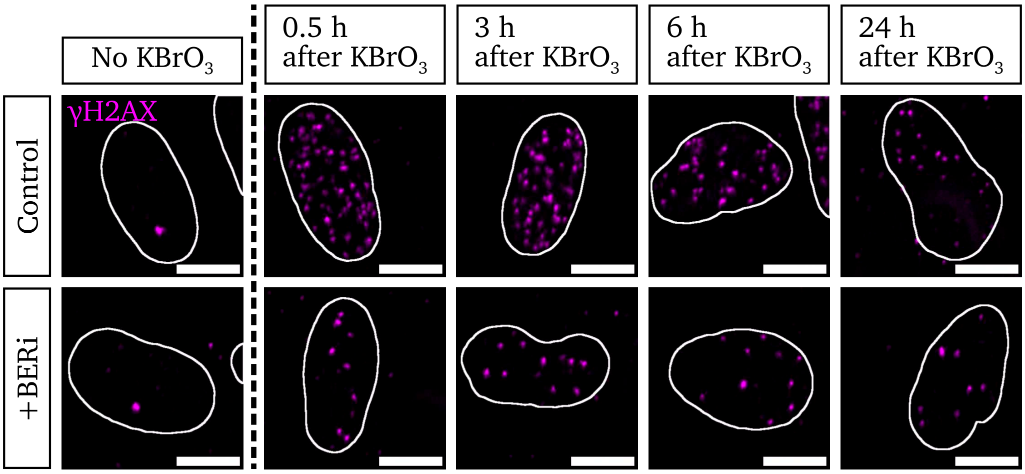

Figure 3.7: IF images of AG1522D fibroblasts stained against the DSB marker γH2AX (magenta) before (no $KBrO_3$) and 30 min, 3 h, 6 h and 24 h after $KBrO_3$ treatment, while cells pre-incubated either with (+ BERi) or without (control) BER inhibitor. Scale bar: 10 µm.

		γH2AX foci	
	Time after $KBrO_3$ treatment [h]	Control [mean ± SEM]	BERi [mean ± SEM]
No $KBrO_3$	0	1.44 ± 0.20	2.56 ± 0.23
$KBrO_3$	0.5	53.9 ± 1.3	7.76 ± 0.32
	1.0	47.6 ± 1.1	8.12 ± 0.34
	2.0	47.2 ± 1.5	11.36 ± 0.62
	3.0	37.1 ± 1.4	11.57 ± 0.52
	6.0	30.6 ± 1.1	10.97 ± 0.70
	24.0	17.65 ± 0.66	8.05 ± 0.78

Table 3.3: γH2AX assay after $KBrO_3$ treatment with (+ BERi) or without (control) BER inhibition in the time course of 30 min up to 24 h after $KBrO_3$ treatment in AG1522D fibroblasts. With N=3 independent experiments including $n_{Control}$=1035 and n_{BERi}=960 cells.

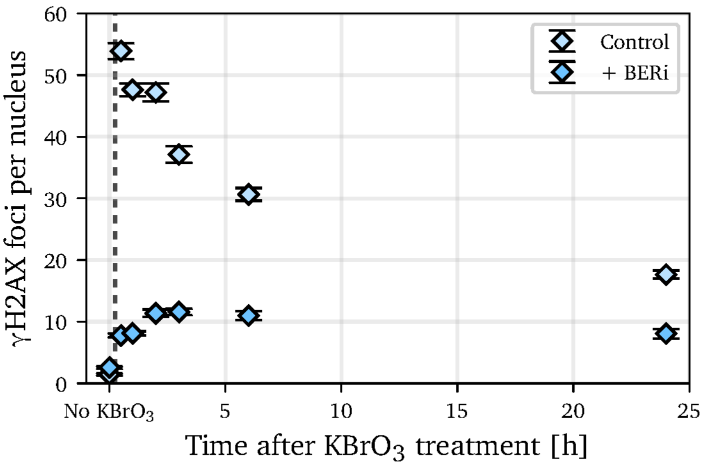

Figure 3.8: **Slow repair of BER-induced DSBs after $KBrO_3$ treatment.** γH2AX assay in AG1522D fibroblasts +/−BERi after $KBrO_3$ treatment. With N=3 independent experiments including $n_{Control}$=1035 and n_{BERi}=960 cells.

3.2 Impact of BER on the DSB load after heavy-ion irradiation

Besides oxidizing agents like $KBrO_3$, a large quantity of base lesions are produced in particular after the exposure to IR [192]. This raises the question whether the transformation of base lesions into DSBs during BER processes adds significantly to the overall DSB load after heavy-ion exposure, and distinctively within the track region. Since the track is composed of highly clustered DSBs, the emergence of additional DSBs due to BER activity can be assumed to increase the general complexity of clustered DSBs even further. Damage clustering impairs the accuracy of DSB repair and may lead to CAs [106]. The exposure to heavy ions and their impact on the genome integrity is especially relevant within space exploration missions.

To study the impact of BER on the induction of additional potentially harmful DSBs under space radiation conditions, AG1522D fibroblasts were irradiated horizontally with 350 MeV/n ^{56}Fe ions at a fluence of 3×10^6 particles/cm^2. The horizontal irradiation geometry with subsequent IF staining and imaging allows for the distinction of heavy-ion induced in-track foci from sparsely distributed δ-electron induced off-track foci. Additional Li-ion irradiation experiments were performed to support the in-track data. With a similar irradiation geometry, fibroblasts were exposed to ^{6}Li ions at energies of 11.4 MeV/n and the same fluence of 3×10^6 particles/cm^2. Due to the relatively low Li-ion energy, emerging δ-electrons are not expected to contribute to the dose outside of the visible track region. In both experimental setups, cells were fixed 15 min, 30 min and 1 h after irradiation and subsequently stained with antibodies against the DSB marker γH2AX and the BER marker OGG1 (figure 3.9). 15 min marks the earliest time point samples became accessible after heavy-ion irradiation.

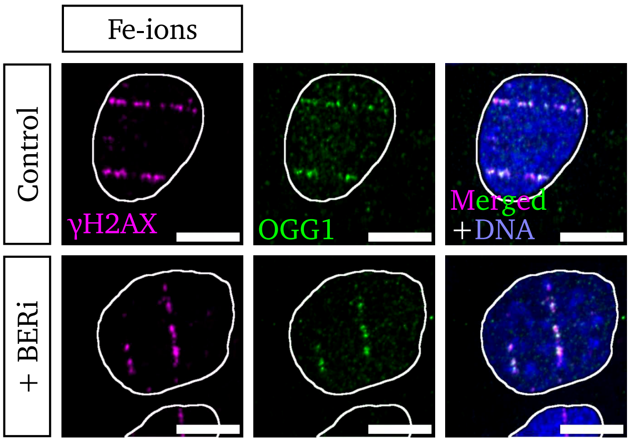

(a) Fe-ion irradiation.

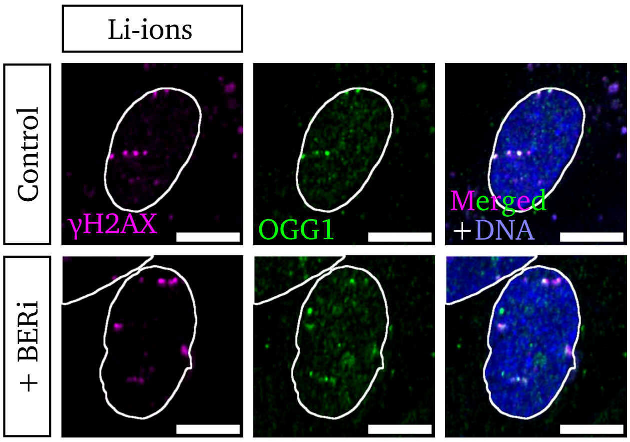

(b) Li-ion irradiation.

Figure 3.9: IF images of AG1522D fibroblasts stained with antibodies against γH2AX (magenta), OGG1 (green) and the DNA stain DAPI (blue) 15 min after (a) Fe-ion irradiation and (b) Li-ion irradiation. Scale bar: 10 µm.

3.2.1 Decreased number of OGG1 foci off-track after Fe-ion irradiation during BER inhibition

To assess the BER activity after Fe- or Li-ion irradiation in cells treated with or without BER inhibitor, the OGG1 signal along the ion track and outside the track region was evaluated per condition. In most cells observed, OGG1 foci accumulate along the ion track in both groups, control and BERi, as verified by the pronounced γH2AX-streaks. Both signals, γH2AX and OGG1, are not perfectly congruent and occasionally, cells with γH2AX tracks and OGG1 background signal do not show OGG1 tracks at all. Since track lengths varied between individual nuclei, the in-track data was normalized with the number of foci per track length, while the latter was measured using the γH2AX signal. Larger gaps within the γH2AX tracks can be explained by the presence of nucleoli [146]. Common in almost all cells assessed was the relatively high and evenly distributed OGG1 background in the whole nucleus. Similar to the $KBrO_3$ data, γH2AX off-track foci usually co-localize with OGG1 foci, although far more off-track OGG1 foci than off-track γH2AX foci for both groups, control and BERi, were observed. Additionally, the off-track OGG1 foci count of non-irradiated cells was subtracted from the OGG1 values of all irradiated cells. The mean value together with the SEM of each condition and time point is listed in table 3.4. 15 min after Fe-ion irradiation, the number of OGG1 foci along the track is lower in the BER-inhibitor treated group in comparison to the control cells (figure 3.10a). In-track, a reduction by around 25% 15 min after Fe-ion irradiation can be observed. Nonetheless, this difference disappears at longer time points, 30 min and 1 h after irradiation. After Li-ion irradiation, there is no difference observable between both groups (figure 3.10c). The Fe-ion off-track data on the other hand (figure 3.10b) shows clearly a lower number of OGG1 foci dispersed around the track in cells treated with BER inhibitor. Off-track OGG1 foci are up to 75% reduced as compared to the control sample 15 min after Fe-ion irradiation. The following later time points show a decrease of more than 90% in contrast to the respective control samples. In general, comparing the numbers of OGG1 foci per track length, Li-ion tracks are composed of less foci per track (between 0.59 foci/µm to 0.976 foci/µm) compared to the numbers of in-track foci observed after Fe-ion irradiation (between 0.758 foci/µm to 1.243 foci/µm). As mentioned at the beginning of this section, it is not expected to observe a dose contribution off-track by δ-electron interaction due to the very short electron-tracks in Li-ion irradiated cells. To conclude the results so far, OGG1 as one of the first factors being recruited to base lesions and hence an early (base) damage responder can be observed in ion tracks within the cellular nucleus. Whereas in the track area itself, the amount of accumulated OGG1 is decreased 15 min after Fe-ion irradiation in cells treated with BER inhibitor prior irradiation. However, this finding could not be replicated by using another ion species with lower LET (Li ions). Outside the trajectory, BER inhibition reduces the number of OGG1 foci massively at all time points. Thus, off-track the recruitment of OGG1 seems to be affected more strongly than in-track in BER-inhibited cells.

Irradiation	Location	Time after irradiation [h]	OGG1 foci Control [mean ± SEM]	 BERi [mean ± SEM]
Fe ions	In-track [foci/µm]	0.25	1.013 ± 0.054	0.758 ± 0.045
		0.5	0.874 ± 0.066	1.010 ± 0.049
		1	1.243 ± 0.071	1.114 ± 0.058
	Off-track	0.25	12.5 ± 2.9	3.2 ± 1.4
		0.5	11.5 ± 2.8	0.49 ± 0.34
		1	21.7 ± 4.6	2.00 ± 0.62
Li ions	In-track [foci/µm]	0.25	0.664 ± 0.055	0.59 ± 0.11
		0.5	0.832 ± 0.073	0.807 ± 0.088
		1	0.976 ± 0.074	0.830 ± 0.072

Table 3.4: Mean number of OGG1 foci per track length (in-track) and per nucleus excluding the track area (off-track) in control or BERi treated AG1522D fibroblasts after Fe-ion or Li-ion irradiation. With N_{Fe}=2 independent experiments including n_{Fe}=397 cells and N_{Li}=1 experiment including n_{Li}=130 cells.

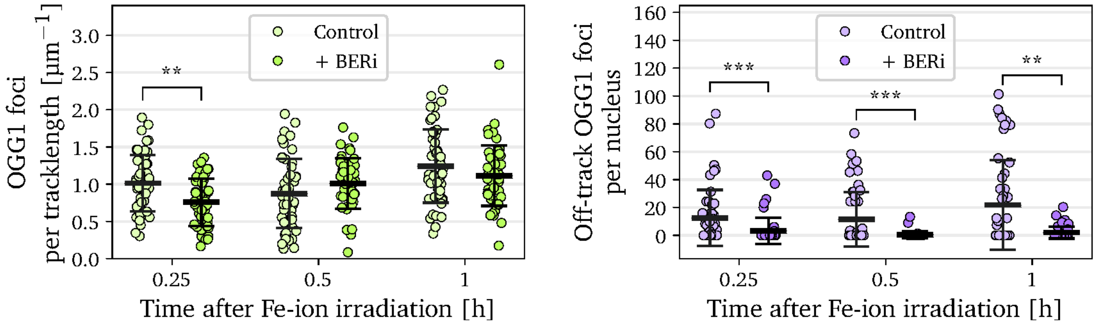

(a) In-track OGG1 foci after Fe-ion irradiation. (b) Off-track OGG1 foci after Fe-ion irradiation.

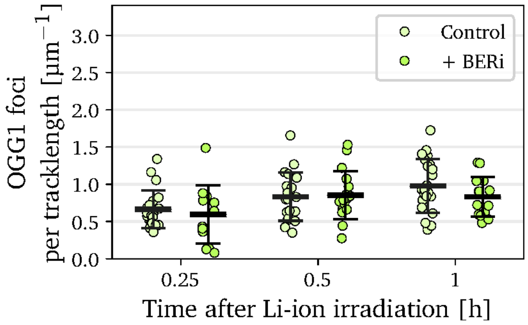

(c) In-track OGG1 foci after Li-ion irradiation.

Figure 3.10: **Less OGG1 foci off-track after Fe-ion irradiation in BER-inhibited cells.** Distribution of (a, c) OGG1 foci per track length and (b) off-track OGG1 foci per nucleus excluding the track area in control or BERi treated AG1522D fibroblasts after (a, b) Fe-ion or (c) Li-ion irradiation. Statistical analysis via Mann-Whitney *U* test: (a) in-track OGG1: p=0.0013 (0.25 h), p=0.062 (0.5 h) and p=0.24 (1 h), (b) off-track OGG1: p=5.9×10^{-5} (0.25 h), p=0.00011 (0.5 h) and p=0.0026 (1 h), (c) in-track OGG1: p=0.67 (0.25 h), p=0.90 (0.5 h) and p=0.27 (1 h). With N_{Fe}=2 independent experiments including n_{Fe}=397 cells and N_{Li}=1 experiment including n_{Li}=130 cells.

3.2.2 BER inhibition causes less DSBs after heavy-ion irradiation

In order to evaluate DSBs along and outside of ion tracks after low angle Fe- or Li-ion irradiation of AG1522D fibroblasts, the γH2AX signal was assessed. Similar to the evaluation of OGG1 foci described in the previous section, the in-track γH2AX foci count was normalized to the track's length. γH2AX foci around the track area have been regarded consequently as off-track DSBs, while γH2AX foci in non-irradiated cells served as background which was subsequently subtracted from all irradiated cells. Table 3.5 lists the mean γH2AX values together with the SEM per time point and condition of the Fe- and Li-ion irradiation experiments.

Comparing the control and inhibitor treated group 15 min after Fe-ion irradiation, the number of γH2AX foci is decreased in BER-inhibitor treated cells by around 13% in-track and 62% off-track (figure 3.11a). While in-track, this difference disappears latest 30 min after irradiation, it can still be observed outside the ion trajectory for the off-track DSBs, with a decrease of 61% 30 min and 21% 1 h after Fe-ion irradiation (figure 3.11b). Similar to the observation of the OGG1 signal, the impact of BER on DSB induction after heavy-ion irradiation seems to be more pronounced for off-track DSBs and the largest difference in DSB numbers are within short times after irradiation. Additionally, BER-inhibited fibroblasts after Li-ion irradiation show decreased numbers of in-track foci per track length 30 min after irradiation (figure 3.11c), although the difference is not significant. Since Li ions have a far smaller nuclear charge (Z) number ($Z_{Li} = 3$) than Fe ions ($Z_{Fe} = 26$), the LET of Li ions at energies of 11.4 MeV/n is far lower than for Fe ions at energies of 350 MeV/n. This LET difference theoretically leads to less DSBs along the track, which can qualitatively be even observed in the acquired IF images of the γH2AX staining (figure 3.9). Less foci could therefore mean less overlap, which may in principle facilitate the observation of additional in-track γH2AX foci in non-inhibited cells. However, the observed difference of in-track γH2AX foci numbers after Li-ion irradiation in cells +/− BER inhibitor is far less pronounced than for Fe ions. Taken together, these findings show that after Fe-ion irradiation, a substantial amount of DSBs outside the track region are induced via BER processes, while the impact on in-track DSBs is less pronounced and foremost only observable shortly after heavy-ion irradiation.

Irradiation	Location	Time after irradiation [h]	γH2AX foci Control [mean ± SEM]	γH2AX foci BERi [mean ± SEM]
Fe ions	In-track [foci/µm]	0.25	0.851 ± 0.024	0.741 ± 0.020
		0.5	0.852 ± 0.026	0.868 ± 0.027
		1	0.807 ± 0.023	0.805 ± 0.027
	Off-track	0.25	5.72 ± 0.69	2.16 ± 0.28
		0.5	5.62 ± 0.52	2.18 ± 0.33
		1	5.19 ± 0.50	4.08 ± 0.35
Li ions	In-track [foci/µm]	0.25	0.657 ± 0.032	0.619 ± 0.070
		0.5	0.727 ± 0.040	0.580 ± 0.039
		1	0.758 ± 0.033	0.729 ± 0.042

Table 3.5: Mean number of γH2AX foci per track length (in-track) and per nucleus excluding the track area (off-track) in control or BERi treated AG1522D fibroblasts after Fe- or Li-ion irradiation. With N_{Fe}=2 independent experiments including n_{Fe}=397 cells and N_{Li}=1 experiment including n_{Li}=130 cells.

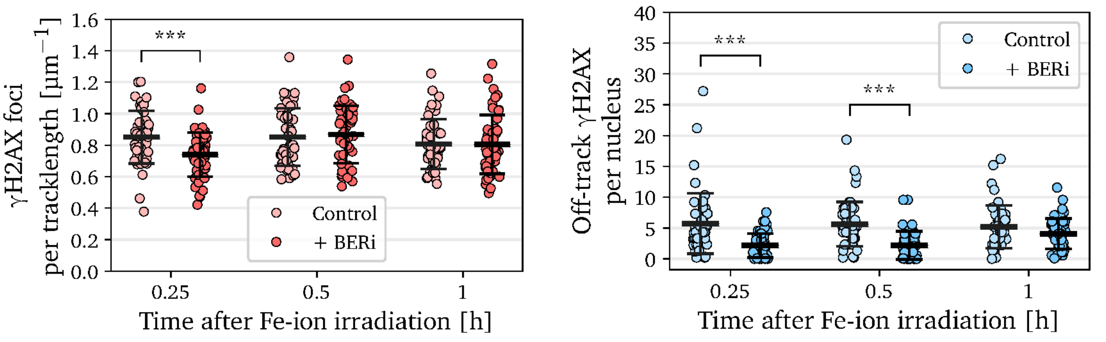

(a) In-track γH2AX foci after Fe-ion irradiation. (b) Off-track γH2AX foci after Fe-ion irradiation.

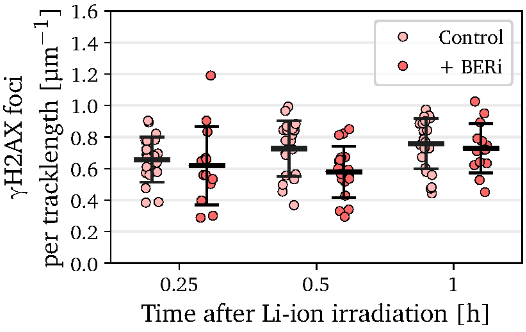

(c) In-track γH2AX foci after Li-ion irradiation.

Figure 3.11: **Less γH2AX foci off-track and in-track after Fe- and Li-ion irradiation in BER-inhibited cells.** Distribution of (a, c) γH2AX foci per track length and (b) γH2AX foci per nucleus excluding the track area in control or BERi treated AG1522D fibroblasts after (a, b) Fe-ion or (c) Li-ion irradiation. Statistical analysis via Mann-Whitney *U* test: (a) In-track γH2AX: p=0.00046 (0.25 h), p=0.66 (0.5 h) and p=0.82 (1 h), (b) off-track γH2AX: $p=1.9 \times 10^{-7}$ (0.25 h), $p=2.8 \times 10^{-8}$ (0.5 h) and p=0.095 (1 h), (c) in-track γH2AX: p=0.27 (0.25 h), p=0.015 (0.5 h) and p=0.44 (1 h). With N_{Fe}=2 independent experiments including n_{Fe}=397 cells and N_{Li}=1 experiment including n_{Li}=130 cells.

To support the hypothesis of an early impact on the DSB load due to BER processes after heavy-ion irradiation, the recruitment of another DSB marker after Fe-ion irradiation was observed via live cell imaging. U2OS cells tagged with NBS1-2GFP were irradiated horizontally with Fe ions at 350 MeV/n with a fluence of 3×10^6 particles/cm^2. The total duration of live cell imaging (figure 3.12) was 45 min, including 1 min of imaging prior irradiation and 44 min of imaging after irradiation with one image stack each minute, directly at the beam line. In-track NBS1-GFP foci were counted along the track and divided by the respective track length and off-track foci were assessed in the area around the track, while the number of background foci to subtract was counted with the image gathered 1 min before irradiation (table 3.6).

Similar to the γH2AX data, NBS1-GFP foci numbers are decreased during the inhibition of the BER pathway, in- as well as off-track, with a reduction of around 26% for in-track and 59% for off-track NBS1-GFP foci (figure 3.13). While in-track, the reduction is higher for NBS1-GFP foci (26%) compared to γH2AX foci (13%) of fixed fibroblasts, the amount of reduced off-track foci is proportionally quite similar (59% less NBS1-GFP foci versus 62% less γH2AX foci during BER inhibition). In contrast to the fixed cell experiments, the sum of NBS1-GFP foci during the whole 44 min of imaging was counted, which leads to increased foci numbers due to the consideration of foci that are only visible for a short amount of time. In contrast to fibroblasts which undergo contact-inhibition at high cell densities, U2OS cells proliferate continuously, leading to a variety of different cell cycle stages (G1, S or G2 phase) within the acquired microscope image data. Due to the higher chromatin content in S and G2 cells at the time of irradiation, higher DSB numbers can be expected [145, 193]. Compared to the fibroblast data (table 3.5), this may explain the increased numbers of observed off-track NBS1-GFP RIF. Nonetheless, the live cell data supports the fixed fibroblast data in regards of showing the reduction of RIF within and around Fe-ion tracks in BER-impaired cells.

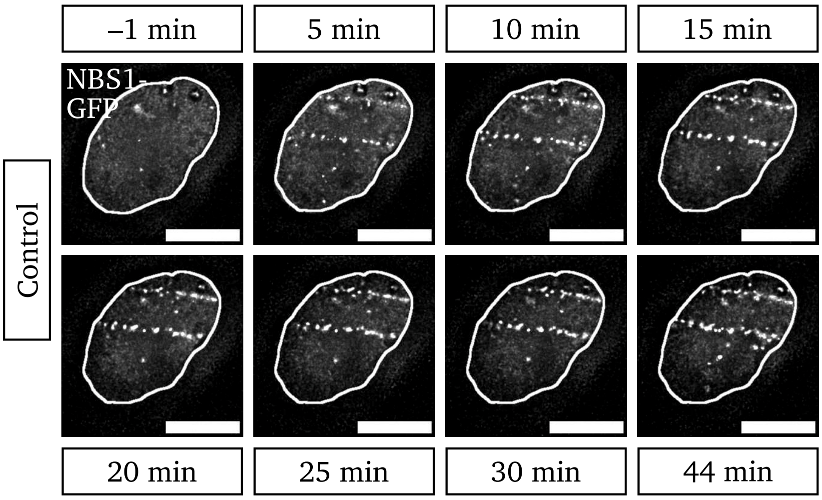

(a) Control.

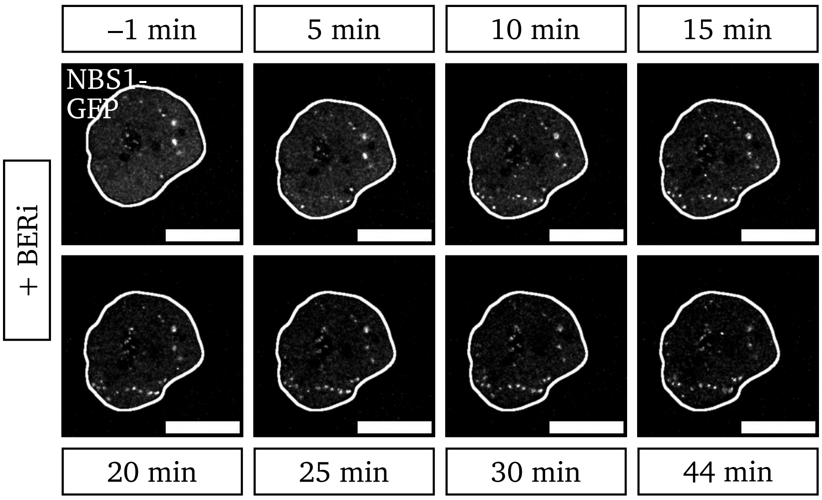

(b) + BERi.

Figure 3.12: Live cell imaging of U2OS cells tagged with the DSB marker NBS1 (U2OS-2GFP) for 45 min with 1 min before and 44 min after horizontal Fe-ion irradiation. With (a) control cells and (b) BER-inhibitor treated cells. Scale bar: 10 µm.

Location	NBS1-GFP foci	
	Control [mean ± SEM]	BERi [mean ± SEM]
In-track [foci/µm]	1.524 ± 0.095	1.125 ± 0.058
Off-track [foci/nucleus]	14.7 ± 3.1	6.1 ± 1.7

Table 3.6: Mean number of NBS1-GFP foci per track length (in-track) and per nucleus excluding the track area (off-track) in control or BERi treated U2OS-NBS1-2GFP cells within 44 min after Fe-ion irradiation. With N=1 experiment including n_{Control}=10−19 and n_{BERi}=9−11 cells.

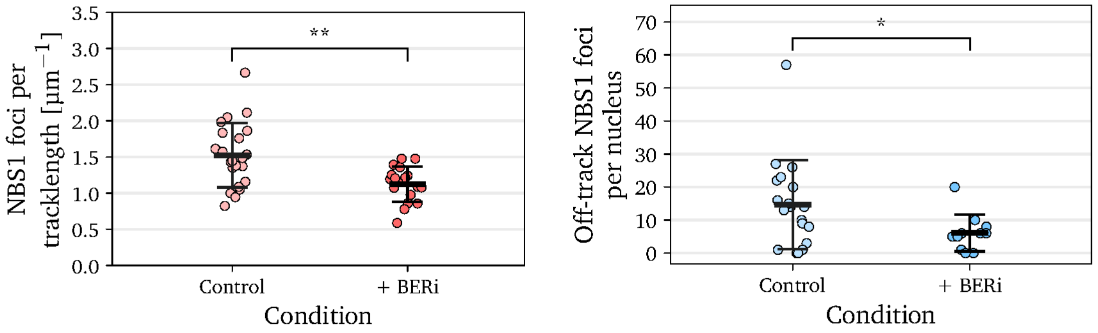

(a) In-track NBS1-GFP foci.

(b) Off-track NBS1-GFP foci.

Figure 3.13: **Less NBS1-GFP foci off-track and in-track during live cell imaging after Fe-ion irradiation in BER-inhibited cells.** NBS1-GFP foci number (a) per track length and (b) per nucleus, excluding the track area in U2OS-NBS1-2GFP cells observed during 45 min of live cell imaging, with 1 min before and 44 min after Fe-ion irradiation. Statistical analysis via Mann-Whitney *U* test: p=0.0032 (in-track) and p=0.040 (off-track). With N=1 experiment including n_{Control}=10−19 and n_{BERi}=9−11 cells.

3.2.3 Delayed emergence time of in-track NBS1-GFP foci after Fe-ion irradiation during BER inhibition

Besides the counting of NBS1-GFP foci, the live cell imaging data was used to assess the time point of focus appearance after Fe-ion irradiation (emergence time). The previous fixed cell experiments suggest that foremost early DSBs may be additionally induced by BER processes and the evaluation of the foci emergence time could further support this assumption. As can be observed in the graphical representation of the data's cumulative distribution function (figure 3.14), the appearance of foremost early in-track NBS1-GFP foci in BER inhibited cells was delayed. Half of the foci are visible 3 min after Fe-ion irradiation in control cells in contrast to 5 min after irradiation in BER-inhibitor treated cells. This difference is even more pronounced one minute later. While around 80% of control cells' NBS1-GFP foci along the track appeared 4 min after Fe-ion irradiation, only 45% of BER impaired cells' NBS1-GFP foci are yet visible. It takes 8 min within the inhibitor group to reach 80% of the maximum foci number inside the ion trajectory. However, no apparent delay was observed within off-track NBS1-GFP foci (data not shown). In conclusion, DSBs seem to be induced foremost in the first 10 min due to BER processes within heavy-ion tracks and BER inhibition leads to the suppression of the induction of those early DSBs.

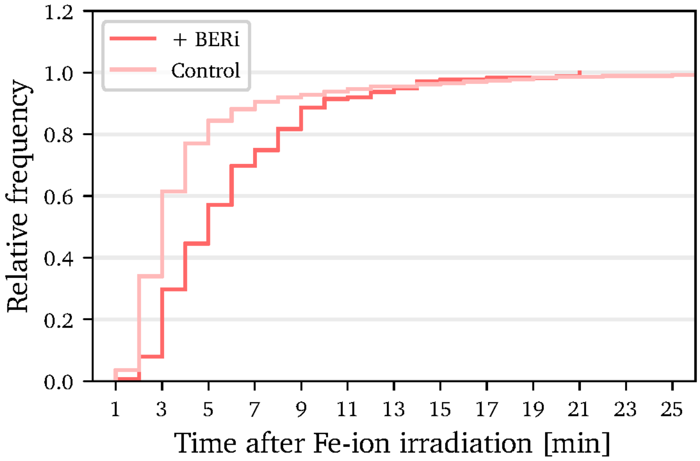

Figure 3.14: **Delayed emergence time of in-track NBS1-GFP foci after Fe-ion irradiation during BER inhibition.** Emergence time of NBS1-GFP foci in U2OS-NBS1-2GFP cells observed during 45 min of live cell imaging, with 1 min before and 44 min after Fe-ion irradiation. The empirical cumulative distribution function (ECDF) represents the data in a cumulative histogram. With N=1 experiment including n_{Control}=17 cells with n_{Control}=371 foci and n_{BERi}=9 cells with n_{BERi}=175 foci.

3.3 Higher resection and HR rates at in- and off-track DSBs after Fe-ion irradiation

3.3.1 Increased resection frequency at in- and off-track DSBs of Fe-ion hit nuclei

High-LET heavy ions induce a plethora of clustered and complex lesions along their path [138, 194–196]. As the previous findings show, BER processes seem to increase the number of DSBs along ion tracks, which may subsequently have consequences on the degree of DSB clustering within this confined track area. To cope with high-complex damage, for instance after particle irradiation, cells perform resection-dependent repair pathways [131, 197]. Resected DSB ends will then further undergo HR or alternative pathways like MMEJ, since extended resection at DSBs has a strong inhibitory effect on NHEJ [83]. Although the complexity of off-track δ-electron induced DSBs is considered to be similar to that of DSBs induced during photon irradiation [28, 74, 198], the concurrent high damage load of the ion track may influence the degree of resection at simpler off-track DSBs additionally.

To study whether DSBs induced by δ-electrons are being processed via resection more frequently in cells directly hit by Fe ions compared to non-hit and photon-irradiated cells, proliferating U2OS cells were irradiated either with 350 MeV/n Fe ions with a fluence of 3×10^6 particles/cm^2 or 0.5 Gy X-rays. Cells were stained 1 h, 2 h and 5 h after irradiation with antibodies against the resection marker RPA and DSB marker 53BP1 (figure 3.15). S-phase cells were excluded via pulse-labeling with EdU. In contrast to the confluent fibroblast culture, U2OS cells divide rapidly and perform no contact inhibition, resulting in a mixed population of different cell cycle phases (data not shown).

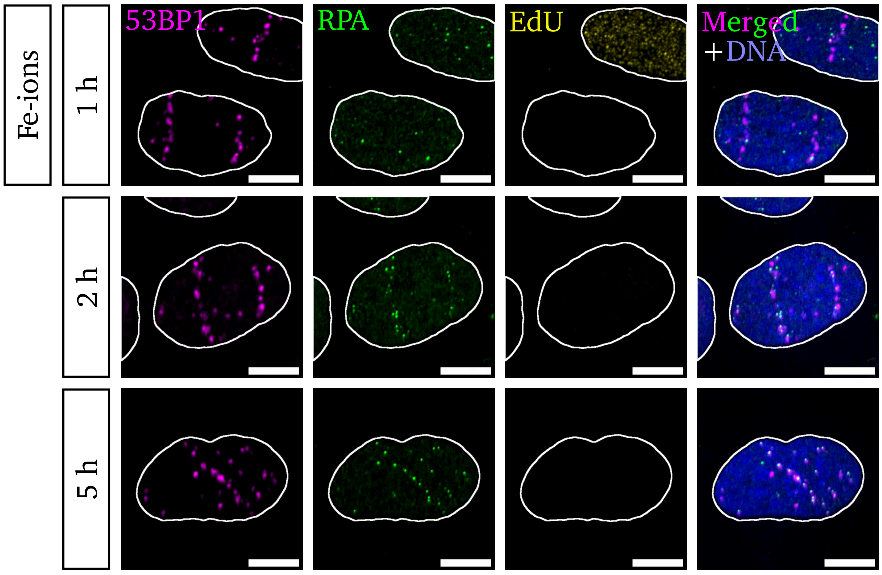

(a) Fe-ion irradiation.

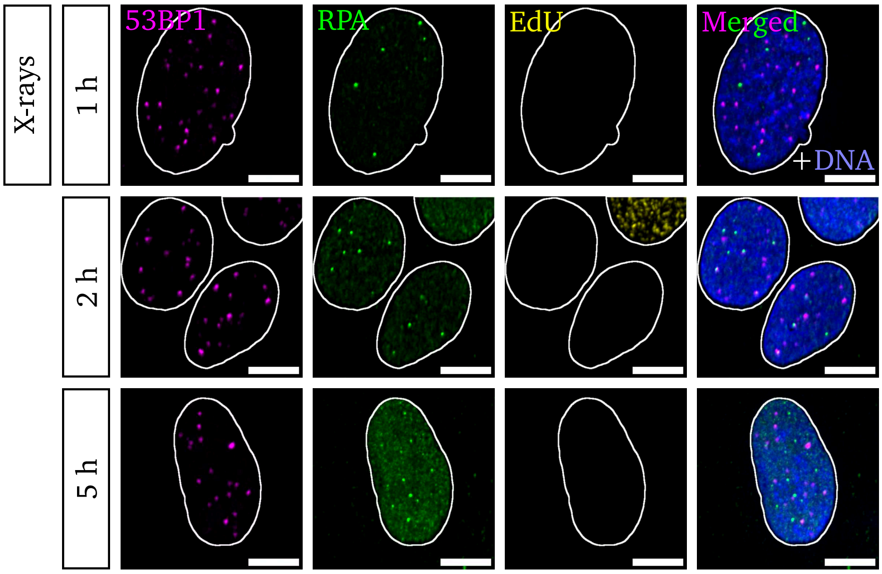

(b) X-ray irradiation.

Figure 3.15: IF images of U2OS cells stained with antibodies against the DSB marker 53BP1 (magenta), resection marker RPA (green), cell cycle marker EdU (yellow) and the DNA stain DAPI (blue) after (a) Fe-ion irradiation or (b) X-ray irradiation. Scale bar: 10 µm.

Out of all the cells evaluated, EdU-positive and RPA-negative nuclei were discarded. This decision was made since radiation-independent DSBs may as well emerge from replication fork collapses in S-phase cells and subsequent repair of these DSBs primarily relies on HR [114]. Mainly EdU-negative nuclei were selected already during image acquisition, leading to low numbers of EdU-positive nuclei in the overall data set. The fraction of resected DSBs was calculated via the amount of RPA foci co-localizing with 53BP1 foci per total 53BP1 foci number, while discriminating between in- and off-track foci (table 3.7). The fraction of in-track RPA-53BP1 foci increases from 31% (1 h) to 61% (5 h), while the fraction observed at off-track foci is lower with 18% (1 h) up to 40% (5 h). Thus off-track, the fraction of RPA positive 53BP1 foci is between 34% and 42% lower than what is observed in-track. The higher RPA frequency at in-track DSBs confirms that repair of complex damage as in ion-tracks requires resection-dependent pathways.

Furthermore, comparing the Fe-ion data with X-ray irradiated cells, it can be observed that the fraction of RPA-positive 53BP1 off-track foci is higher than RPA-positive 53BP1 foci induced by X-rays (table 3.7 and figure 3.16). Just around half of the co-localization events assessed at off-track foci can be observed at X-ray induced RIF within the first 2 h after irradiation. While the fraction of RPA-positive off-track DSBs rapidly increases 5 h after irradiation, it remains low at X-ray induced DSBs. The broad distribution of observations within the Fe-ion dataset (figure 3.16), suggests a higher variation in resection use at in- as well as off-track DSBs in contrast to the smaller SD observed after X-ray irradiation. Nonetheless, off-track DSBs seem to be resected more frequently than X–ray induced DSBs while they show significantly more 53BP1 co-localizing with RPA at all observed time points after Fe-ion irradiation.

To determine whether the presence of complex track damage influences the degree of resection use at off-track DSBs, non-hit nuclei from the same data set were evaluated and added to the overall evaluation. Due to the broad energy deposition of high-energetic δ-electrons after the exposure to HZE ions [26], adjacent nuclei not initially hit by Fe ions show increased numbers of 53BP1 RIF, as compared to non-irradiated control cells. Due to the high fluence of 3×10^6 particles/cm^2 of the Fe-ion irradiation, the average number of ion traversals is theoretically between one and two per nucleus with only a few nuclei having no ion track at all (appendix 4.5). Interestingly, the ratio of RPA positive 53BP1 foci in Fe-ion irradiated but not directly hit nuclei is in between the off-track and X-ray data. The RPA-53BP1 co-localization obtained of nuclei without ion traversal is reduced by 38% compared to the off-track DSBs of nuclei with track but increased by 66% in perspective of the X-ray set. Since the decrease of resection use at δ-electron induced DSBs in non-hit cells is far from significant compared to the off-track data of directly hit cells and due to the scarce amount of non-hit cells that qualified for evaluation, no conclusions can be drawn without repeating the experiment.

Time	Fe-ion irradiation			X-ray irradiation
	In-track [% ± SEM]	Off-track [% ± SEM]	Off-track (no track) [% ± SEM]	[% ± SEM]
1 h	31.3 ± 2.4	18.1 ± 1.5	–	8.4 ± 1.1
2 h	37.2 ± 3.2	24.4 ± 3.0	–	13.2 ± 1.5
5 h	61.2 ± 3.2	40.0 ± 3.8	24.9 ± 7.9	15.0 ± 1.5

Table 3.7: Distribution of the mean percentages of DSB marker 53BP1 co-localizing with resection marker RPA per respective 53BP1 foci amount in- or off-track or per nucleus in U2OS cells after Fe-ion or X-ray irradiation. With N=2–3 independent experiments including n=127–206 cells, except the off-track (no track) data with N=1 experiment and n=7 cells.

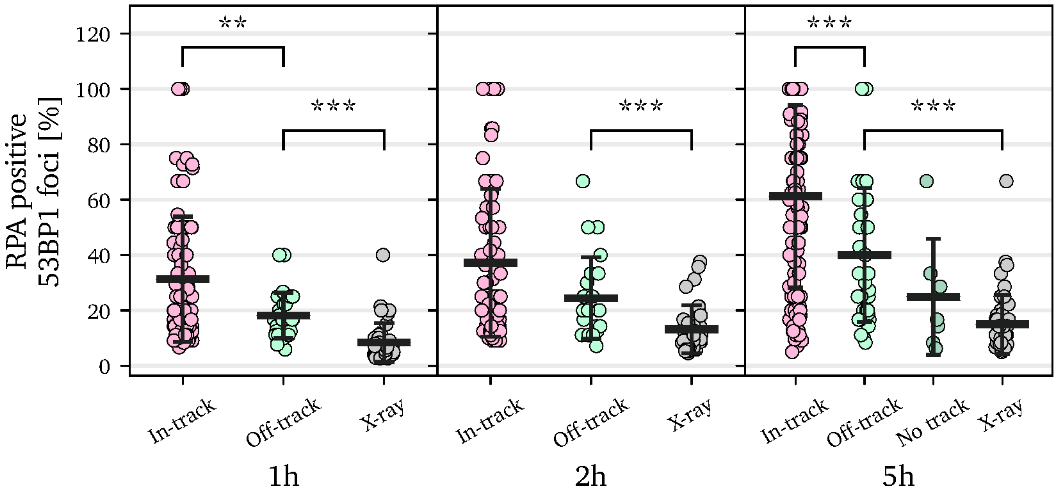

Figure 3.16: **Increased RPA at in- and off-track DSBs after Fe-ion irradiation compared to X-ray induced DSBs.** Fraction of the DSB marker 53BP1 co-localizing with the resection marker RPA in- or off-track after Fe-ion or X-ray irradiation of U2OS cells. Statistical analysis via Mann-Whitney *U* test: In-track vs. off-track: p=0.0058 (1 h), p=0.065 (2 h) and p=0.00078 (5 h); Off-track vs. X-ray: $p=3.7\times10^{-8}$ (1 h), p=0.00016 (2 h) and $p=8.4\times10^{-10}$ (5 h). With N=2–3 independent experiments including n=127–206 cells each, except the off-track (no track) data with N=1 experiment and n=7 cells.

3.3.2 Increased HR frequency at DSBs in- and off-track after Fe-ion irradiation

Extended DNA end resection is a fundamental step for repair by HR [120], and since this pathway relies on homologous sequences in sister chromatids as template, it can be only performed during S and G2 phase in proliferating human cells. Usually, G1- as well as G2-phase cells primarily rely on NHEJ for repair of exogenous DSBs, even with an available template in G2-phase cells [83, 84, 86]. Although NHEJ factors are initially being recruited to almost every DSB site, the repair pathway will switch to resection-dependent HR if NHEJ did not succeed to ligate the break ends promptly [83]. Additionally, already resected DNA break ends with substantially long ssDNA overhangs have a strong inhibitory effect on Ku binding [89], thus promoting HR even further. To follow up with the finding of an increase of resection use at in- and off-track DSBs, the frequency of RAD51 recruitment at DSB sites after Fe-ion irradiation was assessed. U2OS cells were irradiated with either

350 MeV/n Fe ions with a fluence of 3×10^6 particles/cm^2 horizontally or 0.5 Gy X-rays. Subsequently after 2 h of incubation time, the cells were IF stained against the HR marker RAD51 and the DSB marker 53BP1. RAD51 is involved in the homology search and ATP-dependent strand invasion during HR [119, 199] and can be further observed as microscopically detectable foci at high complex lesions, for instance after α-particle irradiation [200]. IF images of RAD51 recruitment after Fe-ion or X-ray irradiation are shown in figure 3.17.

To assess the frequency of HR use at DSB sites, the amount of 53BP1 co-localizing with RAD51 in RAD51-positive cells directly hit by Fe ions was quantified (table 3.8). Similar to the distribution of resection frequency in- and off-track after Fe-ion irradiation (figure 3.3.1), HR signal is found less frequently at off-track DSBs compared to in-track DSBs (figure 3.18). For instance, 38% less RAD51-positive DSBs can be observed off-track. This difference is in line with the resection data that shows 34% less off-track DSBs positive for RPA as compared to the in-track data. Although cells were initially EdU pulse labeled, due to the small sample size and single time point of 2 h after Fe-ion irradiation, cells of all cell cycle phases were included in the HR data set. While S-phase cells may be more frequently RAD51-positive due to HR activity at DSBs emerging during replication [114], the difference of 53BP1 foci showing RAD51 signal between in- and off-track remains almost the same if S-phase cells are included in the overall evaluation (table 3.8). In total, 55% of the cells that are part of this evaluation are EdU positive (predominately S phase) while 45% of the remaining cells account for being most probable in G2 phase. Compared to the resection data set which specifically excludes S-phase cells (table 3.7), the mean percentages of RAD51-positive 53BP1 foci are higher (table 3.8). Since HR is being used more frequently mid-S phase [85], a change in the overall distribution with a higher percentage of DSBs being processed with HR is to be expected if S-phase cells are being included. For instance, excluding S-phase cells from the HR data set shifts the mean percentage of RAD51-positive 53BP1 foci down to 34.7% ± 5.8% and 21.1% ± 3.3% for in-track and off-track DSBs, respectively. These values are quite similar to the fraction of RPA-positive 53BP1 foci with 37.2% ± 3.2% and 24.4% ± 3.0% for in-track and off-track DSBs, respectively. This finding suggests that almost all resected break-ends, in- and off-track after Fe-ion irradiation, are further being processed by HR, with higher HR frequencies at more complex and clustered in-track DSBs.

Between off-track after Fe-ion and X-ray irradiation, a similar difference of RAD51-positive 53BP1 foci can be observed as between RPA co-localizing with 53BP1 of the previous section. After X-ray irradiation, around 52% less RAD51-positive 53BP1 foci can be found compared to off-track DSBs. Although the X-ray HR data set includes S-phase cells as well, the degree of HR use at DSBs (14.5%) is remarkably similar to the frequency of RPA-positive DSBs of the resection data (13.2%) 2 h after X-ray irradiation (table

3.7). In conclusion, Fe-ion irradiation induced off-track DSBs in directly hit cells are more frequently processed by HR, in contrast to similar complex DSBs induced by X-ray irradiation. Together with the resection data, this finding suggests that the presence of complex track damage seems to enhance the nuclear-wide recruitment of resection factors to even lower complex DSBs, while the extend of resection leads to the subsequent processing via the HR pathway.

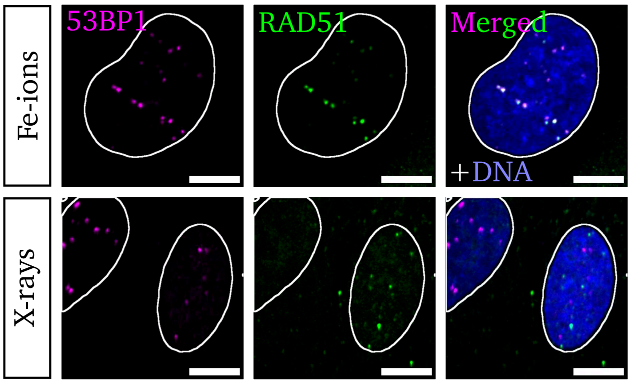

Figure 3.17: IF images of U2OS cells stained against the DSB marker 53BP1 (magenta), HR marker RAD51 (green), and DNA (blue) 2 h after Fe-ion or X-ray irradiation. Scale bar: 10 µm.

Time	Fe-ion irradiation		X-ray irradiation
	In-track [% ± SEM]	Off-track [% ± SEM]	[% ± SEM]
2 h	48.4 ± 3.0	30.1 ± 4.3	14.5 ± 1.5

Table 3.8: Distribution of the mean values of DSB marker 53BP1 foci co-localizing with the HR marker RAD51 per respective 53BP1 foci amount in- or off-track or per nucleus in U2OS cells 2 h after Fe-ion or X-ray irradiation. With N=1–2 independent experiments including n=51–88 cells.

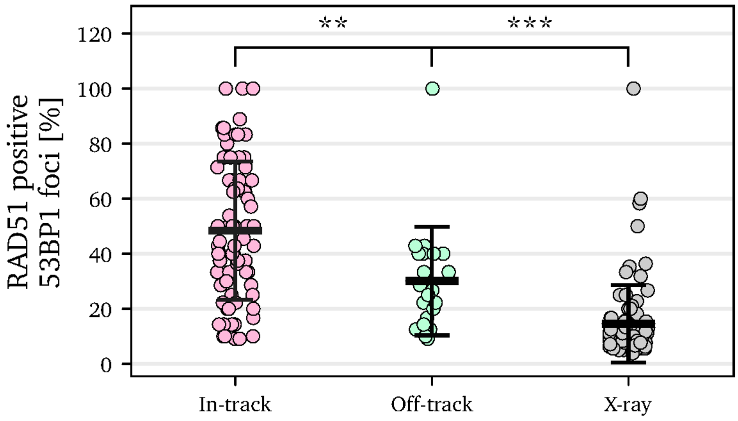

Figure 3.18: **Increased RAD51 at in- and off-track DSBs after Fe-ion irradiation compared to X-ray induced DSBs.** Fraction of the DSB marker 53BP1 co-localizing with the HR marker RAD51 in- or off-track or per nucleus in U2OS cells 2 h after Fe-ion or X-ray irradiation. Statistical analysis via Mann-Whitney *U* test: In-track vs. off-track: p=0.0019 and off-track vs. X-ray: $p=2.0\times10^{-6}$. With N=1–2 independent experiments including n=51–88 cells.

3.3.3 Less HR signal at DSBs in Fe-ion tracks during BER inhibition

Heavy-ion induced clustered and complex DSBs depend on resection to be resolved [197]. BER processes within ion tracks are assumed to increase clustering due to the emergence of additional BER-induced DSBs in close proximity (section 3.2.2). Since the number of RPA foci within DSBs increases with LET [201], it can be hypothesized that RAD51 recruitment may increase with complexity as well. To test this assumption, AG1522D fibroblasts were treated either with or without BER inhibitor and subsequently irradiated horizontally with Fe ions at energies of 350 MeV/n and a fluence of 3×10^6 particles/cm^2. Cells were fixed 3 h after irradiation and IF stained with the DSB marker 53BP1 and HR marker RAD51 (figure 3.19), to assess the fraction of 53BP1 co-localizing with RAD51 (table 3.9, figure 3.20).

During BER inhibition, less RAD51 foci can be observed at in-track DSBs. This suggests that DSBs are less frequently repaired via the HR pathway in presumably S- or G2-phase cells unable to perform BER. Off-track on the other hand, there was no difference in RAD51 recruitment between these two conditions observable (data not shown). However, BER processes are not expected to add significantly to the clustering of δ-electron induced

DSBs due to their dispersed and foremost non-overlapping distribution. Although the number of cells evaluated is quite small due to the low number of S- and G2-phase cells in confluent fibroblast cultures, this finding suggests an impact on DSB clustering by BER processes in Fe-ion tracks. Not only do BER processes lead to additional DSBs after Fe-ion irradiation (section 3.2.2), but those BER-induced DSBs seem to add to the in-track DSB clustering, which are repaired more frequently via resection and subsequently HR in S and G2 cells.

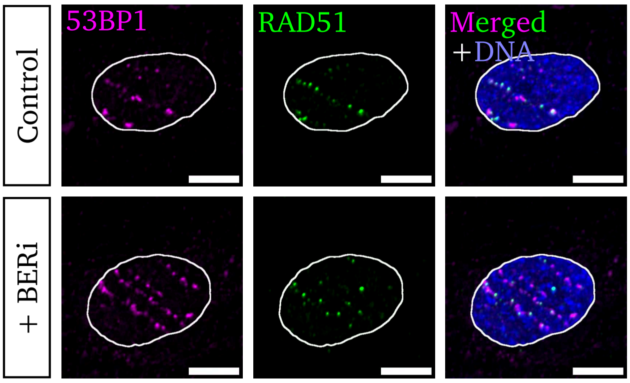

Figure 3.19: IF imaging of AG1522D fibroblasts stained against the DSB marker 53BP1 (magenta), HR marker RAD51 (green) and DNA (blue) with (+ BERi) or without (control) BER inhibitor 3 h after Fe-ion irradiation. Scale bar: 10 µm.

Time	Condition	Fe-ion irradiation
		In-track [% ± SEM]
3 h	Control	62.1 ± 6.1
3 h	BERi	37.8 ± 6.3

Table 3.9: Distribution of the mean values of DSB marker 53BP1 foci co-localizing with the HR marker RAD51 per respective 53BP1 foci amount in- or off-track or per nucleus in AG1522D fibroblasts with (+ BERi) or without (control) BER inhibitor 3 h after Fe-ion irradiation. With N=1 experiment including $n_{Control}$=8 and n_{BERi}=7 cells.

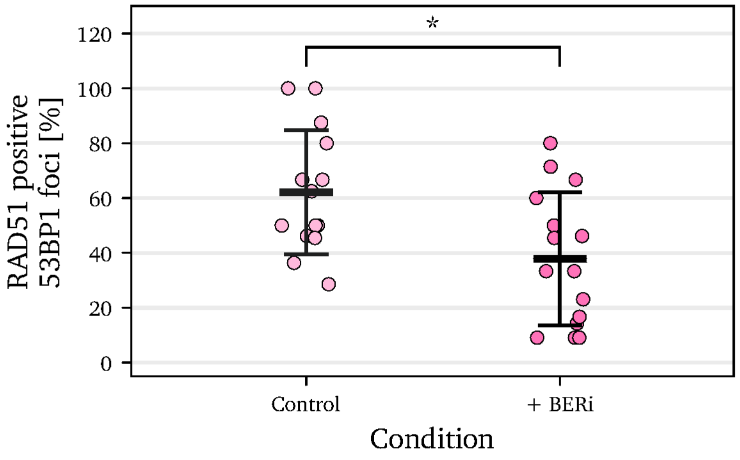

Figure 3.20: **Less RAD51 foci at DSBs in Fe-ion tracks during BER inhibition.** Distribution of DSB marker 53BP1 foci co-localizing with HR marker RAD51 per respective 53BP1 foci amount in-track in AG1522D fibroblasts with (+ BERi) or without (control) BER inhibitor 3 h after Fe-ion irradiation. Statistical analysis via Mann-Whitney *U* test: p= 0.019. With N=1 experiment including n_{Control}=8 and n_{BERi}=7 cells.

3.4 Faster repair of δ-electron (Fe-ion irradiation) induced off-track DSBs compared to X-ray induced DSBs

The previous experiments suggest a different processing of Fe-ion induced off-track DSBs compared to X-ray inflicted DSBs. Resection and foremost HR are being used predominantly in (mid) S and early G2 phase, although as stated earlier, use of resection is as well observed after high-LET irradiation throughout the cell cycle, including G1-phase cells [131]. In fact, this may suggest an increased use of resection at off-track DSBs also in G1-phase cells, as demonstrated in the previous section with a mixed G1- and G2-phase population (section 3.3.1). To further elucidate on the hypothesis of an impact on the processing of off-track DSBs due to the high in-track damage load, repair kinetics via the γH2AX assay in confluent human fibroblasts (mainly G1 phase) within 10 h after 350 MeV/n Fe-ion (off-track) or 0.5 Gy X-ray irradiation were assessed. Resection-dependent pathways, like homology-directed repair, are assumed to be responsible for the slow component of experimentally derived biphasic DSB repair kinetics in G2 cells [83] and resection-dependent alternative end-joining pathways, which are active throughout the cell cycle, are supposed to be slower than the classical NHEJ as well [97]. Thus a direct comparison of repair dynamics in off-track DSBs after heavy-ion irradiation and X-ray induced DSBs could reinforce the hypothesis of a differing off-track DSB processing within the presence of clustered track damage.

To measure DSB repair kinetics, IF staining of AG1522D fibroblasts using antibodies against the DSB marker γH2AX, centromere protein F (CENPF) to label G2-phase cells and the DNA stain DAPI was performed in the time course of 15 min up to 10 h incubation after Fe-ion or X-ray irradiation (figure 3.21). The fibroblasts used in this project have slower proliferation rates as rapid dividing tumor cells, like for instance the human osteosarcoma (U2OS) cell line used prior. Due to their ability of contact-inhibition, confluent fibroblast cultures can be enriched in G1 phase. Although most of the cells were stalled in G1 phase after 10 days of incubation period, see histogram of the cell cycle distribution assessed via flow cytometry 3.22, CENPF staining was used to exclude residual G2-phase cells from the evaluation. To increase the total amount of cells within the evaluation, nuclei with more than one track were included as well. As can be observed in figure 3.23, the number of ion-tracks per nucleus does not influence the repair kinetics of off-track DSBs significantly. Although with increasing numbers of tracks, the off-track area decreases and thus the amount of off-track DSBs, the number of observed γH2AX foci is more or less stable between one track and two tracks per nucleus. Hence, cells with two nuclear ion traversals and thus higher complex damage load seem to be as fast as singly hit cells regarding the repair of δ-electron inflicted DSBs.

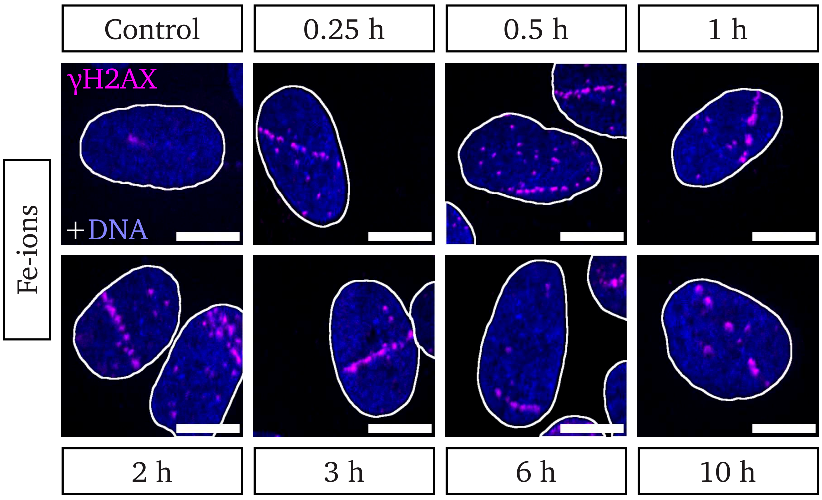

(a) γH2AX assay after Fe-ion irradiation.

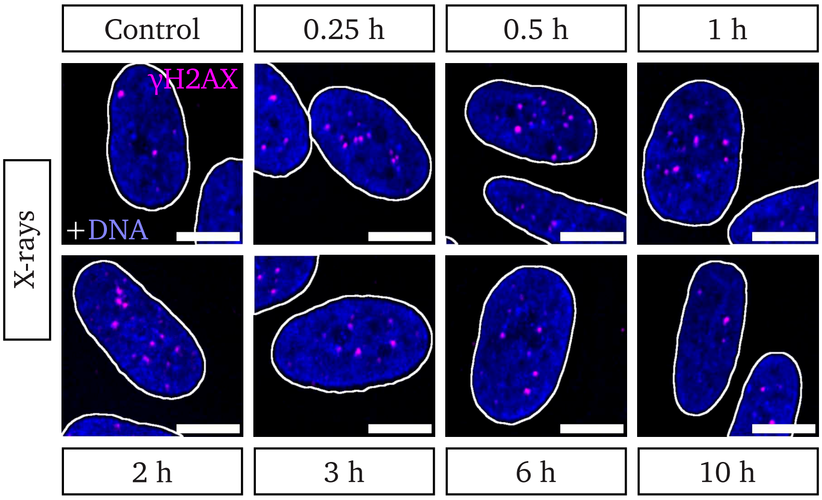

(b) γH2AX assay after X-ray irradiation.

Figure 3.21: IF images of AG1522D fibroblasts stained against the DSB marker γH2AX (magenta) and DNA (blue) after (a) Fe-ion or (b) X-ray irradiation. Scale bar: 10 µm.

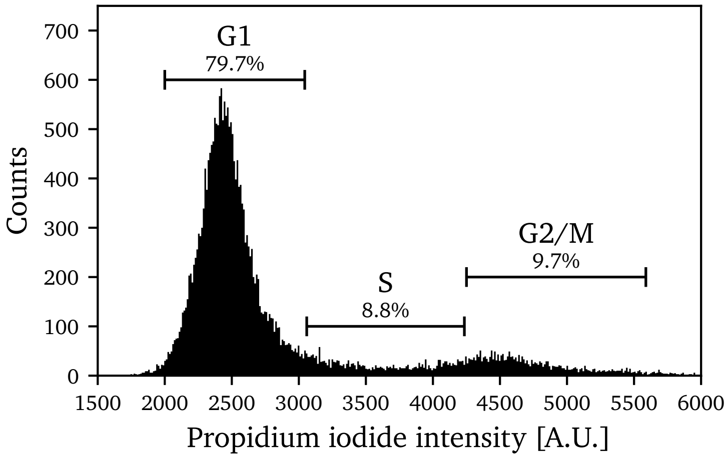

Figure 3.22: **Confluent AG1522D fibroblasts are mainly in G1 phase.** Cell cycle distribution of confluent AG1522D fibroblasts after 10 days in culture measured by flow cytometry via propidium iodide (PI) staining. With N=1 experiment including n=24 997 cells.

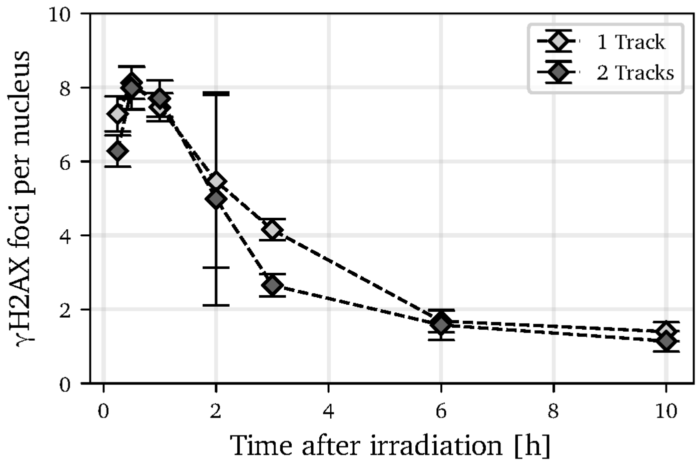

Figure 3.23: **Similar repair kinetics for off-track DSBs in cells traversed by one or two Fe ions.** Mean number of off-track γH2AX foci per nucleus in AG1522D fibroblasts after Fe-ion irradiation with either one or two ion traversals. With N=2 independent experiments including n=1248 cells.

In general there are less off-track DSBs observable in Fe-ion irradiated fibroblasts compared to the X-ray counterpart (figure 3.24a). After an initial rise to a maximum number of γH2AX foci 30 min after irradiation for both radiation qualities, surprisingly, the number of δ-electron induced γH2AX foci seems to decline faster than the amount of X-ray induced γH2AX foci. The difference can be observed more clearly while normalizing both data sets to the highest foci count 30 min after irradiation (figure 3.24b). To gain more detailed insight into this apparent difference and to diminish the impact of any data normalization that was used to prepare figure 3.24b, the logarithm of the non-normalized mean values was fitted via linear regression (figure 3.24c). Since the exponential decline is most pronounced in the segment between 1 h and 6 h, the linear regression was performed solely within this time interval. By retrieving the fitting parameters, the difference in inclination for both radiation qualities can be assessed. The repair curve of X-ray inflicted DSBs is less steep (slope ± SD: $-0.2463\ \mathrm{h}^{-1} \pm 0.0093\ \mathrm{h}^{-1}$) than the repair curve of δ-electron induced DSBs (slope ± SD: $-0.306\ \mathrm{h}^{-1} \pm 0.012\ \mathrm{h}^{-1}$), supporting the observation of the faster repair of δ-electron induced DSBs. The time point at which half of the initial amount of RIF has disappeared, can be calculated using the fitting coefficients and the half-life equation $t_{1/2} = \frac{\ln 2}{\lambda}$ which leads to 2.81 h ± 0.11 h and 2.263 h ± 0.084 h for the X-ray and δ-electron data set, respectively. Although repair kinetics of DSBs in general are assumed to be biphasic with a fast and slow component [202], these biphasic tendencies are not evident in the curves represented in 3.24. The slow part of DSB repair kinetics usually starts past 10 h after exposure to IR [83], which is the last time point in the repair kinetics in 3.24. Due to the decreasing number of cells showing a complete ion track more than 10 h after irradiation, later time points were not assessed.

To strengthen the hypothesis of an enhanced DDR at off-track DSBs due to the concurrent complex track damage, non-hit cells exposed to δ-electrons were evaluated as well. Unexpectedly, cells without track show higher fluctuations regarding the number of γH2AX foci per time point. For instance, non-hit cells show two maxima, one at 30 min (not shown) and, surprisingly, another one at 2 h after Fe-ion irradiation (figure 3.24c). This impedes a direct comparison to the other two kinetics and a repetition of this experiment is indispensable to prove the impact of track damage on the nuclear wide enhancement on the DDR.

In conclusion, the simultaneous presence of clustered track damage seems to enhance repair at simpler off-track DSBs in foremost G1-phase fibroblasts.

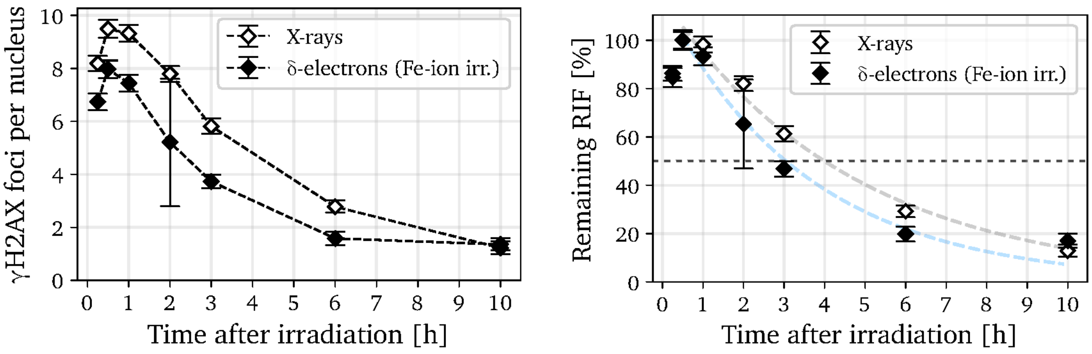

(a) Mean number of γH2AX foci per nucleus.

(b) Remaining γH2AX foci per nucleus with exponential fit: y_X=117.5 $e^{-0.214\,x}$ and y_δ=116.8 $e^{-0.279\,x}$.

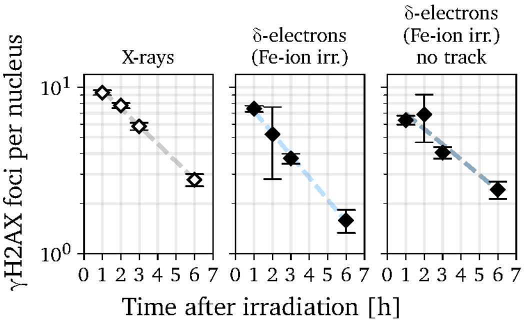

(c) Logarithmic representation of the mean γH2AX foci number per nucleus with linear fit.

Figure 3.24: **Faster repair kinetics for off-track DSBs after Fe-ion irradiation.** (a) Mean number of γH2AX foci and (b) remaining γH2AX foci in AG1522D fibroblasts after X-ray or Fe-ion irradiation. (c) Logarithmic representation of the mean γH2AX foci number between 1 h and 6 h after irradiation with linear regression and additional Fe-ion data set including non-hit cells (no track). Linear fitting parameters are as follows: X-ray: y_X=−0.2463 x + 2.506, Fe ion δ-electrons: y_δ=−0.306 x + 2.278 and Fe ion δ-electrons no track: $y_{\delta,\text{-track}}$=−0.213 x + 2.15. Error-bars are within the propagation of the SEM. With N=2−3 independent experiments including n=1223−1786 cells.

4 Discussion

The scope of this work was to investigate the impact of HZE ions on the DDR *in vitro*, regarding the influence of base repair to the overall DSB load as well as the impact of clustered track damage on the nuclear wide processing of δ-electron induced DSBs. For this purpose, human cells were irradiated with high-LET Fe ions and IF stained with several factors involved in BER and DSB repair. The horizontal irradiation geometry enabled the visualization of heavy-ion tracks surrounded by δ-electron inflicted DSBs.

4.1 BER leads to increased DSB load after heavy-ion irradiation

To study the impact of BER on the DSB load via IF staining against γH2AX in cells exposed to heavy ions, human fibroblasts were pre-incubated with a combination of BER inhibitors and compared to non-treated control cells. Combining two inhibitors was significantly more effective in reducing DSBs than each inhibitor on its own (figure 3.6). While the inhibitor effect on the reduction of γH2AX and OGG1 foci number was quite pronounced, there was no difference observable on the resolving of 8-OxoG base lesions in inhibitor-treated cells (figure 3.2), as opposed to similar studies [184, 203]. Although OGG1 is the main glycosylase regarding the excision of 8-OxoG, other factors may take over this task if the function of OGG1 is compromised. For instance, NEIL1 can excise base lesions, primarily oxidized pyrimidine lesions, like Tg and 5-OHU, and to a smaller degree oxidized purine lesions, like 8-OxoG, and thus effectively compensate for the loss of OGG1 [67, 68]. Nonetheless, the 8-OxoG data suggests that the major fraction (control: 69%, BERi: 61%) of base lesions are being resolved within 30 min after damage induction by $KBrO_3$ incubation and subsequent removal. Although cells were washed twice with PBS after $KBrO_3$ treatment, the slight increase of 8-OxoG signal between 0 min and 15 min suggests that residual nuclear low concentrations of $KBrO_3$ further induce base lesions at a higher rate than the base removal during BER. The pronounced decline 15 to 30 min after damage induction suggests a high BER activity with an efficient 8-OxoG base removal at foremost early time points.

The repair of $KBrO_3$ induced base lesions via the BER pathway leads to significant amounts of DSBs (figure 3.6 and 3.8). These BER-induced DSBs seem to be repaired particularly slow, especially when compared to the DSB repair after X-ray irradiation (appendix 4.3). This observation leads to the following assumptions: In non-inhibited cells, BER-induced DSBs may be more complex and hence processed more slowly as observed by the overall slow decline and the well noticeable remaining fraction of DSBs 24 h after $KBrO_3$ treatment. On the other hand it cannot be excluded that residual traces of nuclear $KBrO_3$ lead to ongoing BER activity above the endogenous level. Additional BER processes thus may induce DSBs during the whole time course of the experiment, resulting in simultaneous DSB repair and induction. If DSB repair rates are higher than the rates for induction, overall slower repair kinetics may be observed. Due to the ambiguity of the interpretation, statements regarding the DSB quality upon $KBrO_3$ treatment should be made with caution. Experiments with the oxidizing agent $KBrO_3$ were performed at high concentrations of 40 mM and the mechanism of damage differs distinctly to the damage induction by exposure to IR. In contrast to IR, bromine dioxide BrO_2, bromine monoxide BrO radicals and bromine $Br^\bullet$ radicals are assumed to be the main cause for the generation of 8-OxoG during the treatment with $KBrO_3$ [179]. Ionizing radiation on the other hand most prevalently leads to the production of hydroxyl ($^\bullet HO$) radicals [180] and non-radical oxidants like hydrogen peroxide (H_2O_2) [179]. Interestingly, the presence of intracellular antioxidants such as glutathione (GSH) are required for the base damaging effect of $KBrO_3$ [180]. Nonetheless, despite those differences in mechanism of action between IR and $KBrO_3$, the number of observable OGG1 and γH2AX foci is strongly reduced in BER-impaired cells exposed to heavy ions or $KBrO_3$. Surprisingly, the number of 53BP1-GFP foci upon $KBrO_3$ treatment was far less enhanced in non-inhibited cells compared to the large amount of γH2AX foci (figure 3.4). Considerably lower 53BP1 foci numbers were also observed in fixed and IF stained AG1522D fibroblasts (appendix 4.2). The accumulation of 53BP1 proteins at DSB sites is supposed to undergo liquid-liquid phase separation [204, 205]. Liquid-liquid phase separation describes the formation of two phases with high and low densities, allowing for a closed compartment of the dense phase and exchange with the diluted phase [206]. They can be found for instance in membraneless organelles like the nucleolus and nuclear speckles [206]. These compartments seem to be disrupted during osmotic stress induced by the administration of sorbitol or salt [204], thus preventing foci formation. Since $KBrO_3$ is the potassium salt of bromic acid and the assessment of 53BP1 foci formation was done during or immediately after $KBrO_3$ treatment, it could be possible that salt-induced changes in osmotic pressure prevented the accumulation of 53BP1 at DSBs. This would also be supported by the unaffected γH2AX foci formation, since this histone modification does not seem to be influenced by osmotic stress [204]. However, the osmotic concentration of the applied $KBrO_3$ treatment with around $c_{osm} = 80\,\text{mosmol/l}$ was far lower than the concentration of the NaCl solution with $c_{osm} = 500\,\text{mosmol/l}$, as described in [204], which seemed to effectively prevent 53BP1-GFP foci formation. In addition, the number of 53BP1 foci remains quite low even after the complete removal of $KBrO_3$ (appendix 4.2). Hence, the reason for this discrepancy cannot be explained solely by differences in osmotic concentration and needs to be explored further.

The OGG1 signal served the purpose to monitor the reduction in BER activity in inhibited cells. Unexpectedly, the damage pattern assessed by IF imaging of the base lesions (figure 3.1) and OGG1 signal after $KBrO_3$ treatment (figure 3.5) differs greatly. While the 8-OxoG signal is evenly distributed throughout the whole nucleus, OGG1, besides the punctate background signal, accumulates foremost at γH2AX clusters. This behavior of the OGG1 staining was observed after $KBrO_3$ treatment as well as after heavy ion exposure. In the case of an ion traversal, OGG1 can be found very pronounced along the track as well as at off-track γH2AX foci. The reason why OGG1 accumulates at DSBs is not quite obvious. While this finding may be attributed to some degree of uncertainty of the OGG1 antibody binding, OGG1 foci co-localizing with DSB-marker were observed as well in the literature after high-LET exposure [138] and at sites of laser-induced damage [207]. Additionally, other groups also observed the punctate nuclear background signal of OGG1 [208], which supports to some degree the validity of the OGG1 staining presented in this work. Whilst the OGG1 signal accumulates very pronounced along the ion trajectory of Fe- and Li-ion irradiated cells (figure 3.9), the effect of BER inhibition on the OGG1 foci count per track length varies greatly and is in general less strong than the difference observed off-track. The fact that OGG1 recruitment can still be observed within tracks even during the BER inhibition may be explained by the inhibitor combination not preventing the formation of OGG1 foci completely. Highly clustered base lesions inside the track might lead to the accumulation of large amounts of OGG1 and the inhibitor combination used in this work clearly does not prevent OGG1-binding entirely. Hence, OGG1 signal would still be observable at ion-tracks in OGG1-impaired cells, even though the foci may consist of less molecules.

Furthermore, the OGG1 data in- and off-track after Fe- and Li-ion irradiation suggests that the signal of the glycosylase OGG1 increases during DSB repair time and is highest 1 h after irradiation. A previous study found that another DNA glycosylase, NEIL1, is being removed from the DSB site in the time course of 15 to 30 min after the exposure to IR while it returns back around 1 h after irradiation [209]. The reason for the absence of NEIL1 during this time is the binding of Ku to the DSB ends, which is supposed to prevent the activity of NEIL1 at neighboring base lesions until the DSB is resolved [209]. Ku and DNA-PK are assumed to bind less efficiently to short DNA fragments induced by high-LET irradiation [105, 210]. However, Ku is supposed to bind to almost all DSBs [211] and DNA-PK signal can be observed in Fe-ion tracks [212]. It remains unclear if the initial binding of Ku to complex DSB ends in ion tracks effectively inhibits the further recruitment of BER factors. PARP1, which is involved in the repair of SSBs [213], competes with Ku at DSB sites and high concentrations of PARP1 may inhibit Ku recruitment [101]. Although the role of PARP1 in BER is not well understood [63] it was found to directly interact with XRCC1 [214] and OGG1 during BER [215], while OGG1 is assumed to stimulate the activation of PARP1 upon the induction of oxidative damage [215, 216]. Importantly, PARP1 is known to be involved in error-prone a-EJ pathways [101]. It can thus be hypothesized that base clusters at complex DSBs in ion tracks are processed more frequently via BER due to less effective Ku-binding. If PARP1 is being recruited to the BER complex, it may prevent the accumulation of additional Ku molecules, increasing the probability of the processing of complex in-track DSBs as well as BER-induced DSBs via alternative pathways [209].

Overall, the experimental setup might not be sensitive enough to detect those changes, including the number of DSBs in ion tracks. Although the treatment with BER inhibitors prior and during $KBrO_3$ incubation prevents the formation of DSBs significantly (figure 3.6), there was a huge difference observable regarding BER inhibitor treatment between in- and off-track RIF after Fe- and Li-ion irradiation. 15 min after Fe-ion irradiation, BER-inhibited cells demonstrate a decrease in off-track γH2AX foci of around 62% (figure 3.11). The reduction observed during 45 min of live-cell imaging of U2OS cells tagged with NBS1-GFP after Fe-ion irradiation was around 59% for off-track NBS1 foci (figure 3.13), which is in line with the γH2AX data, but slightly more than a reduction of 43% obtained from similar experiments with the same cell line irradiated with X-rays [74]. In-track γH2AX foci on the other hand show a far less pronounced decrease of 13% 15 min after Fe-ion irradiation in BER-inhibited cells. However, this apparent lack of BER inhibition in ion tracks could be explained by the high damage density within the track region. Due to the higher LET, Fe ions induce an increased number of DSBs and thus more RIF along the ion trajectory, in contrast to Li ions with a lower LET. With increasing LET values, the amount of observable RIF will reach a certain limit. Below this LET threshold of 200 keV/µm to 300 keV/µm, a dependence of track structure and LET may still be observable [146, 217], as demonstrated by other groups in cells exposed to Fe- and Si-ions [217]. However, at high-LET values in-track RIF may become more difficult to distinguish due to the increased clustering of DSBs and overlapping foci. Regarding the optical resolution limit of the microscope and the mean focus diameter, especially for damage markers with a broad extension around the DSB such as the mega-base wide phosphorylation of H2AX histones [142], the number of DSBs along ion tracks will be underestimated. For instance, the DSB marker NBS1 used for the live cell experiments accumulates at DSB sites to foci of much smaller size than the other two frequently used DSB marker γH2AX and 53BP1. Presumably due to the small NBS1 foci size, the difference observed between the number of foci per track length in inhibited and non-inhibited cells was the highest of all the experiments performed. Nonetheless, to improve the γH2AX foci detection in tracks, cells were exposed to lower LET Li ions. Although there are in general less γH2AX foci per track length observable after Li-ion irradiation as compared to Fe ions, the BER inhibitor effect on the in-track foci number is no more pronounced than what was observed in Fe-ion tracks. Hence, this experimental setup may not be sensitive enough to reliably detect changes in the amount of DSBs in heavy-ion tracks. Future experiments could elucidate further on this finding by employing more advanced high-resolution microscope techniques and extensive pre-extraction [218–220]. Additionally, emerging techniques like expansion microscopy, which relies on the physical isotropic expansion of the specimen, could potentially enlarge the track area [221, 222]. However, difficulties may occur at the evaluation step due to the nano-foci structure of DSB marker with increased resolution [223–227], since this substructure cannot be correlated reliably to the actual DSB number.

With increased numbers of DSBs inside the ion trajectory due to BER, neighbouring DSBs may become more clustered and difficult to repair. Importantly, DNA break ends within complex DSBs will be resected more often [197]. While DNA end-resection is required as a preliminary step for performing HR in S- and G2-phase cells [120, 228] it can be observed as well in G1-phase cells at high-complex damage lesions [131], for instance after heavy-ion irradiation. Since G1-phase cells cannot repair DSBs within an error-free pathway, complex damage induced by high-LET irradiation may lead to an accumulation of mutations due to mis-repair [79, 138, 229]. While almost no complex chromosomal aberrations were observed after photon irradiation [162, 169], these mutagenic exchanges were found in more than 20% of cells surviving the irradiation with Fe ions [162]. In line with the *in vitro* data, lymphocytes derived from astronauts after exposure to the space environment for prolonged time have shown increased frequencies in the occurrence of chromosomal aberrations, with complex exchanges being more prevalent than simple chromosome lesions [230].

Supporting the notion of the increased DSB clustering within ion tracks due to BER processes, higher frequencies of the HR-marker RAD51 at in-track DSBs in non-inhibited cells were observed (figure 3.20). The increase of RAD51 foci at in-track RIF could thus reflect the increase of DSB clustering. Multiple RPA foci for instance were also observed in α-particle irradiation induced DSB clusters [130] as well as after C-ion irradiation [201]. The frequency of RAD51 co-localization at off-track DSBs on the other hand does not differ between inhibited and non-inhibited cells. Since BER leads to dispersed DSBs it would not be expected to observe increased DSB clustering outside the track region.

The biological processing of base lesions induced by ionizing radiation, which may itself lead to an increased damage load, is not only important for the risk assessment of heavy-ion irradiation in space but could also serve as input for radiobiological modeling of DNA damage induction and repair [231–233], reviewed in Baiocco et al. [234].

4.2 Higher break-end resection frequency and increased use of homologous recombination after Fe-ion irradiation

In line with other studies showing an LET-dependence of the amount of RPA foci at DSB sites, which are supposed to reflect the increase of clustering [130, 201], strongly clustered in-track DSBs co-localized more frequently with RPA after Fe-ion irradiation than less clustered off-track or X-ray induced DSBs (figure 3.16). This supports the observation that repair pathway choice depends on the degree of damage complexity [83]. Nonetheless, the increased frequency of resection-use at sparsely dispersed DSBs around the ion trajectory in comparison to cells after X-ray irradiation (figure 3.16), could indicate that besides damage quality alone, chromatin condensation and thereby accessibility to the damage site seems to influence pathway choice as well [86]. The complexity of DSBs induced by δ-electrons emerging from heavy-ion interactions is assumed to be almost identical to DSBs induced by photon irradiation [28, 74, 198]. Thus, it could be hypothesized that the concurrent high complex track damage may impact the DDR nuclear wide. However, the analysis of not directly hit nuclei did not reveal significant differences between the resection use at off-track DSBs and X-ray irradiation induced DSBs due to the small sample size. With a fluence of around 3×10^6 particles/cm^2, most of the nuclei have been hit by one or two ions (appendix 4.5). Repeating this experiment while using a lower fluence might clarify whether the prevalence of complex track damage may shift the DDR at lower complex DSBs towards resection.

The ratio of resected DSBs is more or less reflected in the number of RAD51-DSB events observed in- and off-track (figure 3.18), suggesting that most of the resected DNA ends will be further processed via HR. Although it cannot be certainly excluded that some of the resected off- and in-track DSBs will be repaired by error-prone alternative mechanisms, especially in G1 cells. Usually NHEJ is the main DSB repair pathway after low-LET irradiation in human cells, even if the cell enters the G2 phase and would be able to perform HR due to the presence of sister chromatids [83, 84]. Yet after high-LET irradiation, for instance after Fe-ion irradiation, cells enhance their use of HR [235], as well as resection after C-ion irradiation with almost all DSBs accompanied by RPA in G2 [83] and importantly also a substantial fraction in G1 cells [131]. In contrast to high-LET irradiation only 20% to 25% or 15% to 20% of X-ray induced DSBs are being resected or processed via HR, respectively, in G2 cells [86], similar to the data presented in section 3.3.1 and 3.3.2. However, HR-independent resection in G1 cells via error-prone MMEJ is less pronounced than the extended resection during HR and may not always be observable via RPA foci analysis, especially for lower complex off-track and photon-induced DSBs [236].

Previous experiments in confluent fibroblast cultures show similar frequencies of resection and HR use at off-track DSBs as for X-ray induced DSBs (data not shown) in contrast to the higher frequency observed in the G1/G2-phase U2OS cell population. Different cell lines may differ in their use of resection and HR [237] and cancer cells may resect DNA break ends more often than normal fibroblasts. For instance, variation in chromatin condensation between cancer cells and fibroblasts may lead to a difference in frequency of resection used at DSBs [238].

Results obtained by irradiation of a mixed cell cycle population of U2OS cells with isolated or mixed beams of α-particles and γ-rays suggest a slower repair for small foci if both radiation qualities are administered simultaneously [239, 240]. Although the radiation geometry in this publication prevents the direct correlation of focus location and radiation quality, photons seem to induce smaller 53BP1 foci compared to α-particles [239]. Besides 53BP1, this focus size difference after high-LET irradiation perpendicular to the cell monolayer was also observed for the DSB marker γH2AX, which tends to be larger due to the occurrence of several DSBs along the track [241, 242]. While assuming a similar cell cycle distribution of U2OS cells, this mixed beams study supports the observation of increased resection and HR use at off-track foci after heavy-ion irradiation by showing a slower processing of small foci. Resection-dependent pathways like HR as well as a-EJ are both considered to be responsible for the slow part of DSB repair kinetics [97].

Although 53BP1 is supposed to inhibit resection at break ends [124], it can be used as a general DSB marker since 53BP1-RIF co-localize with γH2AX foci (appendix 4.4) up to several hours after photon-irradiation with almost identical repair kinetics [193]. Furthermore, 53BP1 signal has been observed at DSBs determined for repair by HR [243]. Confocal microscope images also show the co-localization of 53BP1 with RPA foci, for instance after laser or high-LET irradiation [160, 244, 245]. Observing the concurrent recruitment of 53BP1 and the HR marker RAD51 via high resolution microscopy, the regions of RAD51 and 53BP1 signal do not overlap and RAD51 accumulates foremost inside the surrounding 53BP1 intensity [246]. Nonetheless, due to the resolution limit, both signals show an overlap in confocal microscope images.

Follow-up experiments should in particular focus on the cell cycle distribution to assess the extend of resection at simple off-track DSBs in G1-phase cells. Resected break ends cannot be ligated via NHEJ [83] and thus require either alternative repair in G1 phase or HR in S and G2 phase. Resected DSBs induced in G1 cells may even remain unrepaired until the cell enters S phase enabling the further processing by HR [193]. For instance, unrepaired RAD51-positive DSBs in G2 phase were found to progress into G1 phase [193]. Alternative repair as well as the proceeding of the cell cycle with remaining DSBs are both highly error-prone processes and future work should elucidate on the likelihood of those events after high-LET irradiation as well as the cellular consequences.

4.3 Accelerated repair kinetics for Fe-ion induced off-track DSBs

Surprisingly, repair kinetics of δ-electron induced off-track DSBs in G1 cells after Fe-ion irradiation are slightly faster compared to DSB repair after X-ray irradiation (figure 3.24). Complex in-track DSBs on the other hand are partially even observable more than 10 h after irradiation (data not shown), indicating that they are more difficult to repair while some in-track DSBs may even pose non-repairable [161]. Since off-track DSBs appear to be processed with fast kinetics in mainly G1-phase cells (figure 3.22), resection-dependent repair can almost be completely excluded to be relevant for repair at δ-electron induced DSBs, at least in normal fibroblasts. Confluent human primary fibroblasts in G0/G1 for instance were observed to show almost no resection activity after heavy-ion irradiation, indicating a cell line specific resection activity [197]. Nonetheless, the apparent lack of resection at off-track DSBs in G1 cells emphasizes the great similarity in complexity between off-track DSBs and DSBs induced by photon irradiation. Although the difference between the kinetics of X-ray and off-track DSB repair is quite small, it could hint towards a more enhanced DDR through concurrent high-complex track damage in the same nucleus. Research on δ-electron damage due to heavy-ion irradiation is quite scarce, but looking at the data of Nakajima et al. [198], δ-electron induced DSBs after Fe-ion irradiation seem to be repaired somewhat faster in contrast to their X-ray data. Importantly, Nakajima et al. [198] used confluent human fibroblasts primarily in G0/G1 phase to assess the repair after Fe-ion irradiation.

Although cells without tracks but with δ-electron contribution have been evaluated as well (figure 3.24c), the outcome was ambiguous. Strong fluctuations of the DSB number's mean especially within the early time points up to 2 h impair the comparison with the X-ray curve. An inhomogeneous distribution of δ-electron track ends between individual ion tracks could be assumed to be the reason for these fluctuations. However, Monte Carlo simulations performed with high energetic (270 MeV/n) uranium (U) ion beams showed an almost evenly dispersed background of δ-electron induced DSBs between the ion-tracks [247]. While these simulations were performed with particle fluences of around 6×10^6 particles/cm^2, the discussed experiment was carried out with just half of it (3×10^6 particles/cm^2). Thus, inhomogeneities of the δ-electron distribution could be in fact responsible for the fluctuation of off-track DSBs observed in non-hit cells. Nonetheless, the standard deviation of the DSB number in non-hit cells is within the same magnitude as for cells traversed by Fe ions, suggesting rather small variations between cells and little influence of distance to the ion tracks. Since the number of non-hit cells evaluated is around half as much as for cells hit by Fe ions and the whole experiment was repeated just once, additional data from at least another independent set would be required to draw any conclusions.

The presented repair kinetics suggest that the large majority of off-track DSBs in G1 cells are ligated via the fast NHEJ. Although a slight decrease in the time required for DSB resolving was observed for the off-track DSBs in contrast to X-ray irradiation induced DSBs, there is currently no plausible explanation for the exact mechanism behind this acceleration of repair. Since G1-phase cells irradiated solely with low-LET X-rays do not show any significant resection signal via RPA accumulation at DSBs [131], the hypothesis of a resection-caused slower DSB-repair in a minor fraction of the X-ray γH2AX assay presented in this work is unlikely. Whilst the electron's kinetic energy spectrum presumably differs between X-ray and Fe-ion irradiation, the large majority of simple damage clusters will be induced solely by the slow electron part, the electron track ends. Nonetheless, it could be of interest to determine the fraction of low-energetic electrons which contribute to the DSB load within the same nucleus. More low-energetic electrons thus results in more electron track ends which consequently increase the probability of the induction of DSB clusters.

DNA damage repair kinetics are also affected by the level of chromatin condensation. Less dense euchromatin for instance allows for faster DSB end joining than the more compact heterochromatin region, presumably due to a variation in accessibility of repair factors to the DNA strand [151]. It can thus be speculated whether chromatin decondensation is more extended after heavy-ion exposure including the area around off-track DSBs. Mixed beam experiments with the simultaneous irradiation of γ-rays and alpha-particles and subsequent evaluation using transmission electron microscopy (TEM) show an inverse correlation of electron density and damage cluster size, indicating that smaller foci are surrounded by less dense chromatin and thus easier to access for repair factors [220]. Especially after mixed beams, the brightness around clusters of small bead numbers seems higher as compared to photons only. This would support the finding of increased rejoining efficiency at off-track DSBs due to an enhanced accessibility as well as higher frequencies of resection and HR use in S and G2 cells since histone acetylation, which leads to the relaxation of the chromatin, is supposed to promote HR [248]. Nonetheless, the method utilized in this study of Akuwudike et al. [220] involves the use of uranyl acetate to measure the electron density via TEM, and uranyl acetate is supposed to bind non-specifically to nuclear components, for instance RNA. Thus, areas of low density (increased brightness) within and around RIF are diminished of RNA, while the structure of chromatin inside RIF resembles non-irradiated euchromatin [249].

Moreover, it was shown that the irradiation of normal human fibroblasts with low and high X-ray doses does not alter the expression of NHEJ proteins 0 to 5 h after irradiation significantly [250], although there is no similar data in the case of high-LET irradiation. Compared to photon irradiation, the exposure to charged particles leads to stronger effects on changes in general gene expression [251, 252] with dependence on LET [253]. While there may be some changes in repair gene expression induced by charged particle traversals, fast chromatin modifications are probably more relevant. Pan-nuclear γH2AX signal for instance was shown to be induced shortly after heavy-ion irradiation through ATM and DNA-PK activity, while it was not observed after irradiation with 1 Gy X-rays, indicating a dependence on dose [147]. Thus, ion-induced complex DNA damage seems to trigger fast nuclear-wide chromatin modifications [147]. Upon local DSB induction via laser irradiation, a pan-nuclear distribution of phosphorylated KRAB-associated protein 1 (KAP-1) can be observed [254]. The ATM-dependent phosphorylation of KAP-1 is assumed to be involved in chromatin decondensation processes to increase accessibility to sites of DSBs [254, 255]. Interestingly, cells with partial loss of the linker histone H1, which is correlated with less chromatin condensation [256], show an enhanced DDR with slightly faster repair kinetics after the exposure to IR compared to wild-type cells [257]. Whether nuclear-wide chromatin modifications induced by ion traversals contribute to the facilitated DDR observed for off-track DSBs in mostly G1-phase fibroblasts needs to be further explored.

4.4 Conclusion and outlook

This work particularly emphasizes the different damage qualities a cell experiences after being exposed to heavy ions. High-energetic Fe ions relevant for space radiation research inflict strongly clustered DSBs along their trajectory while δ-electrons induce additional sparsely distributed DSBs around the ion track. The maximum δ-electron range can reach up to the mm-scale [28] and thus adds to the dose contribution in adjacent cells not initially hit by the ion. It was estimated for one cell hit by 600 MeV/n Fe ions, more than 30 surrounding cells will be exposed to δ-electrons solely [258]. This mixed radiation quality property of HZE ions is unique, as for instance the exposure to alpha particles emitted from radioactive sources does not deposit dose on non-hit cells. In cells hit by Fe ions, the clustered track damage seems to impact the DDR overall, with implications on the processing of δ-electron induced off-track DSBs. While an increased use of resection and HR was observed at off-track DSBs in G1/G2-phase cancer cells, the same type of lesion was repaired faster in mainly G1-phase normal fibroblasts. Although both observations are quite contradictory, one could attempt to explain this finding with an increased accessibility for off-track DSBs in cells with concurrent high damage loads. Furthermore, the data suggests that simple off-track DSBs in confluent fibroblasts are presumably not processed via alternative repair pathways. Contrarily, in-track DSBs within the same cell line remain for several hours, indicating an extended need for break-end processing [83]. Since high resection rates were observed in G1 cells after the exposure to heavy ions [131] it can be assumed that foremost clustered track damage may be processed via resection-dependent alternative repair in G1 cells which are unable to perform HR. Additionally, it may even be possible that unresolved but resected DSBs transition from G1 into S and G2 phase to enable repair via factors involved mainly in HR [85, 193]. Due to the missing DNA template in both scenarios, the repair outcome may be highly error-prone. Although in G1/G2 cells almost the same fraction of off-track DSBs shows resection and HR signal, whether alternative mechanisms are involved at off-track DSB-repair in G2-phase cells remains unresolved. Additionally, the assessment of not directly hit cells exposed to δ-electrons would be of great interest to determine the impact of clustered track damage on the processing of off-track DSBs. Due to the BER activity in close proximity to in-track DSBs, additional BER-induced DSBs are assumed to increase the damage clustering within ion tracks even further. Although the data suggests that the increase of observed in-track DSBs is accompanied by an increase of HR signal, it is not clear yet whether the presumable increase of damage clustering leads to a more pronounced impact on the overall DDR. Since the assessed fibroblasts show HR signal, they need to be in S or G2 phase. Nonetheless, off-track DSBs do not differ in their use of HR between fibroblasts with more (non-inhibited) or less (BER inhibited) in-track damage clustering. Future experiments may elaborate more on the correlation of the amount and degree of damage clustering and the impact on the nuclear-wide DDR at distant off-track DSBs, possibly also in different cell lines and precisely estimated cell cycle phases.

In conclusion, the hereby presented data suggests that the exposure to space relevant HZE ions impacts the nuclear-wide DDR, while BER processes increase the overall DSB load and supposedly add to the damage clustering within the narrow ion-track area. Importantly, IR induced damage clusters correlate strongly with genomic instability [106] and processes like BER which add to the clustering may increase the risk of cancer. Regarding future deep space missions, the exposure to HZE ions, despite shielding, is not negligible. During missions extending the duration of several years, the probability of multiple ion hits in long living cells increases [10], while each nuclear ion traversal induces clustered damage which is difficult to repair [160, 197]. Last but not least, ground-based radiobiological experiments studying the underlying molecular mechanisms are indispensable to reduce the uncertainties related to cancer risk from exposure to space radiation [259].

Appendix

4.1 OGG1 IF signal accumulates inside nucleoli

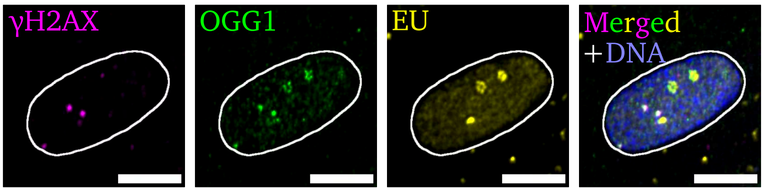

Figure 4.1: **Accumulation of OGG1 signal inside nucleoli.** IF images of AG1522D fibroblasts + BERi and after $KBrO_3$ treatment stained against the DSB marker γH2AX (magenta), BER marker OGG1 (green), RNA marker EU (yellow) and DNA (blue). Since nucleoli contain transcriptionally active ribosomal DNA (rDNA), nascent RNA can be detected via a click iT reaction with incorporated EU. OGG1 signal seems to accumulate inside nucleoli in AG1522D fibroblasts +/−BERi and can be observed in $KBrO_3$ treated as well as in non-treated cells. Scale bar: 10 μm

4.2 Comparison of γH2AX and 53BP1 foci after $KBrO_3$ treatment

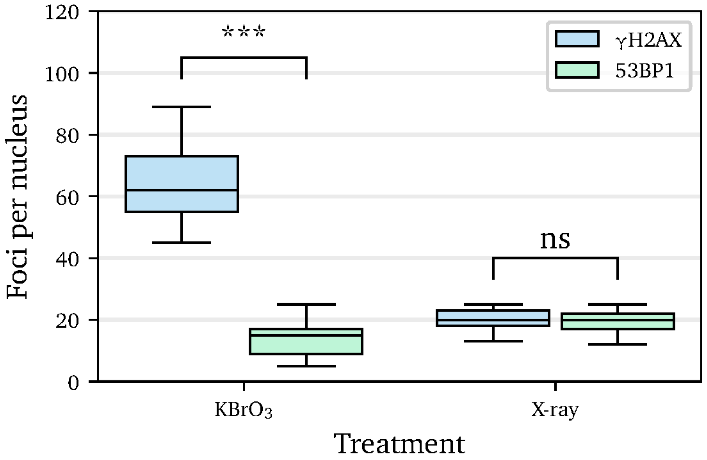

Figure 4.2: **Different number of 53BP1 foci after $KBrO_3$ treatment.** γH2AX and 53BP1 foci numbers in AG1522D fibroblasts were assessed directly after $KBrO_3$ treatment or 1 h after 0.5 Gy X-ray irradiation. Statistical analysis via Mann-Whitney *U* test: $KBrO_3$: $p=1.4 \times 10^{-9}$ and X-ray: $p=0.57$. With N=1 experiment including n=25 cells per treatment.

4.3 Comparison of DSB repair kinetics between $KBrO_3$ treated and X-ray irradiated cells

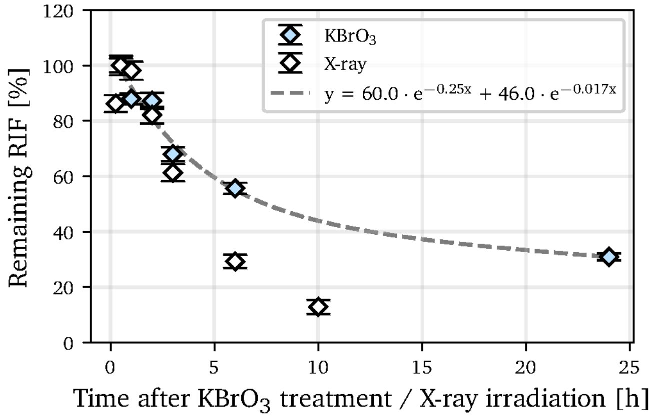

Figure 4.3: **Comparison of repair kinetics of cells treated with $KBrO_3$ or irradiated with X-rays.** Comparison of the remaining amount of γH2AX RIF after treatment with $KBrO_3$ or after irradiation with 0.5 Gy X-rays in AG1522D fibroblasts. X-ray data was obtained from 3.24b. $KBrO_3$ data was fitted biexponentially. With N=3 independent experiments including $n_{KBrO_3,Control}$=1035, $n_{KBrO_3,BERi}$=960 and $n_{X\text{-}ray}$=522 cells.

4.4 Comparison of 53BP1 and γH2AX foci number

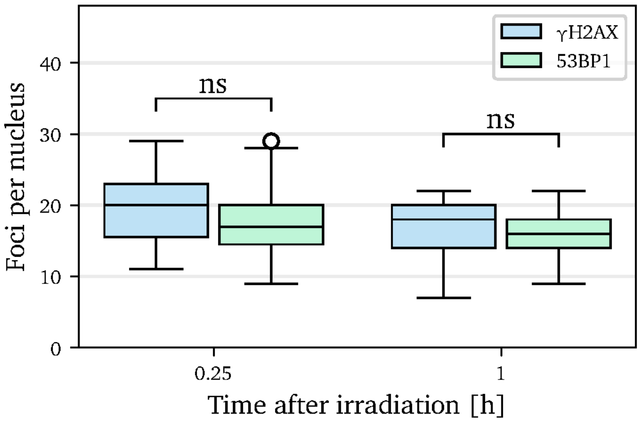

Figure 4.4: **Similar 53BP1 and γH2AX foci numbers after X-ray irradiation.** Mean number of 53BP1 and γH2AX foci in AG1522D fibroblasts 15 min and 1 h after 0.5 Gy X-ray irradiation. Statistical analysis via Mann-Whitney *U* test: 0.25 h: p=0.080 and 1 h: p=0.15. With N=1 experiment including $n_{0.25h}$=31 and n_{1h}=25 cells.

4.5 Poisson distribution

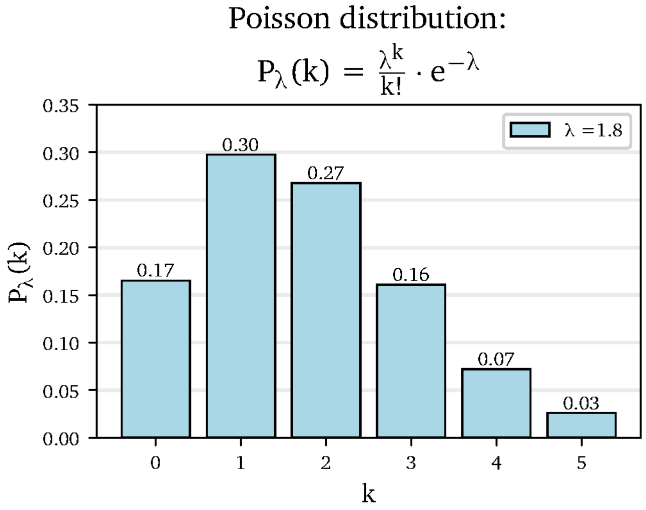

Figure 4.5: **Poisson distribution of nuclei hits with Fe ions.** Poisson distribution of the probability ($P_\lambda(k)$) of the number of nuclear ion traversals (k) with λ=1.8, estimated by assuming a fluence of 3×10^6 particles/cm^2 and a mean U2OS nucleus area of 6×10^{-7} cm^2 (60 µm^2), as the vertical plane through the nucleus orthogonal to the direction of irradiation.

Contributions

The experiment behind the data presented in section 3.3.3 was performed by Prof. Dr. Burkhard Jakob, including sample preparation, Fe-ion irradiation and image acquisition.

References

[1] E. Romero and D. Francisco. “The NASA Human System Risk Mitigation Process for Space Exploration”. In: *Acta Astronautica* 175 (Oct. 2020), pp. 606–615.

[2] E. Seedhouse. “Countermeasures”. In: *Life Support Systems for Humans in Space*. Ed. by E. Seedhouse. Cham: Springer International Publishing, 2020, pp. 199–242.

[3] S. Zhang et al. “First Measurements of the Radiation Dose on the Lunar Surface”. In: *Science Advances* 6.39 (Sept. 2020), eaaz1334.

[4] N. A. Vernice et al. “Long-Term Spaceflight and the Cardiovascular System”. In: *Precision Clinical Medicine* 3.4 (June 2020), pp. 284–291.

[5] F. A. Cucinotta et al. “Space Radiation Risks to the Central Nervous System”. In: *Life Sciences in Space Research* 2 (July 2014), pp. 54–69.

[6] F. A. Cucinotta et al. “Space Radiation and Cataracts in Astronauts”. In: *Radiation Research* 156.5 (Nov. 2001), pp. 460–466.

[7] F. A. Cucinotta and M. Durante. “Cancer Risk from Exposure to Galactic Cosmic Rays: Implications for Space Exploration by Human Beings”. In: *The Lancet Oncology* 7.5 (May 2006), pp. 431–435.

[8] M. M. Shapiro, ed. *Composition and Origin of Cosmic Rays*. Dordrecht: Springer Netherlands, 1983.

[9] F. Cucinotta and M. Durante. “Risk of Radiation Carcinogenesis”. In: *Human health and performance risks of space exploration missions. NASA SP-2009-3405. Houston: National Aeronautics and Space Administration* (2009), pp. 119–170.

[10] S. B. Curtis and J. R. Letaw. “Galactic Cosmic Rays and Cell-Hit Frequencies Outside the Magnetosphere”. In: *Advances in Space Research* 9.10 (Jan. 1989), pp. 293–298.

[11] J. W. Wilson et al. “Issues in Space Radiation Protection: Galactic Cosmic Rays”. In: *Health Physics* 68.1 (Jan. 1995), pp. 50–58.

[12] L. Heilbronn et al. “Overview of Secondary Neutron Production Relevant to Shielding in Space”. In: *Radiation Protection Dosimetry* 116.1-4 (Dec. 2005), pp. 140–143.

[13] D. A. Pierce et al. “Studies of the Mortality of Atomic Bomb Survivors. Report 12, Part I. Cancer: 1950-1990”. In: *Radiation Research* 146.1 (1996), pp. 1–27.

[14] F. A. Cucinotta et al. “Space Radiation Cancer Risks and Uncertainties for Mars Missions”. In: *Radiation Research* 156.5 (Nov. 2001), pp. 682–688.

[15] W. Tinganelli and M. Durante. “Carbon Ion Radiobiology”. In: *Cancers* 12.10 (Oct. 2020), p. 3022.

[16] F. Tommasino, E. Scifoni, and M. Durante. “New Ions for Therapy”. In: *International Journal of Particle Therapy* 2.3 (Dec. 2015), pp. 428–438.

[17] M. Durante and K. Parodi. “Radioactive Beams in Particle Therapy: Past, Present, and Future”. In: *Frontiers in Physics* 8 (Aug. 2020).

[18] H. M. Prichard and T. F. Gesell. “Radon in the Environment”. In: *Advances in Radiation Biology*. Ed. by J. T. Lett. Vol. 11. Advances in Radiation Biology. Elsevier, Jan. 1984, pp. 391–428.

[19] S. Darby et al. “Radon in Homes and Risk of Lung Cancer: Collaborative Analysis of Individual Data from 13 European Case-Control Studies”. In: *BMJ* 330.7485 (Jan. 2005), p. 223.

[20] D. T. Goodhead. “Mechanislns for the Biological Effectiveness of High-LET Radiations.” In: *Journal of Radiation Research* 40.Suppl. (1999), pp. 1–13.

[21] M. Durante et al. “X-Rays vs. Carbon-Ion Tumor Therapy: Cytogenetic Damage in Lymphocytes”. In: *International Journal of Radiation Oncology*Biology*Physics* 47.3 (June 2000), pp. 793–798.

[22] D. Schardt, T. Elsässer, and D. Schulz-Ertner. “Heavy-Ion Tumor Therapy: Physical and Radiobiological Benefits”. In: *Reviews of Modern Physics* 82.1 (Feb. 2010), pp. 383–425.

[23] H. Bethe. “Zur Theorie Des Durchgangs Schneller Korpuskularstrahlen Durch Materie”. In: *Annalen der Physik* 397.3 (1930), pp. 325–400.

[24] E. L. Alpen et al. “Tumorigenic Potential of High-Z, High-LET Charged-Particle Radiations”. In: *Radiation Research* 136.3 (1993), pp. 382–391.

[25] T. C.-h. Yang et al. “Neoplastic Cell Transformation by Heavy Charged Particles”. In: *Radiation Research* 104.2 (1985), S177–S187.

[26] F. A. Cucinotta, H. Nikjoo, and D. T. Goodhead. “The Effects of Delta Rays on the Number of Particle-Track Traversals per Cell in Laboratory and Space Exposures”. In: *Radiation Research* 150.1 (July 1998), p. 115.

[27] W. E. Wilson and T. L. Criswell. “Microscopic Track Structure of Equal-Let Heavy Ions”. In: *Advances in Space Research* 6.11 (Jan. 1986), pp. 75–81.

[28] F. A. Cucinotta, H. Nikjoo, and D. T. Goodhead. “Model for Radial Dependence of Frequency Distributions for Energy Imparted in Nanometer Volumes from HZE Particles”. In: *Radiation Research* 153.4 (Apr. 2000), pp. 459–468.

[29] F. A. Cucinotta et al. “Radial Dose Model of Ssb, Dsb, Deletions and Comparisons to Montecarlo Track Structure Simulations”. In: *Robert Katz Publications* (Jan. 1997).

[30] C. Fournier et al. “The Fate of a Normal Human Cell Traversed by a Single Charged Particle”. In: *Scientific Reports* 2.1 (Dec. 2012), p. 643.

[31] J. Ward. “The Complexity of DNA Damage: Relevance to Biological Consequences”. In: *International Journal of Radiation Biology* 66.5 (Jan. 1994), pp. 427–432.

[32] R. Roots and S. Okada. “Estimation of Life Times and Diffusion Distances of Radicals Involved in X-Ray-Induced DNA Strand Breaks or Killing of Mammalian Cells”. In: *Radiation Research* 64.2 (Nov. 1975), pp. 306–320.

[33] G. Scholes, J. F. Ward, and J. Weiss. “Mechanism of the Radiation-Induced Degradation of Nucleic Acids”. In: *Journal of Molecular Biology* 2.6 (Dec. 1960), pp. 379–391.

[34] G. Scholes, J. F. Ward, and J. J. Weiss. “Some Chemical Effects of Ionizing Radiations on Nucleic Acids and Related Compounds”. In: *Journal of Polymer Science* 48.150 (1960), pp. 301–308.

[35] J. Cadet, T. Douki, and J.-L. Ravanat. “Oxidatively Generated Base Damage to Cellular DNA”. In: *Free Radical Biology and Medicine* 49.1 (July 2010), pp. 9–21.

[36] Y. Luo et al. “Three Chemically Distinct Types of Oxidants Formed by Iron-Mediated Fenton Reactions in the Presence of DNA.” In: *Proceedings of the National Academy of Sciences* 91.26 (Dec. 1994), pp. 12438–12442.

[37] A. Meister and M. E. Anderson. “Glutathione”. In: *Annual Review of Biochemistry* 52.Volume 52, 1983 (July 1983), pp. 711–760.

[38] E. Gajewski et al. “Modification of DNA Bases in Mammalian Chromatin by Radiation-Generated Free Radicals”. In: *Biochemistry* 29.34 (Aug. 1990), pp. 7876–7882.

[39] J. F. Ward. “DNA Damage Produced by Ionizing Radiation in Mammalian Cells: Identities, Mechanisms of Formation, and Reparability”. In: *Progress in Nucleic Acid Research and Molecular Biology*. Ed. by W. E. Cohn and K. Moldave. Vol. 35. Academic Press, Jan. 1988, pp. 95–125.

[40] H. Nikjoo et al. “Computational Approach for Determining the Spectrum of DNA Damage Induced by Ionizing Radiation”. In: *Radiation Research* 156.5 (Nov. 2001), pp. 577–583.

[41] K. M. Prise et al. “A Review of Dsb Induction Data for Varying Quality Radiations”. In: *International Journal of Radiation Biology* 74.2 (Jan. 1998), pp. 173–184.

[42] D. Charlton, H. Nikjoo, and J. Humm. “Calculation of Initial Yields of Single- and Double-strand Breaks in Cell Nuclei from Electrons, Protons and Alpha Particles”. In: *International Journal of Radiation Biology* 56.1 (Jan. 1989), pp. 1–19.

[43] H. Nikjoo et al. “Modelling of Radiation-induced DNA Damage: The Early Physical and Chemical Event”. In: *International Journal of Radiation Biology* 66.5 (Jan. 1994), pp. 453–457.

[44] K. Rothkamm et al. “Pathways of DNA Double-Strand Break Repair during the Mammalian Cell Cycle”. In: *Molecular and Cellular Biology* 23.16 (Aug. 2003), pp. 5706–5715.

[45] H. Nikjoo et al. “Computational Modelling of Low Energy Electron-Induced DNA Damage by Early Physical and Chemical Event”. In: *International journal of radiation biology* 71 (June 1997), pp. 467–83.

[46] S. A. Lesko, R. J. Lorentzen, and P. O. P. Ts’o. “Role of Superoxide in Deoxyribonucleic Acid Strand Scission”. In: *Biochemistry* 19.13 (June 1980), pp. 3023–3028.

[47] W. F. Blakely et al. “Hydrogen Peroxide-Induced Base Damage in Deoxyribonucleic Acid”. In: *Radiation Research* 121.3 (Mar. 1990), pp. 338–343.

[48] J. Dahm-Daphi, C. Sass, and W. Alberti. “Comparison of Biological Effects of DNA Damage Induced by Ionizing Radiation and Hydrogen Peroxide in CHO Cells”. In: *International Journal of Radiation Biology* 76.1 (Jan. 2000), pp. 67–75.

[49] D. Brenner and J. Ward. “Constraints on Energy Deposition and Target Size of Multiply Damaged Sites Associated with DNA Double-strand Breaks”. In: *International Journal of Radiation Biology* 61.6 (Jan. 1992), pp. 737–748.

[50] H. Nikjoo et al. “Modelling of DNA Damage Induced by Energetic Electrons (100 eV to 100 keV)”. In: *Radiation Protection Dosimetry* 99.1-4 (June 2002), pp. 77–80.

[51] M. Hada and A. G. Georgakilas. “Formation of Clustered DNA Damage after High-LET Irradiation: A Review”. In: *Journal of Radiation Research* 49.3 (May 2008), pp. 203–210.

[52] J. A. Nickoloff, N. Sharma, and L. Taylor. “Clustered DNA Double-Strand Breaks: Biological Effects and Relevance to Cancer Radiotherapy”. In: *Genes* 11.1 (Jan. 2020), p. 99.

[53] J. M. Danforth, L. Provencher, and A. A. Goodarzi. “Chromatin and the Cellular Response to Particle Radiation-Induced Oxidative and Clustered DNA Damage”. In: *Frontiers in Cell and Developmental Biology* 10 (July 2022), p. 910440.

[54] A. Klungland et al. “Accumulation of Premutagenic DNA Lesions in Mice Defective in Removal of Oxidative Base Damage”. In: *Proceedings of the National Academy of Sciences of the United States of America* 96.23 (Nov. 1999), pp. 13300–13305.

[55] J.-P. Pouget et al. “DNA Damage Induced in Cells by γ and UVA Radiation As Measured by HPLC/GC-MS and HPLC-EC and Comet Assay”. In: *Chemical Research in Toxicology* 13.7 (July 2000), pp. 541–549.

[56] S. Steenken and S. V. Jovanovic. “How Easily Oxidizable Is DNA? One-Electron Reduction Potentials of Adenosine and Guanosine Radicals in Aqueous Solution”. In: *Journal of the American Chemical Society* 119.3 (Jan. 1997), pp. 617–618.

[57] M. Dizdaroglu. “Formation of 8-Hydroxyguanine Moiety in Deoxyribonucleic Acid on .Gamma.-Irradiation in Aqueous Solution”. In: *Biochemistry* 24.16 (July 1985), pp. 4476–4481.

[58] M. L. Wood et al. “Mechanistic Studies of Ionizing Radiation and Oxidative Mutagenesis: Genetic Effects of a Single 8-Hydroxyguanine (7-Hydro-8-Oxoguanine) Residue Inserted at a Unique Site in a Viral Genome”. In: *Biochemistry* 29.30 (July 1990), pp. 7024–7032.

[59] K. C. Cheng et al. “8-Hydroxyguanine, an Abundant Form of Oxidative DNA Damage, Causes G-T and A-C Substitutions.” In: *Journal of Biological Chemistry* 267.1 (Jan. 1992), pp. 166–172.

[60] F. L. Page et al. “Repair and Mutagenic Potency of 8-oxoG:A and 8-oxoG:C Base Pairs in Mammalian Cells”. In: *Nucleic Acids Research* 26.5 (Mar. 1998), p. 1276.

[61] A. L. Jacobs and P. Schär. “DNA Glycosylases: In DNA Repair and Beyond”. In: *Chromosoma* 121.1 (Feb. 2012), pp. 1–20.

[62] Y. Gao et al. “DNA Ligase III Is Critical for mtDNA Integrity but Not Xrcc1-mediated Nuclear DNA Repair”. In: *Nature* 471.7337 (Mar. 2011), pp. 240–244.

[63] H. E. Krokan and M. Bjoras. “Base Excision Repair”. In: *Cold Spring Harbor Perspectives in Biology* 5.4 (Apr. 2013), a012583–a012583.

[64] H. M. Nash et al. “The Critical Active-Site Amine of the Human 8-Oxoguanine DNA Glycosylase, hOgg1: Direct Identification, Ablation and Chemical Reconstitution”. In: *Chemistry & Biology* 4.9 (Sept. 1997), pp. 693–702.

[65] D. O. Zharkov et al. “Substrate Specificity and Reaction Mechanism of Murine 8-Oxoguanine-DNA Glycosylase”. In: *Journal of Biological Chemistry* 275.37 (Sept. 2000), pp. 28607–28617.

[66] M. M. Slupska et al. “Functional Expression of hMYH, a Human Homolog of the Escherichia Coli MutY Protein”. In: *Journal of Bacteriology* 181.19 (Oct. 1999), pp. 6210–6213.

[67] M. Takao et al. “A Back-up Glycosylase in Nth1 Knock-out Mice Is a Functional Nei (Endonuclease VIII) Homologue *”. In: *Journal of Biological Chemistry* 277.44 (Nov. 2002), pp. 42205–42213.

[68] B. M. F. Hanna et al. “NEIL1 and NEIL2 Are Recruited as Potential Backup for OGG1 upon OGG1 Depletion or Inhibition by TH5487”. In: *International Journal of Molecular Sciences* 22.9 (Apr. 2021), p. 4542.

[69] M.-H. David-Cordonnier, J. Laval, and P. O’Neill. “Clustered DNA Damage, Influence on Damage Excision by XRS5 Nuclear Extracts and Escherichia Coli Nth and Fpg Proteins *”. In: *Journal of Biological Chemistry* 275.16 (Apr. 2000), pp. 11865–11873.

[70] M.-H. David-Cordonnier et al. “Efficiency of Incision of an AP Site within Clustered DNA Damage by the Major Human AP Endonuclease”. In: *Biochemistry* 41.2 (Jan. 2002), pp. 634–642.

[71] J. O. Blaisdell and S. S. Wallace. “Abortive Base-Excision Repair of Radiation-Induced Clustered DNA Lesions in *Escherichia Coli*”. In: *Proceedings of the National Academy of Sciences* 98.13 (June 2001), pp. 7426–7430.

[72] N. Yang, H. Galick, and S. S. Wallace. “Attempted Base Excision Repair of Ionizing Radiation Damage in Human Lymphoblastoid Cells Produces Lethal and Mutagenic Double Strand Breaks”. In: *DNA Repair* 3.10 (Oct. 2004), pp. 1323–1334.

[73] N. Yang, M. A. Chaudhry, and S. S. Wallace. “Base Excision Repair by hNTH1 and hOGG1: A Two Edged Sword in the Processing of DNA Damage in γ-Irradiated Human Cells”. In: *DNA Repair* 5.1 (Jan. 2006), pp. 43–51.

[74] B. Jakob et al. “Differential Repair Protein Recruitment at Sites of Clustered and Isolated DNA Double-Strand Breaks Produced by High-Energy Heavy Ions”. In: *Scientific Reports* 10.1 (Jan. 2020), p. 1443.

[75] A. A. Polyzos et al. “Base Excision Repair and Double Strand Break Repair Cooperate to Modulate the Formation of Unrepaired Double Strand Breaks in Mouse Brain”. In: *Nature Communications* 15.1 (Sept. 2024), p. 7726.

[76] K. D. Mills, D. O. Ferguson, and F. W. Alt. “The Role of DNA Breaks in Genomic Instability and Tumorigenesis”. In: *Immunological Reviews* 194.1 (2003), pp. 77–95.

[77] S. Nowsheen et al. “Accumulation of Oxidatively Induced Clustered DNA Lesions in Human Tumor Tissues”. In: *Mutation research* 674.1-2 (Mar. 2009), pp. 131–136.

[78] O. A. Martin and W. M. Bonner. “γ-H2AX in Cancer Cells: A Potential Biomarker for Cancer Diagnostics, Prediction and Recurrence”. In: *Cell Cycle* 5.24 (Dec. 2006), pp. 2909–2913.

[79] S. Ritter and M. Durante. “Heavy-Ion Induced Chromosomal Aberrations: A Review”. In: *Mutation Research/Genetic Toxicology and Environmental Mutagenesis* 701.1 (Aug. 2010), pp. 38–46.

[80] J. Chen and J. Stubbe. “Bleomycins: Towards Better Therapeutics”. In: *Nature Reviews Cancer* 5.2 (Feb. 2005), pp. 102–112.

[81] M. M. Vilenchik and A. G. Knudson. “Endogenous DNA Double-Strand Breaks: Production, Fidelity of Repair, and Induction of Cancer”. In: *Proceedings of the National Academy of Sciences* 100.22 (Oct. 2003), pp. 12871–12876.

[82] M. R. Lieber. “The Mechanism of Double-Strand DNA Break Repair by the Nonhomologous DNA End-Joining Pathway”. In: *Annual Review of Biochemistry* 79.1 (June 2010), pp. 181–211.

[83] A. Shibata et al. “Factors Determining DNA Double-Strand Break Repair Pathway Choice in G2 Phase: DSB Repair Pathway Choice in G2 Phase”. In: *The EMBO Journal* 30.6 (Mar. 2011), pp. 1079–1092.

[84] O. D. Shahar et al. “Live Imaging of Induced and Controlled DNA Double-Strand Break Formation Reveals Extremely Low Repair by Homologous Recombination in Human Cells”. In: *Oncogene* 31.30 (July 2012), pp. 3495–3504.

[85] K. Karanam et al. “Quantitative Live Cell Imaging Reveals a Gradual Shift between DNA Repair Mechanisms and a Maximal Use of HR in Mid S Phase”. In: *Molecular Cell* 47.2 (July 2012), pp. 320–329.

[86] A. Beucher et al. “ATM and Artemis Promote Homologous Recombination of Radiation-Induced DNA Double-Strand Breaks in G2”. In: *The EMBO Journal* 28.21 (Nov. 2009), pp. 3413–3427.

[87] H. H. Y. Chang et al. “Different DNA End Configurations Dictate Which NHEJ Components Are Most Important for Joining Efficiency”. In: *The Journal of Biological Chemistry* 291.47 (Nov. 2016), pp. 24377–24389.

[88] M. Bétermier, P. Bertrand, and B. S. Lopez. “Is Non-Homologous End-Joining Really an Inherently Error-Prone Process?” In: *PLOS Genetics* 10.1 (Jan. 2014), e1004086.

[89] T. Mimori and J. A. Hardin. “Mechanism of Interaction between Ku Protein and DNA.” In: *Journal of Biological Chemistry* 261.22 (Aug. 1986), pp. 10375–10379.

[90] K. Meek et al. “The DNA-dependent Protein Kinase: The Director at the End”. In: *Immunological Reviews* 200.1 (2004), pp. 132–141.

[91] A. A. Goodarzi et al. “DNA-PK Autophosphorylation Facilitates Artemis Endonuclease Activity”. In: *The EMBO Journal* 25.16 (Aug. 2006), pp. 3880–3889.

[92] E. Riballo et al. “A Pathway of Double-Strand Break Rejoining Dependent upon ATM, Artemis, and Proteins Locating to γ-H2AX Foci”. In: *Molecular Cell* 16.5 (Dec. 2004), pp. 715–724.

[93] A. Kurosawa et al. “The Requirement of Artemis in Double-Strand Break Repair Depends on the Type of DNA Damage”. In: *DNA and Cell Biology* 27.1 (Jan. 2008), pp. 55–61.

[94] H. H. Y. Chang et al. “Non-Homologous DNA End Joining and Alternative Pathways to Double-Strand Break Repair”. In: *Nature reviews. Molecular cell biology* 18.8 (Aug. 2017), pp. 495–506.

[95] T. Ochi et al. “PAXX, a Paralog of XRCC4 and XLF, Interacts with Ku to Promote DNA Double-Strand Break Repair”. In: *Science* 347.6218 (Jan. 2015), pp. 185–188.

[96] U. Grawunder et al. “Activity of DNA Ligase IV Stimulated by Complex Formation with XRCC4 Protein in Mammalian Cells”. In: *Nature* 388.6641 (July 1997), pp. 492–495.

[97] L. Han and K. Yu. “Altered Kinetics of Nonhomologous End Joining and Class Switch Recombination in Ligase IV–Deficient B Cells”. In: *Journal of Experimental Medicine* 205.12 (Nov. 2008), pp. 2745–2753.

[98] D. Simsek and M. Jasin. “Alternative End-Joining Is Suppressed by the Canonical NHEJ Component Xrcc4/Ligase IV during Chromosomal Translocation Formation”. In: *Nature structural & molecular biology* 17.4 (Apr. 2010), pp. 410–416.

[99] J. Bentley et al. “DNA Double Strand Break Repair in Human Bladder Cancer Is Error Prone and Involves Microhomology-Associated End-Joining”. In: *Nucleic Acids Research* 32.17 (2004), pp. 5249–5259.

[100] D. D. Villarreal et al. “Microhomology Directs Diverse DNA Break Repair Pathways and Chromosomal Translocations”. In: *PLOS Genetics* 8.11 (Nov. 2012), e1003026.

[101] M. Wang et al. “PARP-1 and Ku Compete for Repair of DNA Double Strand Breaks by Distinct NHEJ Pathways”. In: *Nucleic Acids Research* 34.21 (Dec. 2006), pp. 6170–6182.

[102] L. N. Truong et al. “Microhomology-Mediated End Joining and Homologous Recombination Share the Initial End Resection Step to Repair DNA Double-Strand Breaks in Mammalian Cells”. In: *Proceedings of the National Academy of Sciences of the United States of America* 110.19 (May 2013), pp. 7720–7725.

[103] P. A. Mateos-Gomez et al. “Mammalian Polymerase ϑ Promotes Alternative NHEJ and Suppresses Recombination”. In: *Nature* 518.7538 (Feb. 2015), pp. 254–257.

[104] H. Wang et al. “The Ku-dependent Non-Homologous End-Joining but Not Other Repair Pathway Is Inhibited by High Linear Energy Transfer Ionizing Radiation”. In: *DNA Repair* 7.5 (May 2008), pp. 725–733.

[105] H. Wang et al. “Characteristics of DNA-binding Proteins Determine the Biological Sensitivity to High-Linear Energy Transfer Radiation”. In: *Nucleic Acids Research* 38.10 (June 2010), pp. 3245–3251.

[106] A. Schipler et al. “Chromosome Thripsis by DNA Double Strand Break Clusters Causes Enhanced Cell Lethality, Chromosomal Translocations and 53BP1-recruitment”. In: *Nucleic Acids Research* 44.16 (Sept. 2016), pp. 7673–7690.

[107] A. J. Pierce et al. “Ku DNA End-Binding Protein Modulates Homologous Repair of Double-Strand Breaks in Mammalian Cells”. In: *Genes & Development* 15.24 (Dec. 2001), pp. 3237–3242.

[108] Z. E. Karanjawala et al. “The Nonhomologous DNA End Joining Pathway Is Important for Chromosome Stability in Primary Fibroblasts”. In: *Current Biology* 9.24 (Dec. 1999), pp. 1501–1506.

[109] M. R. Lieber et al. “Mechanism and Regulation of Human Non-Homologous DNA End-Joining”. In: *Nature Reviews Molecular Cell Biology* 4.9 (Sept. 2003), pp. 712–720.

[110] A. A. Goodarzi and P. A. Jeggo. “The Repair and Signaling Responses to DNA Double-Strand Breaks”. In: *Advances in Genetics*. Vol. 82. Elsevier, 2013, pp. 1–45.

[111] F. Liang et al. “Homology-Directed Repair Is a Major Double-Strand Break Repair Pathway in Mammalian Cells”. In: *Proceedings of the National Academy of Sciences of the United States of America* 95.9 (Apr. 1998), pp. 5172–5177.

[112] M. Takata et al. “Homologous Recombination and Non-Homologous End-Joining Pathways of DNA Double-Strand Break Repair Have Overlapping Roles in the Maintenance of Chromosomal Integrity in Vertebrate Cells.” In: *The EMBO Journal* 17.18 (Sept. 1998), pp. 5497–5508.

[113] J. N. Strathern, B. K. Shafer, and C. B. McGill. “DNA Synthesis Errors Associated with Double-Strand-Break Repair.” In: *Genetics* 140.3 (July 1995), pp. 965–972.

[114] C. Arnaudeau, C. Lundin, and T. Helleday. “DNA Double-Strand Breaks Associated with Replication Forks Are Predominantly Repaired by Homologous Recombination Involving an Exchange Mechanism in Mammalian Cells1”. In: *Journal of Molecular Biology* 307.5 (Apr. 2001), pp. 1235–1245.

[115] P. Huertas. “DNA Resection in Eukaryotes: Deciding How to Fix the Break”. In: *Nature Structural & Molecular Biology* 17.1 (Jan. 2010), pp. 11–16.

[116] R. S. Williams et al. “Mre11 Dimers Coordinate DNA End Bridging and Nuclease Processing in Double-Strand-Break Repair”. In: *Cell* 135.1 (Oct. 2008), pp. 97–109.

[117] C. Iftode, Y. Daniely, and J. A. Borowiec. “Replication Protein A (RPA): The Eukaryotic SSB”. In: *Critical Reviews in Biochemistry and Molecular Biology* 34.3 (Jan. 1999), pp. 141–180.

[118] E. Golub et al. “Interaction of Human Rad51 Recombination Protein with Single-Stranded DNA Binding Protein, RPA”. In: *Nucleic acids research* 26 (Jan. 1999), pp. 5388–93.

[119] F. E. Benson, A. Stasiak, and S. C. West. “Purification and Characterization of the Human Rad51 Protein, an Analogue of E. Coli RecA”. In: *The EMBO Journal* 13.23 (Dec. 1994), p. 5764.

[120] W. D. Wright, S. S. Shah, and W.-D. Heyer. “Homologous Recombination and the Repair of DNA Double-Strand Breaks”. In: *Journal of Biological Chemistry* 293.27 (July 2018), pp. 10524–10535.

[121] R. Scully et al. “Association of BRCA1 with Rad51 in Mitotic and Meiotic Cells”. In: *Cell* 88.2 (Jan. 1997), pp. 265–275.

[122] E. Sonoda et al. “Rad51-Deficient Vertebrate Cells Accumulate Chromosomal Breaks Prior to Cell Death.” In: *The EMBO Journal* 17.2 (Jan. 1998), pp. 598–608.

[123] M. E. Moynahan, A. J. Pierce, and M. Jasin. “BRCA2 Is Required for Homology-Directed Repair of Chromosomal Breaks”. In: *Molecular Cell* 7.2 (Feb. 2001), pp. 263–272.

[124] S. F. Bunting et al. “53BP1 Inhibits Homologous Recombination in Brca1-deficient Cells by Blocking Resection of DNA Breaks”. In: *Cell* 141.2 (Apr. 2010), pp. 243–254.

[125] M. McVey et al. “Eukaryotic DNA Polymerases in Homologous Recombination”. In: *Annual review of genetics* 50 (Nov. 2016), pp. 393–421.

[126] J. D.-M. Goetz et al. “Reduced Repair of DNA Double-Strand Breaks by Homologous Recombination in a DNA Ligase I-deficient Human Cell Line”. In: *DNA Repair* 4.6 (June 2005), pp. 649–654.

[127] R. Bhargava, D. O. Onyango, and J. M. Stark. “Regulation of Single Strand Annealing and Its Role in Genome Maintenance”. In: *Trends in genetics : TIG* 32.9 (Sept. 2016), pp. 566–575.

[128] W. Y. Mansour et al. “Hierarchy of Nonhomologous End-Joining, Single-Strand Annealing and Gene Conversion at Site-Directed DNA Double-Strand Breaks”. In: *Nucleic Acids Research* 36.12 (July 2008), pp. 4088–4098.

[129] V. Mladenova et al. “The High Toxicity of DSB-clusters Modelling High-LET-DNA Damage Derives from Inhibition of c-NHEJ and Promotion of Alt-EJ and SSA despite Increases in HR”. In: *Frontiers in Cell and Developmental Biology* 10 (Oct. 2022).

[130] S. J. Roobol et al. “Comparison of High- and Low-LET Radiation-Induced DNA Double-Strand Break Processing in Living Cells”. In: *International Journal of Molecular Sciences* 21.18 (Sept. 2020), p. 6602.

[131] N. B. Averbeck et al. “DNA End Resection Is Needed for the Repair of Complex Lesions in G1-phase Human Cells”. In: *Cell Cycle* 13.16 (Aug. 2014), pp. 2509–2516.

[132] J. A. Nickoloff et al. “Roles of Homologous Recombination in Response to Ionizing Radiation-Induced DNA Damage”. In: *International Journal of Radiation Biology* 99.6 (June 2023), pp. 903–914.

[133] A. Sancar et al. “Molecular Mechanisms of Mammalian DNA Repair and the DNA Damage Checkpoints”. In: *Annual Review of Biochemistry* 73.1 (June 2004), pp. 39–85.

[134] K. L. Cann and G. G. Hicks. “Absence of an Immediate G1/S Checkpoint in Primary MEFs Following γ-Irradiation Identifies a Novel Checkpoint Switch”. In: *Cell Cycle* 5.16 (Aug. 2006), pp. 1823–1830.

[135] S. P. Linke et al. “P53-Mediated Accumulation of Hypophosphorylated pRb after the G1 Restriction Point Fails to Halt Cell Cycle Progression”. In: *Oncogene* 15.3 (July 1997), pp. 337–345.

[136] B.-B. S. Zhou and S. J. Elledge. “The DNA Damage Response: Putting Checkpoints in Perspective”. In: *Nature* 408.6811 (Nov. 2000), pp. 433–439.

[137] D. Deckbar et al. “Chromosome Breakage after G2 Checkpoint Release”. In: *The Journal of Cell Biology* 176.6 (Mar. 2007), p. 749.

[138] A. Asaithamby, B. Hu, and D. J. Chen. “Unrepaired Clustered DNA Lesions Induce Chromosome Breakage in Human Cells”. In: *Proceedings of the National Academy of Sciences* 108.20 (May 2011), pp. 8293–8298.

[139] F. Aymard et al. “Transcriptionally Active Chromatin Recruits Homologous Recombination at DNA Double-Strand Breaks”. In: *Nature Structural & Molecular Biology* 21.4 (Apr. 2014), pp. 366–374.

[140] A. Piovesan et al. “On the Length, Weight and GC Content of the Human Genome”. In: *BMC Research Notes* 12 (Feb. 2019), p. 106.

[141] C. Redon et al. “Histone H2A Variants H2AX and H2AZ”. In: *Current Opinion in Genetics & Development* 12.2 (Apr. 2002), pp. 162–169.

[142] E. P. Rogakou et al. “DNA Double-stranded Breaks Induce Histone H2AX Phosphorylation on Serine 139”. In: *Journal of Biological Chemistry* 273.10 (Mar. 1998), pp. 5858–5868.

[143] S. Burma et al. “ATM Phosphorylates Histone H2AX in Response to DNA Double-strand Breaks*”. In: *Journal of Biological Chemistry* 276.45 (Nov. 2001), pp. 42462–42467.

[144] E. P. Rogakou et al. “Megabase Chromatin Domains Involved in DNA Double-Strand Breaks in Vivo”. In: *The Journal of Cell Biology* 146.5 (Sept. 1999), pp. 905–916.

[145] M. Löbrich et al. “γH2AX Foci Analysis for Monitoring DNA Double-Strand Break Repair: Strengths, Limitations and Optimization”. In: *Cell Cycle* 9.4 (Feb. 2010), pp. 662–669.

[146] B. Jakob, M. Scholz, and G. Taucher-Scholz. “Biological Imaging of Heavy Charged-Particle Tracks”. In: *Radiation Research* 159.5 (May 2003), pp. 676–684.

[147] B. Meyer et al. “Clustered DNA Damage Induces Pan-Nuclear H2AX Phosphorylation Mediated by ATM and DNA–PK”. In: *Nucleic Acids Research* 41.12 (July 2013), pp. 6109–6118.

[148] H. Van Attikum and S. M. Gasser. “The Histone Code at DNA Breaks: A Guide to Repair?” In: *Nature Reviews Molecular Cell Biology* 6.10 (Oct. 2005), pp. 757–765.

[149] A. J. Morrison and X. Shen. “DNA Repair in the Context of Chromatin”. In: *Cell Cycle* 4.4 (Apr. 2005), pp. 513–512.

[150] A. Janssen, S. U. Colmenares, and G. H. Karpen. “Heterochromatin: Guardian of the Genome”. In: *Annual Review of Cell and Developmental Biology* 34.1 (Oct. 2018), pp. 265–288.

[151] Y. Lorat et al. “Beyond Repair Foci: DNA Double-Strand Break Repair in Euchromatic and Heterochromatic Compartments Analyzed by Transmission Electron Microscopy”. In: *PLOS ONE* 7.5 (May 2012), e38165.

[152] S. Timm et al. “Clustered DNA Damage Concentrated in Particle Trajectories Causes Persistent Large-Scale Rearrangements in Chromatin Architecture”. In: *Radiotherapy and Oncology* 129.3 (Dec. 2018), pp. 600–610.

[153] T. Chui-hsu Yang et al. “Neoplastic Cell Transformation by High-LET Radiation: Molecular Mechanisms”. In: *Advances in Space Research* 9.10 (Jan. 1989), pp. 131–140.

[154] M. Krämer, W. K. Weyrather, and M. Scholz. “The Increased Biological Effectiveness of Heavy Charged Particles: From Radiobiology to Treatment Planning”. In: *Technology in Cancer Research & Treatment* 2.5 (Oct. 2003), pp. 427–436.

[155] G. W. Barendsen et al. “Effects of Different Ionizing Radiations on Human Cells in Tissue Culture: III. Experiments with Cyclotron-Accelerated Alpha-Particles and Deuterons”. In: *Radiation Research* 18.1 (1963), pp. 106–119.

[156] T. Friedrich et al. “Systematic Analysis of RBE and Related Quantities Using a Database of Cell Survival Experiments with Ion Beam Irradiation”. In: *Journal of Radiation Research* 54.3 (May 2013), pp. 494–514.

[157] M. Krämer and M. Scholz. “Treatment Planning for Heavy-Ion Radiotherapy: Calculation and Optimization of Biologically Effective Dose”. In: *Physics in Medicine & Biology* 45.11 (Nov. 2000), p. 3319.

[158] R. J. Fry et al. “Studies on the Multistage Nature of Radiation Carcinogenesis”. In: *Carcinogenesis; a Comprehensive Survey* 7 (1982), pp. 155–165.

[159] C. V. Camacho et al. “Loss of P15/Ink4b Accompanies Tumorigenesis Triggered by Complex DNA Double-Strand Breaks”. In: *Carcinogenesis* 31.10 (Oct. 2010), pp. 1889–1896.

[160] A. Asaithamby et al. “Repair of HZE-Particle-Induced DNA Double-Strand Breaks in Normal Human Fibroblasts”. In: *Radiation Research* 169.4 (Apr. 2008), pp. 437–446.

[161] R. Okayasu et al. “Repair of DNA Damage Induced by Accelerated Heavy Ions in Mammalian Cells Proficient and Deficient in the Non-homologous End-Joining Pathway”. In: *Radiation Research* 165.1 (Jan. 2006), pp. 59–67.

[162] M. Cornforth, B. Loucas, and I. Shuryak. “Dose-Dependent Transmissibility of Chromosome Aberrations in Human Lymphocytes at First Mitosis. II. Biological Effectiveness of Heavy Charged Particles Versus Gamma Rays”. In: *Radiation Research* 199.3 (Jan. 2023).

[163] M. N. Cornforth. “Perspectives on the Formation of Radiation-Induced Exchange Aberrations”. In: *DNA Repair* 5.9-10 (Sept. 2006), pp. 1182–1191.

[164] M. R. Lieber. “NHEJ and Its Backup Pathways in Chromosomal Translocations”. In: *Nature Structural & Molecular Biology* 17.4 (Apr. 2010), pp. 393–395.

[165] V. Roukos et al. “Spatial Dynamics of Chromosome Translocations in Living Cells”. In: *Science (New York, N.Y.)* 341.6146 (Aug. 2013), pp. 660–664.

[166] A. Niimi et al. “Identification of DNA Double Strand Breaks at Chromosome Boundaries along the Track of Particle Irradiation”. In: *Genes, Chromosomes and Cancer* 55.8 (Aug. 2016), pp. 650–660.

[167] B. Jakob et al. “Live Cell Microscopy Analysis of Radiation-Induced DNA Double-Strand Break Motion”. In: *Proceedings of the National Academy of Sciences* 106.9 (Mar. 2009), pp. 3172–3177.

[168] J. R. K. Savage and P. J. Simpson. “Fish “Painting” Patterns Resulting from Complex Exchanges”. In: *Mutation Research/Environmental Mutagenesis and Related Subjects* 312.1 (Feb. 1994), pp. 51–60.

[169] C. Griffin et al. “Frequencies of Complex Chromosome Exchange Aberrations Induced by 238Pu α-Particles and Detected by Fluorescence in Situ Hybridization Using Single Chromosome-specific Probes”. In: *International Journal of Radiation Biology* 67.4 (Jan. 1995), pp. 431–439.

[170] R. M. Anderson, D. L. Stevens, and D. T. Goodhead. “M-FISH Analysis Shows That Complex Chromosome Aberrations Induced by α-Particle Tracks Are Cumulative Products of Localized Rearrangements”. In: *Proceedings of the National Academy of Sciences* 99.19 (Sept. 2002), pp. 12167–12172.

[171] E. Staaf et al. “Complex Aberrations in Lymphocytes Exposed to Mixed Beams of 241Am Alpha Particles and X-rays”. In: *Mutation Research/Genetic Toxicology and Environmental Mutagenesis*. From DNA Damage to Chromosomal Aberrations 756.1 (Aug. 2013), pp. 95–100.

[172] F. A. Cucinotta et al. “How Safe Is Safe Enough? Radiation Risk for a Human Mission to Mars”. In: *PLoS ONE* 8.10 (Oct. 2013). Ed. by A. A.-J. Golden, e74988.

[173] Z. Mao et al. “Comparison of Nonhomologous End Joining and Homologous Recombination in Human Cells”. In: *DNA repair* 7.10 (Aug. 2008), p. 1765.

[174] L. Schwan et al. “Base-Excision Repair Increases DNA Double-Strand Break Clustering within Heavy-Ion Tracks and Modulates Repair at δ-Electron-Induced Breaks”. In: *Scientific Reports* 16.1 (Jan. 2026), p. 1339.

[175] C. Lukas et al. “Distinct Spatiotemporal Dynamics of Mammalian Checkpoint Regulators Induced by DNA Damage”. In: *Nature Cell Biology* 5.3 (Mar. 2003), pp. 255–260.

[176] J. Schindelin et al. “Fiji: An Open-Source Platform for Biological-Image Analysis”. In: *Nature Methods* 9.7 (July 2012), pp. 676–682.

[177] N. Otsu. “A Threshold Selection Method from Gray-Level Histograms”. In: *IEEE Transactions on Systems, Man, and Cybernetics* 9.1 (Jan. 1979), pp. 62–66.

[178] J. Parsons. “The Role of Glutathione in DNA Damage by Potassium Bromate in Vitro”. In: *Mutagenesis* 15.4 (July 2000), pp. 311–316.

[179] S. Kawanishi and M. Murata. “Mechanism of DNA Damage Induced by Bromate Differs from General Types of Oxidative Stress”. In: *Toxicology* 221.2-3 (Apr. 2006), pp. 172–178.

[180] D. Ballmaier and B. Epe. “Oxidative DNA Damage Induced by Potassium Bromate under Cell-Free Conditions and in Mammalian Cells”. In: *Carcinogenesis* 16.2 (1995), pp. 335–342.

[181] V. Sharma et al. “Oxidative Stress at Low Levels Can Induce Clustered DNA Lesions Leading to NHEJ Mediated Mutations”. In: *Oncotarget* 7.18 (Mar. 2016), pp. 25377–25390.

[182] L. B. Schultz et al. “P53 Binding Protein 1 (53bp1) Is an Early Participant in the Cellular Response to DNA Double-Strand Breaks”. In: *The Journal of Cell Biology* 151.7 (Dec. 2000), pp. 1381–1390.

[183] L. Anderson, C. Henderson, and Y. Adachi. “Phosphorylation and Rapid Relocalization of 53BP1 to Nuclear Foci upon DNA Damage”. In: *Molecular and Cellular Biology* 21.5 (Mar. 2001), pp. 1719–1729.

[184] T. Visnes et al. “Small-Molecule Inhibitor of OGG1 Suppresses Proinflammatory Gene Expression and Inflammation”. In: *Science (New York, N.Y.)* 362.6416 (Nov. 2018), pp. 834–839.

[185] D. E. Barnes and T. Lindahl. “Repair and Genetic Consequences of Endogenous DNA Base Damage in Mammalian Cells”. In: *Annual Review of Genetics* 38.1 (Dec. 2004), pp. 445–476.

[186] M. Talpaert-Borlé and M. Liuzzi. “Reaction of Apurinic/Apyrimidinic Sites with [14C]Methoxyamine”. In: *Biochimica et Biophysica Acta (BBA) - Gene Structure and Expression* 740.4 (Sept. 1983), pp. 410–416.

[187] P. Fortini, M. Bignami, and E. Dogliotti. “Evidence for AP Site Formation Related to DNA-oxygen Alkylation in CHO Cells Treated with Ethylating Agents”. In: *Mutation Research/DNA Repair* 236.1 (July 1990), pp. 129–137.

[188] M. Liuzzi and M. Talpaert-Borlé. “A New Approach to the Study of the Base-Excision Repair Pathway Using Methoxyamine.” In: *Journal of Biological Chemistry* 260.9 (May 1985), pp. 5252–5258.

[189] K. Rothkamm and M. Löbrich. “Evidence for a Lack of DNA Double-Strand Break Repair in Human Cells Exposed to Very Low x-Ray Doses”. In: *Proceedings of the National Academy of Sciences* 100.9 (Apr. 2003), pp. 5057–5062.

[190] M. I. Núñez et al. “Radiation-Induced DNA Double-Strand Break Rejoining in Human Tumour Cells”. In: *British Journal of Cancer* 71.2 (Feb. 1995), pp. 311–316.

[191] M. Löbrich, B. Rydberg, and P. K. Cooper. “Repair of X-Ray-Induced DNA Double-Strand Breaks in Specific Not I Restriction Fragments in Human Fibroblasts: Joining of Correct and Incorrect Ends.” In: *Proceedings of the National Academy of Sciences of the United States of America* 92.26 (Dec. 1995), pp. 12050–12054.

[192] J. Ward. “Biochemistry of DNA Lesions”. In: *Radiation Research* 104.2 II (1985), S103–S111.

[193] L. Bee et al. “The Efficiency of Homologous Recombination and Non-Homologous End Joining Systems in Repairing Double-Strand Breaks during Cell Cycle Progression”. In: *PloS one* 8 (July 2013), e69061.

[194] B. Rydberg. “Clusters of DNA Damage Induced by Ionizing Radiation: Formation of Short DNA Fragments. II. Experimental Detection”. In: *Radiation Research* 145.2 (1996), pp. 200–209.

[195] W. R. Holley and A. Chatterjee. “Clusters of DNA Damage Induced by Ionizing Radiation: Formation of Short DNA Fragments. I. Theoretical Modeling”. In: *Radiation Research* 145.2 (Feb. 1996), pp. 188–199.

[196] B. M. Sutherland et al. “Clustered DNA Damages Induced in Isolated DNA and in Human Cells by Low Doses of Ionizing Radiation”. In: *Proceedings of the National Academy of Sciences* 97.1 (Jan. 2000), pp. 103–108.

[197] H. Yajima et al. “The Complexity of DNA Double Strand Breaks Is a Critical Factor Enhancing End-Resection”. In: *DNA Repair* 12.11 (Nov. 2013), pp. 936–946.

[198] N. I. Nakajima et al. “Visualisation of γH2AX Foci Caused by Heavy Ion Particle Traversal; Distinction between Core Track versus Non-Track Damage”. In: *PLoS ONE* 8.8 (Aug. 2013). Ed. by E. Y. Chuang, e70107.

[199] P. Sung and D. L. Robberson. “DNA Strand Exchange Mediated by a RAD51-ssDNA Nucleoprotein Filament with Polarity Opposite to That of RecA”. In: *Cell* 82.3 (Aug. 1995), pp. 453–461.

[200] J. A. Aten et al. “Dynamics of DNA Double-Strand Breaks Revealed by Clustering of Damaged Chromosome Domains”. In: *Science* 303.5654 (Jan. 2004), pp. 92–95.

[201] Y. Hagiwara et al. “3D-structured Illumination Microscopy Reveals Clustered DNA Double-Strand Break Formation in Widespread γH2AX Foci after High LET Heavy-Ion Particle Radiation”. In: *Oncotarget* 8.65 (Nov. 2017), pp. 109370–109381.

[202] J. L. Schwartz et al. “Faster Repair of DNA Double-Strand Breaks in Radioresistant Human Tumor Cells”. In: *International Journal of Radiation Oncology*Biology*Physics* 15.4 (Oct. 1988), pp. 907–912.

[203] B. M. F. Hanna, T. Helleday, and O. Mortusewicz. “OGG1 Inhibitor TH5487 Alters OGG1 Chromatin Dynamics and Prevents Incisions”. In: *Biomolecules* 10.11 (Nov. 2020), p. 1483.

[204] S. Kilic et al. “Phase Separation of 53 BP 1 Determines Liquid-like Behavior of DNA Repair Compartments”. In: *The EMBO Journal* 38.16 (Aug. 2019), e101379.

[205] L. Zhang et al. “53BP1 Regulates Heterochromatin through Liquid Phase Separation”. In: *Nature Communications* 13.1 (Jan. 2022), p. 360.

[206] S. Boeynaems et al. “Protein Phase Separation: A New Phase in Cell Biology”. In: *Trends in Cell Biology* 28.6 (June 2018), pp. 420–435.

[207] A. Zielinska et al. “Direct Visualization of Repair of Oxidative Damage by OGG1 in the Nuclei of Live Cells”. In: *Journal of Biochemical and Molecular Toxicology* 25.1 (2011), pp. 1–7.

[208] N. C. de Souza-Pinto et al. “The Recombination Protein RAD52 Cooperates with the Excision Repair Protein OGG1 for the Repair of Oxidative Lesions in Mammalian Cells”. In: *Molecular and Cellular Biology* 29.16 (Aug. 2009), pp. 4441–4454.

[209] M. L. Hegde et al. “Scaffold Attachment Factor A (SAF-A) and Ku Temporally Regulate Repair of Radiation-Induced Clustered Genome Lesions”. In: *Oncotarget* 7.34 (June 2016), pp. 54430–54444.

[210] D. Pang et al. “Radiation-Generated Short DNA Fragments May Perturb Non-homologous End-joining and Induce Genomic Instability”. In: *Journal of Radiation Research* 52.3 (May 2011), pp. 309–319.

[211] A. Shibata, P. Jeggo, and M. Löbrich. “The Pendulum of the Ku-Ku Clock”. In: *DNA Repair* 71 (Nov. 2018), pp. 164–171.

[212] A. Asaithamby and D. J. Chen. “Mechanism of Cluster DNA Damage Repair in Response to High-Atomic Number and Energy Particles Radiation”. In: *Mutation Research/Fundamental and Molecular Mechanisms of Mutagenesis* 711.1-2 (June 2011), pp. 87–99.

[213] A. E. O. Fisher et al. “Poly(ADP-Ribose) Polymerase 1 Accelerates Single-Strand Break Repair in Concert with Poly(ADP-Ribose) Glycohydrolase”. In: *Molecular and Cellular Biology* 27.15 (Aug. 2007), pp. 5597–5605.

[214] A. Hanssen-Bauer et al. “XRCC1 Coordinates Disparate Responses and Multiprotein Repair Complexes Depending on the Nature and Context of the DNA Damage”. In: *Environmental and Molecular Mutagenesis* 52.8 (Oct. 2011), pp. 623–635.

[215] N. N. Hooten et al. “Poly(ADP-ribose) Polymerase 1 (PARP-1) Binds to 8-Oxoguanine-DNA Glycosylase (OGG1) *”. In: *Journal of Biological Chemistry* 286.52 (Dec. 2011), pp. 44679–44690.

[216] R. Wang et al. “OGG1-initiated Base Excision Repair Exacerbates Oxidative Stress-Induced Parthanatos”. In: *Cell Death & Disease* 9 (June 2018).

[217] N. Desai et al. “Immunofluorescence Detection of Clustered γ-H2AX Foci Induced by HZE-Particle Radiation”. In: *Radiation Research* 164.4 (Oct. 2005), pp. 518–522.

[218] S. Britton, J. Coates, and S. P. Jackson. “A New Method for High-Resolution Imaging of Ku Foci to Decipher Mechanisms of DNA Double-Strand Break Repair”. In: *The Journal of Cell Biology* 202.3 (Aug. 2013), pp. 579–595.

[219] D. Varga et al. *Quantification of DNA Damage Induced γH2AX Focus Formation via Super-Resolution dSTORM Localization Microscopy*. May 2019.

[220] P. Akuwudike et al. “Mechanistic Insights from High Resolution DNA Damage Analysis to Understand Mixed Radiation Exposure”. In: *DNA Repair* 130 (Oct. 2023), p. 103554.

[221] S. Truckenbrodt et al. “X10 Expansion Microscopy Enables 25-nm Resolution on Conventional Microscopes”. In: *EMBO reports* 19.9 (Sept. 2018), e45836.

[222] E. L. Faulkner et al. “Imaging Nanoscale Nuclear Structures with Expansion Microscopy”. In: *Journal of Cell Science* 135.14 (July 2022), jcs259009.

[223] D. Depes et al. “Single-Molecule Localization Microscopy as a Promising Tool for γH2AX/53BP1 Foci Exploration”. In: *The European Physical Journal D* 72.9 (Sept. 2018), p. 158.

[224] M. Eryilmaz et al. “Localization Microscopy Analyses of MRE11 Clusters in 3D-Conserved Cell Nuclei of Different Cell Lines”. In: *Cancers* 10.1 (Jan. 2018), p. 25.

[225] M. Hausmann et al. “Super-Resolution Localization Microscopy of Radiation-Induced Histone H2AX-phosphorylation in Relation to H3K9-trimethylation in HeLa Cells”. In: *Nanoscale* 10.9 (Mar. 2018), pp. 4320–4331.

[226] H. Scherthan et al. “Nanostructure of Clustered DNA Damage in Leukocytes after In-Solution Irradiation with the Alpha Emitter Ra-223”. In: *Cancers* 11.12 (Nov. 2019), p. 1877.

[227] F. Natale et al. “Identification of the Elementary Structural Units of the DNA Damage Response”. In: *Nature Communications* 8 (June 2017), p. 15760.

[228] S. P. Moore et al. “The Human Homologous Pairing Protein HPP-1 Is Specifically Stimulated by the Cognate Single-Stranded Binding Protein hRP-A.” In: *Proceedings of the National Academy of Sciences* 88.20 (Oct. 1991), pp. 9067–9071.

[229] B. Rydberg et al. “Dose-Dependent Misrejoining of Radiation-Induced DNA Double-Strand Breaks in Human Fibroblasts: Experimental and Theoretical Study for High- and Low-LET Radiation”. In: *Radiation Research* 163.5 (May 2005), pp. 526–534.

[230] K. George et al. “Chromosome Aberrations in the Blood Lymphocytes of Astronauts after Space Flight”. In: *Radiation Research* 156.6 (Dec. 2001), pp. 731–738.

[231] T. Elsässer et al. “Quantification of the Relative Biological Effectiveness for Ion Beam Radiotherapy: Direct Experimental Comparison of Proton and Carbon Ion Beams and a Novel Approach for Treatment Planning”. In: *International Journal of Radiation Oncology*Biology*Physics* 78.4 (Nov. 2010), pp. 1177–1183.

[232] S. Incerti et al. “Geant4-DNA Example Applications for Track Structure Simulations in Liquid Water: A Report from the Geant4-DNA Project”. In: *Medical Physics* 45.8 (Aug. 2018).

[233] T. Pfuhl, T. Friedrich, and M. Scholz. “Comprehensive Comparison of Local Effect Model IV Predictions with the Particle Irradiation Data Ensemble”. In: *Medical Physics* 49.1 (Jan. 2022), pp. 714–726.

[234] G. Baiocco et al. “A Matter of Space: How the Spatial Heterogeneity in Energy Deposition Determines the Biological Outcome of Radiation Exposure”. In: *Radiation and Environmental Biophysics* 61.4 (Nov. 2022), pp. 545–559.

[235] F. Zafar et al. “Homologous Recombination Contributes to the Repair of DNA Double-Strand Breaks Induced by High-Energy Iron Ions”. In: *Radiation Research* 173.1 (Jan. 2010), p. 27.

[236] R. Biehs et al. “DNA Double-Strand Break Resection Occurs during Non-homologous End Joining in G1 but Is Distinct from Resection during Homologous Recombination”. In: *Molecular Cell* 65.4 (Feb. 2017), 671–684.e5.

[237] E. Sonoda et al. “Differential Usage of Non-Homologous End-Joining and Homologous Recombination in Double Strand Break Repair”. In: *DNA Repair*. Mechanisms of Chromosomal Translocation 5.9 (Sept. 2006), pp. 1021–1029.

[238] M. V. Brock, J. G. Herman, and S. B. Baylin. “Cancer as a Manifestation of Aberrant Chromatin Structure”. In: *Cancer journal (Sudbury, Mass.)* 13.1 (2007), pp. 3–8.

[239] A. Sollazzo et al. “Alpha Particles and X Rays Interact in Inducing DNA Damage in U2OS Cells”. In: *Radiation Research* 188.4 (Aug. 2017), p. 400.

[240] A. Sollazzo et al. “Live Dynamics of 53BP1 Foci Following Simultaneous Induction of Clustered and Dispersed DNA Damage in U2OS Cells”. In: *International Journal of Molecular Sciences* 19.2 (Feb. 2018), p. 519.

[241] S. V. Costes et al. “Imaging Features That Discriminate between Foci Induced by High- and Low-LET Radiation in Human Fibroblasts”. In: *Radiation Research* 165.5 (May 2006), pp. 505–515.

[242] F. Antonelli et al. “Induction and Repair of DNA DSB as Revealed by H2AX Phosphorylation Foci in Human Fibroblasts Exposed to Low- and High-LET Radiation: Relationship with Early and Delayed Reproductive Cell Death”. In: *Radiation Research* 183.4 (Apr. 2015), pp. 417–431.

[243] D. R. Whelan and E. Rothenberg. “Super-Resolution Mapping of Cellular Double-Strand Break Resection Complexes during Homologous Recombination”. In: *Proceedings of the National Academy of Sciences* 118.11 (Mar. 2021), e2021963118.

[244] S. Bekker-Jensen et al. “Spatial Organization of the Mammalian Genome Surveillance Machinery in Response to DNA Strand Breaks”. In: *Journal of Cell Biology* 173.2 (Apr. 2006), pp. 195–206.

[245] B. Jakob, J. Splinter, and G. Taucher-Scholz. “Positional Stability of Damaged Chromatin Domains along Radiation Tracks in Mammalian Cells”. In: *Radiation Research* 171.4 (Apr. 2009), pp. 405–418.

[246] J. Reindl et al. “Chromatin Organization Revealed by Nanostructure of Irradiation Induced γH2AX, 53BP1 and Rad51 Foci”. In: *Scientific Reports* 7.1 (Feb. 2017), p. 40616.

[247] B. Jakob and G. Taucher-Scholz. “Interaction of Heavy Ions with Nuclear Chromatin: Spatiotemporal Investigations of Biological Responses in a Cellular Environment”. In: *Nuclear Instruments and Methods in Physics Research Section B: Beam Interactions with Materials and Atoms* 245.1 (Apr. 2006), pp. 292–297.

[248] J. Tang et al. “Acetylation Limits 53BP1 Association with Damaged Chromatin to Promote Homologous Recombination”. In: *Nature Structural & Molecular Biology* 20.3 (Mar. 2013), pp. 317–325.

[249] S. Tonnemacher, M. Eltsov, and B. Jakob. “Correlative Light and Electron Microscopy (CLEM) Analysis of Nuclear Reorganization Induced by Clustered DNA Damage Upon Charged Particle Irradiation”. In: *International Journal of Molecular Sciences* 21.6 (Jan. 2020), p. 1911.

[250] U. Kasten-Pisula et al. “In Normal Human Fibroblasts Variation in DSB Repair Capacity Cannot Be Ascribed to Radiation-Induced Changes in the Localisation, Expression or Activity of Major NHEJ Proteins”. In: *Radiotherapy and Oncology* 86.3 (Mar. 2008), pp. 321–328.

[251] Y. Matsumoto et al. “Gene Expression Analysis in Human Malignant Melanoma Cell Lines Exposed to Carbon Beams”. In: *International Journal of Radiation Biology* 84.4 (Jan. 2008), pp. 299–314.

[252] A. Suetens et al. “Carbon Ion Irradiation of the Human Prostate Cancer Cell Line PC3: A Whole Genome Microarray Study”. In: *International Journal of Oncology* 44.4 (Apr. 2014), pp. 1056–1072.

[253] L.-H. Ding et al. “Distinct Transcriptome Profiles Identified in Normal Human Bronchial Epithelial Cells after Exposure to γ-Rays and Different Elemental Particles of High Z and Energy”. In: *BMC Genomics* 14.1 (June 2013), p. 372.

[254] Y. Ziv et al. “Chromatin Relaxation in Response to DNA Double-Strand Breaks Is Modulated by a Novel ATM- and KAP-1 Dependent Pathway”. In: *Nature Cell Biology* 8.8 (Aug. 2006), pp. 870–876.

[255] A. A. Goodarzi et al. “ATM Signaling Facilitates Repair of DNA Double-Strand Breaks Associated with Heterochromatin”. In: *Molecular Cell* 31.2 (July 2008), pp. 167–177.

[256] Y. Fan et al. “Histone H1 Depletion in Mammals Alters Global Chromatin Structure but Causes Specific Changes in Gene Regulation”. In: *Cell* 123.7 (Dec. 2005), pp. 1199–1212.

[257] M. Murga et al. “Global Chromatin Compaction Limits the Strength of the DNA Damage Response”. In: *The Journal of Cell Biology* 178.7 (Sept. 2007), pp. 1101–1108.

[258] A. L. Brooks et al. “Relative Effectiveness of HZE Iron-56 Particles for the Induction of Cytogenetic Damage In Vivo”. In: *Radiation Research* 155.2 (2001), pp. 353–359.

[259] M. Durante and F. A. Cucinotta. “Heavy Ion Carcinogenesis and Human Space Exploration”. In: *Nature Reviews Cancer* 8.6 (June 2008), pp. 465–472.

Curriculum Vitae

Laura Schwan
Nationality: German

Education

2021 – 2025	**PhD in biology, GSI Helmholtzzentrum für Schwerionenforschung Darmstadt** Department: Molecular Radiobiology and Imaging – Biophysics department, GSI Helmholtzzentrum für Schwerionenforschung Darmstadt University: Technical University of Darmstadt – Department of Biology
2018 – 2020	**Master of Science in biophysics, Goethe University Frankfurt/Main**
2015 – 2018	**Bachelor of Science in biophysics, Goethe University Frankfurt/Main**

Scholarships and Certificates

August 2023	**Travel award scholarship** ICRR, Montreal (Canada)
November 2022	**1st Posterprize** Biology Symposium of Technical University of Darmstadt, Darmstadt (Germany)
September 2022	**Certificate** ESA-FAIR Space Radiation Summer School, Darmstadt (Germany)
September 2021	**Certificate** ESA-FAIR Space Radiation Summer School Videoconference

Publications

Schwan, L., Averbeck, N.B., Durante, M. et al. Base-excision repair increases DNA double-strand break clustering within heavy-ion tracks and modulates repair at δ-electron-induced breaks. Sci Rep 16, 1339 (2026).
`https://doi.org/10.1038/s41598-025-32823-z`

Acknowledgments

An dieser Stelle möchte ich allen danken, die mich während meiner Promotion sowie beim Anfertigen der Dissertation unterstützt und begleitet haben.

First of all I would like to thank Prof. Dr. Marco Durante for giving me the opportunity to do my PhD in the biophysics department at GSI and for being part in my examination committee. I'm very thankful for all of his support and scientific input during this time.

Vor allem möchte ich Herrn Prof. Dr. Burkhard Jakob für seine Betreuung, sowie für seine Expertise und wertvollen Ratschläge danken. Vielen Dank für die zahlreichen Diskussionen und die Möglichkeit, jederzeit das Gespräch suchen zu können.

Des weiteren möchte ich mich herzlich bei Herrn Prof. Dr. Alexander Löwer bedanken für die Übernahme des Zweitgutachtens und die wertvollen Ratschläge während der Komitee-Meetings.

Ein besonderer Dank gilt auch meiner Mentorin Dr. Nicole Averbeck für ihre exzellente Unterstützung und umfassende Betreuung. Herzlichen Dank, dass ich jederzeit meine Anliegen besprechen konnte und ich immer eine offene Tür vorfand.

Bei Prof. Dr. Patrick Heun bedanke ich mich für die Zustimmung zur Teilnahme an der Prüfungskommission meiner Disputation und die sehr freundliche Korrespondenz.

Nicht zuletzt möchte ich meinen Arbeitskollegen danken, die mich während dieser Zeit begleitet und unterstützt haben: Henrieke, Lisa, Katja, Raffael, Amaya und Dmitri sowie der gesamten DNA-Gruppe möchte ich für die angenehme Arbeitsatmosphäre, große Hilfsbereitschaft und ihr technisches Wissen im Labor danken.
Auch möchte ich mich bei allen Strahlzeit-Beteiligten für Ihre Unterstützung und Mithilfe bedanken. Insbesondere möchte ich mich dafür bei Burkhard, Nicole, Henrieke und Lisa bedanken, die mir beim Präparieren meiner Strahlzeitproben tagsüber sowie auch in mancher Nacht mitgeholfen haben.

Der Helmholtz Graduate School for Hadron and Ion Research, HGS-HIRe for FAIR, möchte ich mich vor allem für die finanzielle Unterstützung meiner Reise zur ICRR 2023 in Montreal bedanken. Die Teilnahme an Konferenzen während meiner Doktoranden-Zeit waren sehr wertvolle Erlebnisse.

I'm especially grateful for all the wonderful friends I made during my PhD time at GSI. Francesca, Chiara, Tamara, Cristina, Martina, Gianmarco, Warisara, Nicolò, Cosimo, Esther, Gaia, Olga, Daria, Moritz and everyone else, thank you for bringing so much joy to GSI.

Zum Schluss möchte ich mich bei all meinen Freunden, vor allem Franziska, Lars, Linda, Olga, Sara und Niklas, und meiner Familie für ihre unerlässliche Unterstützung auch in schwierigen Phasen danken. Von Herzen möchte ich mich bei meinen Eltern für die finanzielle und emotionale Unterstützung während meines gesamten Studiums bedanken. Ich habe bei euch immer meinen Rückzugsort gefunden.